THESIS FOR THE DEGREE OF DOCTOR OF PHILOSOPHY

Multimodal Imaging of Anisotropic Hierarchical Materials

Adrian Rodriguez Palomo

Department of Physics

CHALMERS UNIVERSITY OF TECHNOLOGY

Gothenburg, Sweden 2022

Multimodal Imaging of Anisotropic Hierarchical Materials

ADRIAN RODRIGUEZ PALOMO
ISBN 978-91-7905-687-2

Doktorsavhandlingar vid Chalmers tekniska högskola
Ny serie nr 5153
ISSN 0346-718X

Department of Physics
Chalmers University of Technology
SE-412 96 Gothenburg
Sweden
Telephone + 46 (0)31-772 1000

Chalmers Reproservice
Gothenburg, Sweden 2022

Abstract

The thesis is focused on studying the nanostructure of natural and synthetic hierarchical materials with biological applications, using X-ray scattering imaging and birefringence microscopy. The term "hierarchical materials" is used for structures composed of sub-units organised in different length scales that create the building blocks for the next level.

Hierarchical materials are commonly found in nature, with diverse structures and functionalities. In the first part of this thesis, the nanostructure of mineralised tissue, such as tusk and bone, was the focus. Scanning SAXS, SAXS tensor tomography and birefringence microscopy were used to study the helicoidal structure of narwhal tusk. A high degree of anisotropy was found, in which the dentine and cementum have a very highly organised nanostructure with a preferential orientation along the tusk. However, those two main components differ in the deviations from that primary orientation, which revealed complex helical pattern that could be the source of its anisotropic mechanical properties. A layered structure was also observed using X-ray fluorescence spectroscopy, indicating tusk growth layers that reflect the animal history. Those methods were also applied to study the anisotropic nanostructure of regenerated bone in biodegradable scaffolds and titanium implants *in vivo*, successfully demonstrating that the scaffold or implant architecture influence the new bone formation. Scaffolds with aligned fibres led to well-structured bone and a faster regeneration process, while scaffolds with randomly oriented fibres only created a callus around the damaged area with poor growth of new tissue.

In the second part of this thesis, the anisotropy of self-assembled lyotropic liquid crystals for 3D printing of bone-mimetic composites was studied. This work aimed to understand the fundamental processes and mechanisms that induce the alignment of the self-assembled crystalline units to create composites with more anisotropic mechanical properties. In that study, an *in situ* characterisation of the nanostructure during flow in the 3D printer was done using scanning SAXS and birefringence microscopy to correlate the manufacturing process with the observed structural alignment of the material. The results demonstrated the role of the shear stress in such liquid crystals, highlighting the effect it has on the anisotropy and morphological transitions in the self-assembled structures. The importance of time and environmental conditions during 3D printing is also shown, which may affect the final structure and orientation.

Keywords: Hierarchical Materials, Multimodal Imaging, X-Ray Scattering, Birefringence, Biomaterials.

List of Papers

This thesis is based on the work contained in the following papers:

I *In situ* visualization of the structural evolution and alignment of lyotropic liquid crystals in confined flow.
A. Rodriguez-Palomo, V. Lutz-Bueno, X. Cao, R. Kádár, M. Andersson, M. Liebi.
Small 17, 2021, 2006229.

II Nanostructure and anisotropy of 3D printed lyotropic liquid crystals studied by scattering and birefringence imaging.
A. Rodriguez-Palomo, V. Lutz-Bueno, M. Guizar-Sicairos, R. Kádár, M. Andersson, M. Liebi.
Additive Manufacturing 47, 2021, 102289.

III SAXS imaging reveals optimized osseointegration properties of bioengineered oriented 3D-PLGA/aCaP scaffolds in a critical size bone defect model.
E. A. Casanova*, A. Rodriguez-Palomo*, L. Stähli, O. Gröninger, Y. Neldner, S. Tiziani, A. Perez-Dominguez, M. Guizar-Sicairos, Z. Gao, C. Appel, L. C. Nielsen, M. Georgiadis, F. E. Weber, W. Stark, H-C Pape, P. Cinelli**, M. Liebi**.
*Submitted Manuscript, **2022**.*

IV Hierarchical structure of narwhal tusk.
A. Rodriguez-Palomo*, J. Palle*, E. Garde, P. A. Vibe, T. E. K. Christensen, N. K. Wittig, M. R. V. Jørgensen, I. Kantor, M. Burghammer, J. Liu, K. Jakata, P. Cook, J. T. Avaro, C. Appel, L. C. Nielsen, M.-P. H. Jørgensen, M. Liebi**, H. Birkedal**
Manuscript

Contribution Report

I Main author of the publication. I prepared the samples and performed the experiments with the assistance and support of XC in the microfluidics production, VL in the X-ray experiments and RK in the rheology characterisation. I analysed the data with the assistance of ML regarding the scattering and RK in the rheology experiments. I wrote the manuscript. All authors have approved the final version of the manuscript.

II Main author of the publication. I designed the idea of the experiment with ML. I did the sample preparation and performed the scattering experiments with ML, assisted by VL and MGS. I performed the birefringence imaging and the rheological characterisation, assisted by RK. I analysed the data with the assistance of ML regarding the scattering and RK in the rheology experiments. I wrote the manuscript. All authors have approved the final version of the manuscript.

III Shared main author of the publication. I prepared the samples and performed the synchrotron experiments with ML, MGS, ZG and CA. I did the data analysis of the X-ray scattering experiments with the assistance of LN, ML, MG and MGS and the micro-computed tomography. I wrote the manuscript together with EAC, PC and ML. All authors have approved the final version of the manuscript.

IV Shared main author of the publication. I prepared the samples for the synchrotron experiments with JP and NKW. I performed the synchrotron experiments with ML, JTA and CA at the Swiss Light Source (PSI, Switzerland) and with ML, JP, and MB at the ESRF (France). I analysed the data with the assistance of JP, TEKC and NL. I wrote the manuscript together with ML and HB. All authors have approved the final version of the manuscript.

Table of Contents

Chapter 1

Introduction

Human history has been supported by using natural materials such as wood, bone or stone to create tools and structures that allowed a better life quality. The transition from natural to synthetic materials was driven by the necessity of improved performance over a more extended period of time, with stronger, lighter and tougher materials at a lower cost and with the possibility of mass production. However, modern societies' current economic growth and expansion rates require materials that can overcome the challenges of transportation, medicine or energy production. Synthetic materials as they have been used in the last century are becoming obsolete, highly inefficient and unsustainable. It is now time to make better use of the available resources and use materials smarter. Natural materials are catching the attention of scientists and engineers again for their unique and complex structures on a smaller length scale. Inspired by the hierarchical architecture of natural materials, part of the research in functional and structural materials is being directed towards bioinspired structures. However, mimicking the structures of natural materials is not a trivial issue. Natural materials are typically made of a very limited number of components available in the surroundings of the environment, with usually poor intrinsic properties. Years of evolution and adaptation assembled them into complex structures with features on the nano, micro and macroscale. The knowledge about the natural structures that surround us is yet very limited. Many species evolved creative solutions to daily problems by combining their basic building blocks in intricate structures. With the recent advances in the new characterisation tools, being able to reach from millimetres to subatomic resolution allow us to decipher such intricated architectures that are yet a mystery for us.[1]

Centred on the current needs of modern medicine, the field of biomaterials is rapidly expanding. The target in this field has been to replace defective or damaged tissue with synthetic bulk materials, which were designed to avoid any interaction and go unnoticed by the organism. More recent strategies for imitating natural structures aim to produce high-performing materials that can also interact with the biological environment and be part of the organism. Examples of this can be found in using scaffolds for bone regeneration. In contrast with the old ceramic fillings and metallic structural parts for bone replacement, composite scaffolds that can integrate into the defect and promote the growth of new bone are the target of scientists and medical doctors. The scaffolds do not aim to offer mechanical support or be a permanent substitute for the missing part. However, they serve as a matrix where the original tissue can quickly grow and recover its functionality. That is achieved by imitating the natural environment, artificially creating the appropriate environment for cells to populate and divide.[2] In an optimal case, the scaffold will eventually dissolve without a trace of any synthetic material, leaving the native tissue.

Often, not only structural support is wanted, but recovering the functionality of an organ is desired. Analogous to that strategy, soft tissue is also created by a (often polymeric) scaffold or template mimicking the original collagen matrix or fibrillar tissue. To form functional biomedical devices and scaffolds, non-toxic materials compatible with the aqueous environment of the body and capable of interacting with the environment without causing rejection or foreign body reactions are needed. Self-assembled structures are examples of smart use of materials forming hierarchical structures inspired by nature. Inducing anisotropy in the nanoscale makes it possible to create materials with anisotropic physical properties. These materials can be used, e.g. for heart valve replacements, where a fibrinous flexible tissue with anisotropic mechanical properties is needed.[3] Biomimetic composites inspired by the bone-cartilage interphase previously developed, imitating the structure of collagen fibres and hydroxyapatite nanoplatelets in bone.[4] It consists of aligned self-assembled lyotropic liquid crystals, crosslinked and mineralised with calcium phosphate nanoparticles. In order to control the long-range anisotropy, the composites are fabricated into hierarchical structures using extrusion-based 3D printing as a manufacturing method. The self-assembled polymeric matrix is printed and crosslinked to be mineralised in a further step. A more detailed and systematic study of the 3D printing process is necessary to achieve complete control of the induced anisotropy.

The work presented in this thesis aimed to investigate and understand the hierarchical structure of anisotropic materials from natural sources, such as narwhal tusk and bone, and artificially created via self-assembly, as in the bioinspired 3D printed lyotropic liquid crystals. For that purpose, a multiscale imaging approach was chosen, using small-angle X-ray scattering in scanning (2D) and tensor tomography (3D) modes, birefringence microscopy, and in some cases, X-ray fluorescence spectroscopy and X-ray computed tomography. Complementary characterisation techniques such as rheology were used to obtain a more thorough understanding of the materials of study. In more detail, this work aimed to

1. Provide fundamental knowledge about the micro and nanostructure of narwhal tusk as an example of mineralised tissue with a complex architecture.

2. Study the quality of newly formed bone during the ongoing regeneration process in scaffolds and implants as an example of an applied case.

3. Understand the anisotropy induced during the 3D printing of self-assembled lyotropic liquid crystals, a synthetic hierarchical material bioinspired by the hierarchical structure of bone.

Overall, this thesis tried to establish a systematic method to study the morphology and nanostructure of anisotropic hierarchical materials using imaging methods which can be applied to other systems in future research.

Chapter 2

Imaging Methods for Anisotropic Materials

Imaging refers to the multidisciplinary field of science and technology that uses different methods (electromagnetic radiation, neutrons, magnetic fields, etc.) to collect and process information in the form of images. An image is the representation of a set of values with a specific spatial distribution in a particular coordinate system. The information encoded in each pixel is meaningless without the spatial context where it is placed. On the one hand, the information represented in an image can be a scalar value as in radiography (Figure 2.1a), where the projection of the transmission of X-rays through an object is measured in each pixel, and X-ray computed tomography (Figure 2.1b), where a collection of transmission projections of an object at different rotation angles are combined to reconstruct the 3D transmission values in each volumetric element. On the other hand, an image can represent vectors with magnitude and direction, as in the representation of vectorial fields (Figure 2.1c) and tensor tomography (Figure 2.1d), introduced in Section 2.3.3.

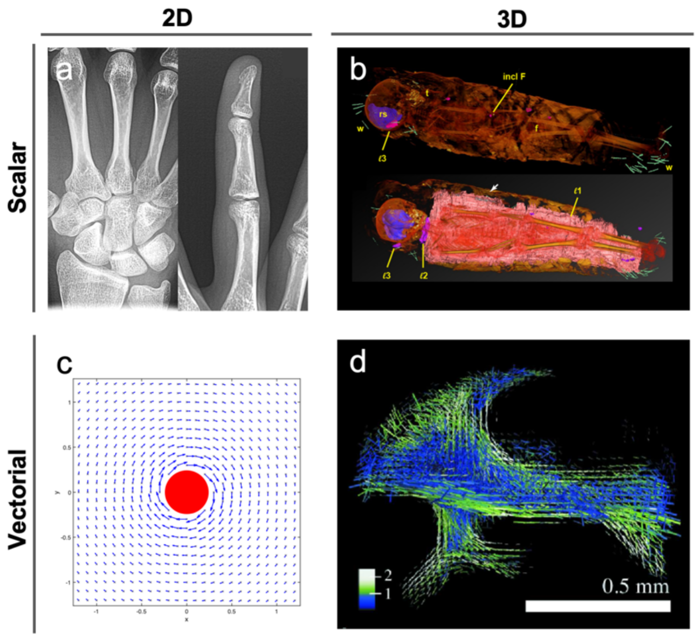

Figure 2.1. Examples of information obtained using imaging techniques. **a**) Radiography of the wrist and finger bones. **b**) X-ray computed tomography of an Egyptian mummy. **c**) Magnetic field around a straight conductor carrying an electrical current. **d**) Small-angle X-ray scattering tensor tomography of a trabecula from a human vertebra. Adapted with permission from Stock et al.[5] (Copyright 2020, The Royal Society) and Liebi et al.[6] (Copyright 2018, International Union of Crystallography).

Light microscopies are one of the best known and most spread imaging techniques. However, they have several limitations that impede the study of large samples or materials in the micro and nanoscale. The penetration power of visible light is very low compared to other types of electromagnetic radiation, allowing only the study of the surface or very thin samples. The resolution of the technique is limited by the diffraction limit, which is proportional to approximately half of the wavelength ($\approx \lambda/2$). Even though there are several improvements to reach better resolutions, the limit for optical microscopies is around hundreds of micrometres. Imaging methods with lower wavelengths able to overcome the diffraction limit of optical microscopes are electron microscopies, X-rays and γ-rays. Electrons have a small wavelength (0.1 – 10 Å), which has contributed enormously to the characterisation of nanomaterials and the study of biological structures. However, they also have a very small penetration power (~100 nm) and can only image the surface or be transmitted through very thin samples (<100 nm).[7] In contrast, X-rays also have a wavelength lower than visible light (0.1 – 10 Å) while having a high penetration power (~1 m in water at 10 keV), ideal for non-destructive characterization of materials and the study of thick samples. While these methods tend to be non-destructive, they often use high doses of ionizing radiation, which can cause radiation damage. They also have the advantage of probing the electron density, avoiding the need for labelling and staining materials with similar densities. Many biological and bioinspired materials have a hierarchical order at different length scales. The study of the ultrastructure of such materials has been a challenge for several years due to the complexity of their architecture. The advances in X-ray techniques have contributed to the investigation of those materials, making possible to investigate their structure in multiple length scales.

2.1. Full-Field and Scanning Imaging

In imaging, two leading technologies are often used to acquire information: full-field and scanning techniques. As shown in Figure 2.2a, Full-field techniques use a beam larger than the sample and a set of lenses and other optical elements to illuminate the sample, collecting the transmitted (or reflected) radiation in a detector. The main characteristic of this technology is that the detector collects the information of the entire field of view simultaneously. This technique has technical limitations from the optical elements, the diffraction limit, which defines the maximum possible resolution. One option to overcome the resolution limit is lens-less techniques such as some coherent diffraction methods.[8]

The other approach, shown in Figure 2.2b, uses scanning imaging to construct an image. In a scanning setup, the sample is raster scanned by a focused beam, ideally much smaller than the sample size. The resolution of scanning methods is defined by the step size during the scanning process, making this strategy a lens-less technique. Alternatively, there are imaging techniques that overcome the resolution limit by beam and step size by using coherent radiation, such as ptychography,[9, 10] not covered in this thesis. After a scanning experiment, the data measured consists of a collection of multiple detector images, each belonging to a very well-defined spatial position in the sample. The detector collects the information for each individual point at a specific position in space. The image is later constructed by reducing the obtained data to a scalar value or a vectorial field placed in the corresponding pixel coordinate where it was measured, which allows for creating images with different contrasts (e.g., based on diffraction, scattering, fluorescence).

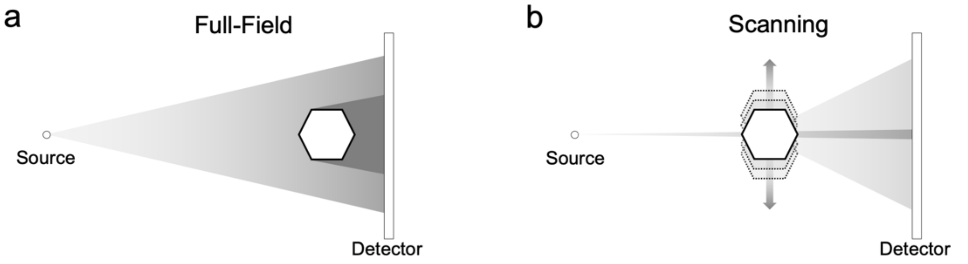

Figure 2.2. Full-field (**a**) and scanning (**b**) modes for transmission techniques. Full-field collects the shade or signal passing through the sample simultaneously, and scanning techniques use a focused beam to collect the signal from individual points. The sample is moved to be scanned by the beam.

In terms of X-ray imaging, synchrotron radiation is widely used due to its high intensity and possibility of reaching micro and nano focused beams. These large-scale facilities, introduced in the next section, are therefore ideal for full-field and scanning techniques such as the ones discussed in Sections 2.3 which can be complemented with optical light techniques, introduced in Section 2.4.

2.2. Synchrotron Radiation[11]

Synchrotrons are circular particle accelerators used to produce high-intensity electromagnetic radiation. Synchrotron radiation compiles all the electromagnetic radiation emitted by synchrotrons, which has a broad spectrum, from microwaves to hard X-rays. Synchrotrons are generally composed of a linear accelerator, a booster and storage ring, which contain focusing and accelerating elements to keep the electrons in a circular path, insertion devices and bending magnets that produce such radiation, and beamlines that use the produced radiation for different purposes.

Table 2.1. Facts of selected synchrotron facilities.

Facility	Country	Circumference (m)	Storage-ring Energy (GeV)	Current (mA)	Brilliance (ph/s/mm^2/mrad^2/0.1%BW)
SPring8	Japan	1436	8.0	100	2×10^{21}
APS	USA	1104	7.0	100	8×10^{19}
ESRF-EBS	France	844	6.0	200	3×10^{21}
Petra-III	Germany	2304	6.0	100	2×10^{21}
MAX IV	Sweden	528	3.0	500	8×10^{21}
Diamond	UK	562	3.0	300	3×10^{20}
Soleil	France	354	2.75	500	1×10^{20}
SLS	Switzerland	288	2.4	400	4×10^{19}
Elettra	Italy	260	2 – 2.4	320	1×10^{19}
BESSY II	Germany	240	1.7	100	5×10^{18}

2.2.1. Layout of a Synchrotron Facility

In a synchrotron, electrons are created in an electron gun, packed in bunches, and accelerated using a linear accelerator (LINAC) to about ~100 MeV. The accelerated electrons are injected into the booster ring, a circular accelerator where they reach the final energy (~2 – 8 GeV) before entering the storage ring. The storage ring contains the electron bunches and keeps them circulating in a closed path using magnetic fields. To avoid collisions between the electrons and the atoms of the atmospheric gas and minimize the energy loss, the storage ring is kept under ultrahigh vacuum (~10^{-9} mbar). Its shape is polygonal, as schematically represented in Figure 2.3a, composed of straight sections with insertion devices (wiggles and undulators), that create the high-brilliant synchrotron radiation, and curved sections with bending, quadrupole and sextupole magnets. The bending (dipole) magnets connect the straight sections and are responsible for deflecting the electron beam. During the bending process, the electrons produce synchrotron radiation; however, its brilliance is significantly lower than that produced by insertion devices but several orders of magnitude higher than the one produced by laboratory sources. Quadrupole magnets are used to focus the divergence of the electron beam. Quadrupoles produce an energy dispersion in the electron beam (chromatic aberration) that is corrected using sextupole magnets.

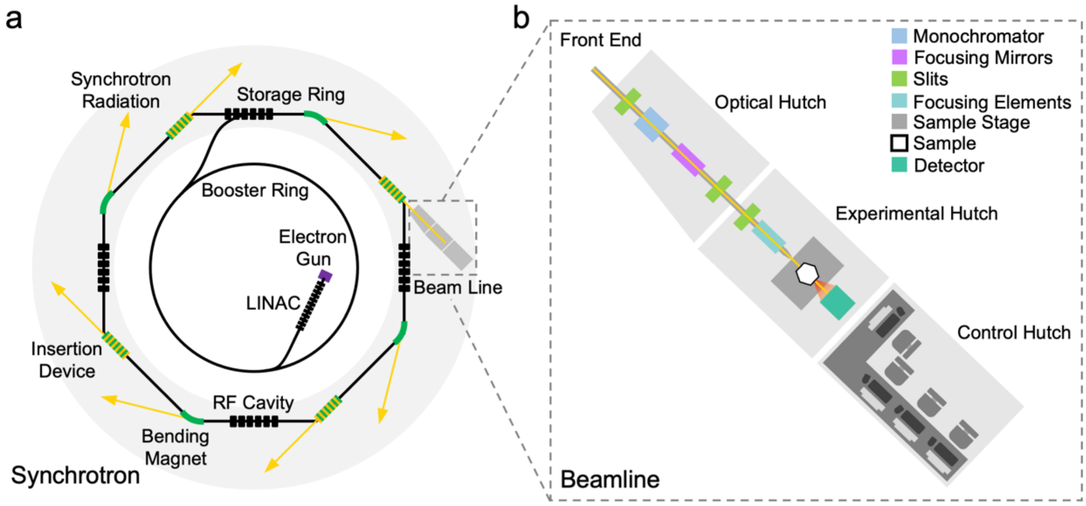

Figure 2.3. Schematics of a synchrotron. **a**) A linear accelerator (LINAC) injects high energy electrons created in an electron gun to a booster ring where they are accelerated to billions of eV. When they reach the final velocity, the electrons are injected in the storage ring, where they circulate creating synchrotron radiation. **b**) The created radiation is used in the beamlines, constituted by an optical hutch where the radiation is filtered and focused, an experimental hutch where the radiation is used, and a control hutch from where the experiment is operated.

The electrons in the storage ring follow a straight path until they encounter a magnetic field that forces them to change their trajectory. The electrons have kinetic energies of GeV, with velocities highly relativistic, i.e. very close to the speed of light. At relativistic speeds, the acceleration that electrons feel during the change in their trajectory caused by bending magnets and insertion devices results in the emission of electromagnetic radiation. During the emission of synchrotron radiation, the electrons lose energy that, if not replenished, would lead to a spiral orbit collapsing in the walls of the ring. Radiofrequency (RF) cavities supply the exact amount of energy needed to replace the lost during the emission to continue their circular orbits.

Starting with MAX IV Laboratory[12] in Lund (Sweden) and followed by SIRIUS[13] (Brazil) and ESRF-EBS[14] (France), 4th-generation synchrotrons introduced the use of magnetic arrays composed of specific combinations of dipoles, quadrupoles and sextupoles in the storage ring called, multi-bend achromats. The technological improvements in the design of these magnetic lattices led to more compact electron bunches with smaller sizes and divergence.

These new-generation synchrotrons produce high-quality synchrotron radiation characterised by:

- *High-brilliance* due to the smaller electron beam size, insertion devices can produce radiation with a much higher number of photons per solid angle per surface unit.
- *Small source size* that allows a smaller focus, which is highly beneficial for scanning methods.
- *Parallel beam*, essential for high-resolution diffraction techniques and scanning tomography.
- *Coherence* is probably one of the major features of fourth-generation synchrotrons. The beam's coherence is directly proportional to the beam size and inversely proportional to the distance measured. A coherent beam is highly desired for lens-less imaging techniques such as ptychography and coherent diffractive imaging.[15]

2.2.2. Production of Synchrotron Radiation

Apart from bending magnets, insertion devices placed in the straight sections of the storage ring are used to create high-quality synchrotron radiation, which set the beginning of third-generation synchrotron sources. Wigglers are insertion devices that could be defined as a series of bending magnets that alternatively bend the electron beam, producing synchrotron radiation in each turn. They force the electrons to oscillate in the plane of the storage ring during their path, using an array of dipolar magnets with an alternating polarity that creates a slalom forward motion. The radiation produced is enhanced by a factor of 2 times the number of wiggler periods. The spectrum of a wiggler has the same shape as a bending magnet but higher intensity due to the repetitive oscillation. Undulators share a common working principle with wigglers; however, they differ in that their spectral flux is concentrated in evenly separated bands of radiation. The radiation created in each dipole overlaps and interferes with the next. The constructive interference creates a fundamental frequency and a series of higher harmonics that can be tunned by precisely adjusting the space between magnets. The radiation cone is much narrower than the one created with wigglers and has higher intensity distributed in narrow emission peaks.

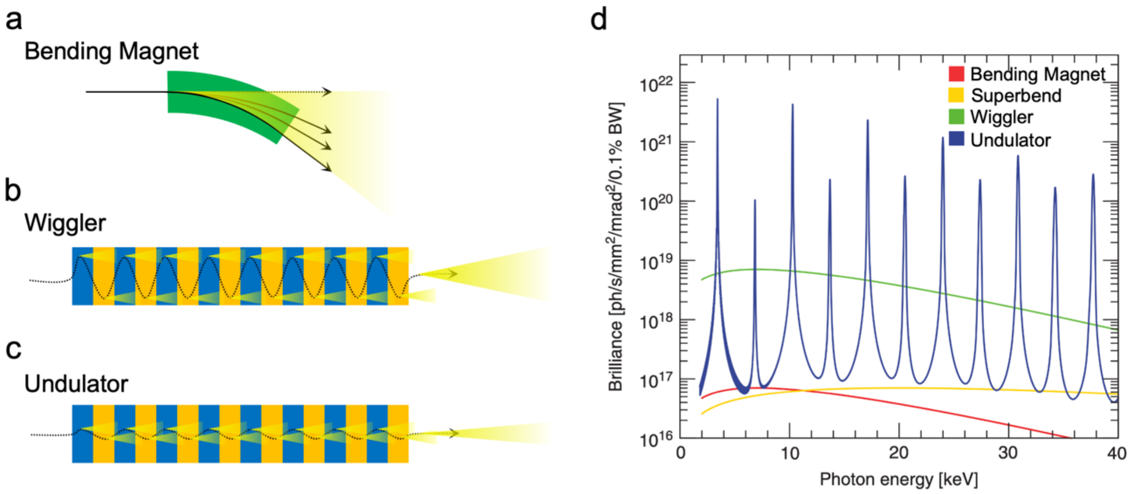

Figure 2.4. Radiation produced by a beam of relativistic electrons passing through a bending magnet (**a**), wiggler (**b**) and undulator (**c**). **d**) Comparison of brilliances at 3 GeV running at 400 mA between a bending magnet with magnetic field B = 1.41 T (red), superbend (superconducting bending magnet) with B = 4 T, a wiggler with B = 1.4 T and 100 periods (green) and an undulator U14 with K = 1.6 (blue). Reproduced with permission from Willmott[11] (Copyright 2019, Wiley and Sons).

2.2.3. Beamlines

From the user's perspective, beamlines are the point of interaction with a synchrotron. They use the electromagnetic radiation produced for all types of purposes (e.g., spectroscopy, scattering, imaging, etc.) in all different fields of science and technology. A beamline starts inside the storage ring tunnel at the front end, where the necessary components to monitor and filter the incoming radiation is. As shown in Figure 2.3b, after the front end, the optical hutch contains all the optical elements to collimate and correct the radiation beam (lenses and mirrors), select the desired beam energy (monochromators) and define the beam size (slits, lenses and zone plates). In the experimental hutch is where the experiment is carried out. There are almost infinite possible experimental setups and sample environments to be used in a synchrotron beamline. The beamline scientists and technicians constantly develop and improve the current experimental configurations for new methods and materials. Due to the high doses of ionizing radiation created during the experiments, the optical and experimental hutch is usually (but not always) shealed inside the concrete, lead and thick steel walls and doors. Therefore, the experiments are remotely controlled from the control hutch, where the users and beamline scientists operate the beamline and everything related to the ongoing experiment.[16]

2.3. X-Ray Imaging

X-rays are electromagnetic radiation with a characteristic wavelength (λ) in the range of Ångströms (1 Å = 10^{-10} m). When an X-ray beam interacts with matter, different processes can occur. Part of the incident radiation will pass through the material without detectable interaction (transmission); thus, neither the X-rays' direction nor their wavelength change. Another fraction will be absorbed and transformed into a different type of energy (e.g. heat, fluorescence emission, etc.). Lastly, a fraction will be scattered in other directions. When the scattered radiation has a different wavelength than the incident beam, it is considered inelastic or Compton scattering, which gives information about the atomic environment. Elastic scattering occurs if the scattered radiation has the same wavelength as the incident beam. The incident radiation interacts with the strongly bound electrons without energy transfer. That means that the electrons will oscillate with the same frequency as the incident radiation and, therefore, will emit photons at that frequency in all directions. The emitted waves of neighbouring atoms will result in an interference process in which radiation in the same phase will be amplified and muted in the opposite phase. That results in an interference pattern in the detector that carries structural information.

The mechanisms that form the image depend on the interaction between the X-rays and the sample. In X-ray imaging, the contrast is given by the absorption, diffraction/scattering (Section 2.3.1), phase contrast or fluorescence (Section 2.3.4).

2.3.1. Small-Angle X-Ray Scattering

Small-angle X-ray scattering (SAXS) is an analytical method to obtain structural information on materials with features in the nanometre range. In contrast with other scattering and absorption methods where the detector is placed a few centimetres from the sample, this technique is characterized by having a large distance (e.g., 2 - 50 m) between the detector and the sample. This detector placement allows for resolving the scattered radiation at lower angles resulting from a smaller scattering vector and thus gaining information on relatively large structures.

In a typical scattering experiment in transmission geometry (represented in Figure 2.5), the sample is exposed to an incident X-ray beam (defined by a vector $\overrightarrow{k_\iota}$) with wavelength λ. Upon interacting with the sample, some part of the radiation will be scattered ($\overrightarrow{k_s}$) at an angle θ, forming an angle 2θ with the incident beam. The intensity (I) of the scattered radiation is a function of the scattering angle (θ), which defines the scattering vector $\vec{q}$, defined as $\vec{q} = \overrightarrow{k_\iota} - \overrightarrow{k_s}$, which quantifies the length scale in the reciprocal space and relates with real space as shown in Equation 2.1. In the case of elastic scattering $\vec{q}$ fulfils Bragg's law in Equation 2.2.

$$q = \frac{2\pi}{d} \qquad \text{Equation 2.1}$$

$$|\vec{q}| = q = \frac{4\pi}{\lambda} sin\left(\frac{\theta}{2}\right) \qquad \text{Equation 2.2}$$

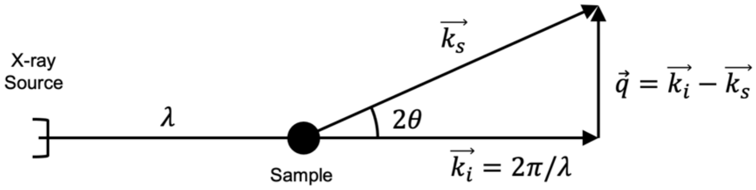

Figure 2.5. Schematic representation of a scattering experiment in a transmission set-up. The incident radiation is scattered by the atoms or materials with different electron densities in the sample.

The efficiency of the scattering process, the scattering length density (ρ), is dependent on the electron density of the atom (higher electron density means a higher number of emitters).[17] The scattering intensity $I(q)$ depends on the contrast ($\Delta\rho$), which, when using X-rays as a radiation source, is proportional to the difference between the electronic density of the sample and the environment. The intensity of the scattered radiation can also be expressed in terms of the so-called form factor $P(q)$ and structure factor $S(q)$. The form factor relates to the shape of the particle and polydispersity. The structure factor reveals the interaction between neighbouring particles, e.g. electrostatic attraction/repulsion, when the distance between particles is in the same range as the size of the particles. In concentrated ordered systems where particles align themselves with certain periodicity the scattering signal can eventually develop a pronounced peak. This maximum in the scattering intensity is then called diffraction peak, and its position reveals the distance between the scatterers according to Bragg's law (Equation 2.2).[17]

Using a 2D detector, not only the structure but the anisotropy of the material can be studied. On the one hand, as shown in Figure 2.6a, the scattering signal can be radially integrated into the whole azimuthal range, resulting in the scattering intensity along the scattering vector. This information can be used to resolve the nanostructure of the material, periodicity and average size and shape of particles or fibres. On the other hand, the scattering intensity of a specific q-range can be evaluated across the azimuthal angle, as shown in Figure 2.6c. This type of analysis carries information about the anisotropy of the material. Materials with an isotropic and homogeneous structure will produce an isotropic scattering, while materials with some anisotropy will produce an anisotropic scattering pattern.

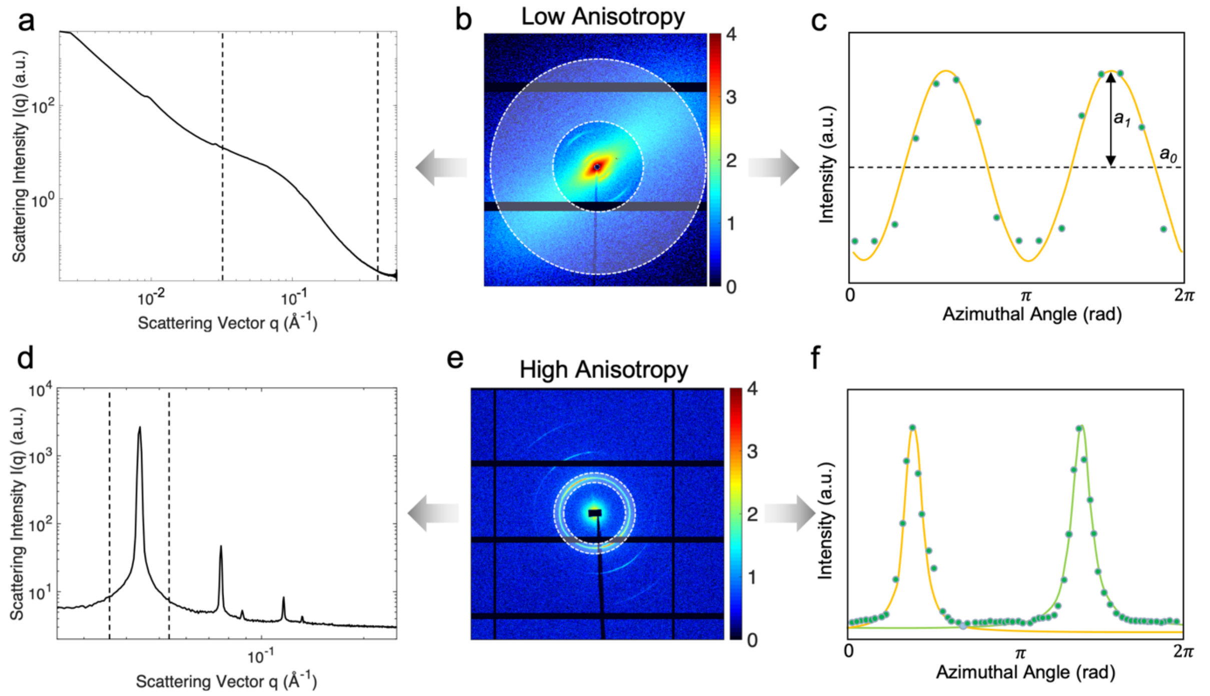

Figure 2.6. Scattering patterns of cortical bone (**b**) and lyotropic liquid crystals (**e**), showing low and high anisotropy, respectively. The analysis method in a SAXS experiment is based on the angle at which the X-rays are scattered (**a**, **d**) and their anisotropy (**c**, **f**). The signal can be integrated (**a**, **d**) to access the structural information or the azimuthal intensity evaluated to analyse the anisotropy of the material. The anisotropy can be evaluated fitting a cosine function (**c**), or calculating an order parameter (**f**).

In scattering experiments, the main orientation direction can be directly calculated from the anisotropy of the scattering pattern. The degree of anisotropy can be evaluated by the degree of orientation proposed by Bunk et al.[18] This parameter highly depends on the particle shape since a perfectly aligned ellipsoid has a less pronounced anisotropy than a perfectly aligned thin rod. In this approach, the scattering pattern is divided into N_θ azimuthal segments. The azimuthal intensity distribution can be approximated by a cosine function using the discrete Fourier transform of the intensities of each individual segment (n_θ), as shown in Equation 2.3 and 2.6c. The baseline of the function (a_0) is the symmetric intensity, given by the average scattering intensity, and the amplitude of the signal (a_1) is the asymmetric intensity, given by the anisotropy created in the scattering intensity as a result of orientation. The degree of orientation can then be defined as the relationship between the asymmetric and symmetric intensity in the scattering signal (a_1/a_0). The phase of the signal (θ_S) represents the actual angle of orientation in the reciprocal space. This method is not an order parameter, but a relative measurement of the degree of anisotropy. Some limitations are associated with the cosine approximation, which is unsuitable for highly oriented materials.

$$I \approx a_0 + a_1 \cos\left(\frac{2\pi n_\theta}{N_\theta} - \theta_S\right) \qquad \text{Equation 2.3}$$

$$Degree\ of\ Orientation = \frac{a_1}{a_0} \qquad \text{Equation 2.4}$$

The Hermans' orientation parameter instead uses the orientational order parameter discussed in Section 4.4, to quantify the anisotropy of the material.[19] The azimuthal intensity in the range -90° to 90° is normalized and interpolated by a Lorentzian curve (Figure 2.6f), centring the peak position at 0°. According to the Hermans' algorithm, the Hermans' orientation parameter $\langle f_a \rangle$ is calculated using Equation 2.5, where $I(\phi)$ is the intensity for each azimuthal angle (ϕ). The angle of the orientation is extracted by the peak position in the azimuthal intensity after the interpolation indicating the angle in the reciprocal space.[20]

$$Orientation\ Parameter\ \langle f_a \rangle = \frac{\int_0^{\pi} \left(\frac{3}{2} cos^2\, \phi - \frac{1}{2}\right) sin\, \phi\, I\phi\, d\phi}{\int_0^{\pi} sin\, \phi\, I\phi\, d\phi} \qquad \text{Equation 2.5}$$

2.3.2. Scanning SAXS

In a SAXS experiment, the scattering signal collected in the detector is the contribution of the scatterer elements in the volume illuminated by the X-ray beam (Figure 2.7a). This method is the essence of solution SAXS, which relies on collecting large statistics of homogeneous systems such as particles in solution. The problem of using large beams in potentially heterogeneous systems lies in the risk of averaging over areas with different compositions or structures. The probed area can be significantly reduced using a smaller beam, increasing the spatial resolution of the mapped system and enabling the study of changes across smaller distances (Figure 2.7b).

Scanning SAXS was first introduced in 1997 by Fratzl et al.,[21] and combined a focused beam with a sample stage able to move in the plane perpendicular to the beam to probe the reciprocal space map (RSM). The first experiments were performed using X-ray tubes, which gave a large beam diameter (~200 μm) and low flux. With the development of modern synchrotron radiation, scientists have transferred this method to large-scale facilities. Micro-focused beams were possible after developing third-generation synchrotrons, and their high flux significantly reduced the measurement time. The short exposure times make this method perfect for studying large areas with small step sizes and visualising dynamic processes such as time-resolved *in situ* experiments. Nowadays, a highly intense beam interacts with a small sample volume, and additional motors controlling the XY-plane (Figure 2.7c) raster scan the region of interest (ROI). As a result, one scattering pattern is obtained per scan point, which is eventually analysed to form the image containing the structural information about the sample. Thus, the resolution of such a method is not ruled by the wavelength of the radiation used but by the beam and scanning step size.

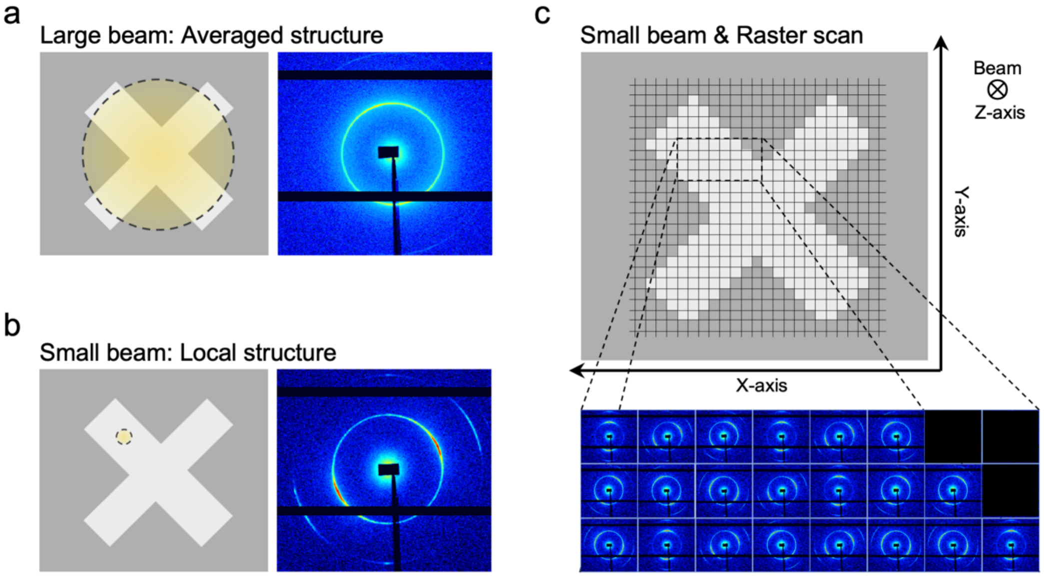

Figure 2.7. a) The scattering signal from a large X-ray beam is the contribution of the averaged structure of the system probed. **b**) Smaller beams probe smaller sample volumes, showing the local structure. **c**) Scanning SAXS uses a focused beam and a raster scanning set-up to collect the scattering pattern in each point, reaching a spatial resolution.

2.3.3. SAXS Tensor Tomography

Scanning SAXS is limited to thin slices of materials and can only provide information on the 2D projection of the orientation. Since it can only probe a two-dimensional section of the three-dimensional reciprocal space map (RSM), it lacks information about the 3D anisotropy. New tomographic methods have been recently developed combining SAXS and tensor tomography to obtain a three-dimensional reconstruction of the RSM.

In contrast with traditional tomographic methods, SAXS tensor tomography attempts to reconstruct the tensor in each voxel to represent the reciprocal space map and retrieve the structural and orientational 3D information. Traditional tomography, such as absorption X-ray tomography, reconstructs a scalar in each volumetric element (voxel). For that, the sample is rotated with respect to the X-ray source in a rotation axis perpendicular to the beam. Each reconstructed slice is orthogonal to the rotation axis and can be reconstructed independently from the rest. Anisotropic materials contain structural elements such as particles, fibres or crystals with a non-uniform electron density distribution in all directions. A scalar value cannot represent the structural and orientational information, and reconstructing a tensor is thus needed. In general, the projections of such tensors are not invariant under rotation about the tomographic axis, and can therefore not be constrained without an additional degree of freedom, such as another axis of rotation (tilt) perpendicular to the other one (Figure 2.8a).[22, 23]

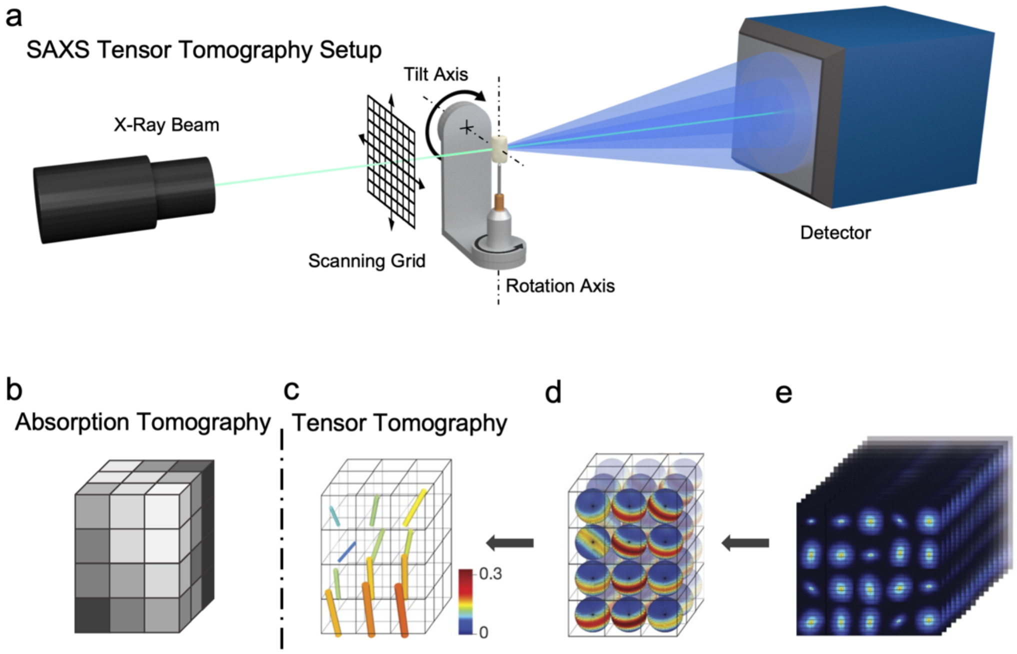

Figure 2.8. a) Schematic representation of the experimental set-up for SAXS tensor tomography. The reconstruction method differs from conventional absorption tomography (**b**), in that a tensor is reconstructed in each voxel (**c**) instead of a scalar. The reconstruction is done using a set of spherical harmonics (**d**) from the 2D projections of the sample at different orientations (**e**). Adapted with permission from Liebi et al.[22] (Copyright 2015, Nature Publishing Group).

There are several approaches for reconstructing the tensor of the 3D RSM.[24-26] The method developed by Liebi et al.,[15] as schematically shown in Figure 2.8b, uses a set of 2D SAXS projections of the sample at different rotations and tilts to reconstruct the anisotropy of the RSM by a superposition of spherical harmonics (SH). In each projection, a 2D slice of the RSM is collected, containing information about the structure and the projected 3D orientation. This method reconstructs two angular parameters representing the principal nanostructure orientation and a set of spherical harmonics coefficients representing the shape of the RSM in each voxel. The parameter optimisation is done by minimising the error between the intensities measured and predicted by the model for all projections.[6] This method only considers the real spherical harmonics (Y_m^ℓ) with cylindrical symmetry of even order (ℓ) and degree ($m = 0$), which represent the point-symmetric orientations. To overcome the limitations of this model, new approaches recently developed by Nielsen et al.[27,28] implements the use or real unrestricted spherical harmonics (RUSH) with order ℓ and degree $m = \ell_{max}$. This new approach to the SH method, used in the content of this thesis, offers more robust reconstructions and a wider variety of reciprocal space maps than the previous model restricted to only cylindrical symmetries.

2.3.4. X-Ray Fluorescence Spectroscopy

Spectroscopy techniques measure the response of a material as a function of energy. The energy scanned in the measurement can be either from the incoming beam or the energy from the outgoing particles produced by the sample. X-ray fluorescence spectroscopy (XRF) is a non-destructive technique to determine the elemental composition of a sample by measuring the fluorescence of its atoms excited by a monochromatic X-ray beam. It is a surface-sensitive technique suitable for all types of materials and requires very little to no sample preparation.

In fluorescence, an absorbed X-ray photon excites and ejects a core electron from an inner shell of the atom (Figure 2.9a). The ejected electron leaves a hole that will be occupied by an electron from a more external shell in the further relaxation process (Figure 2.9b). The excess energy during the relaxation from the higher to the lower state will be emitted as a photon. The energy of the emitted photon corresponds to the energy difference between the initial and final energy states of the electron, and it is denoted by the shell where the electron falls (K, L, M, etc.), and the transition from the level where the electron comes from ($L \rightarrow K = \alpha$, $M \rightarrow K = \beta$, $M \rightarrow L = \alpha$, etc.).[29]

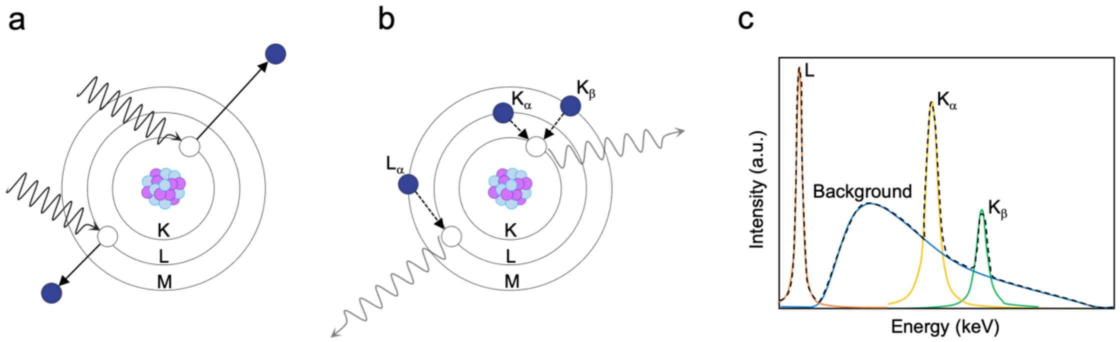

Figure 2.9. The fluorescence phenomenon happens when a photon has enough energy to eject a core electron (**a**). The vacancy left is then occupied by an electron from a higher shell, releasing the excess of energy as a photon (**b**), and creating characteristic emission lines in the fluorescence spectrum (**c**).

XRF provides qualitative and quantitative information. The chemical composition is reflected in the characteristic emission lines in the spectrum, and the element quantity can be extracted with the help of calibration materials and reference targets. The XRF spectrum is composed of a broad continuous background coming from the electron collisions with the atoms and highly intense emission lines from each element exited by the incoming radiation (Figure 2.9c). Since the emitted radiation has lower energy than the absorbed one, the energy of the incoming photons defines the upper detection limit. Even though there is no real lower detection limit, light elements emitting low-energy photons are technically challenging to detect since the atoms in the atmosphere easily absorb the emitted radiation. This method can be easily combined with the current scanning set-ups to identify a sample's local fluorescence signal. This way, valuable spatial resolution can be achieved, creating element distribution maps.[30]

The detector that collects the fluorescence signal can be a source of artefacts affecting the final spectrum. Scape peaks are created when the fluorescence photons produce fluorescence in the detector. An emitted photon can lose part of its energy, exciting the atoms in the detector and emitting their corresponding fluorescence photon. As a result, the detector will count a fraction of photons with lower energy, resulting in two peaks: the emission line and the escape peak. The energy shift is equivalent to the emission line of the elements in the detector. Another common artefact is pile-up peaks, created when several photons hit the detector at the same time (or below the read-out time of the detector). Those two photons produce an electrical signal detected as a single photon with an energy equal to the sum of the energy of the incoming photons.[31]

2.4. Birefringence Microscopy

The optical property of a material with a refractive index that depends on the polarisation and propagation direction of the light is called birefringence. Birefringent materials are optically anisotropic materials with a defined optical axis. They are characterised by having a double refractive index dependant on the polarisation state of light, producing, as a result, a double transmitted ray with two different refraction angles (see Figure 2.10). One of the two beams of light travels through a shorter path and, therefore, faster, which is called the *ordinary* ray. The other beam depends on the propagation direction, taking a longer path and travelling slower, which is called the *extraordinary* ray. The ordinary ray will reach the highest velocity when the polarisation state is parallel to the optical fast axis, indicating the optical anisotropy direction. Birefringence (B), in Equation 2.6, is then the difference between the extraordinary (n_e) and the ordinary (n_o) refractive index. The ordinary ray will reach the highest velocity when the polarization state is parallel to the optical fast axis, which indicates the direction of the optical anisotropy.

$$B = |n_e - n_o| \qquad \text{Equation 2.6}$$

The relationship between the phase (δ) of both transmitted waves is calculated through the retardation (Γ). The retardation measures how much the slow ray will be retarded with respect to the fast ray due to the orthogonal polarisation between both rays. It can be calculated considering the birefringence and the thickness (*t*) of the sample as:

$$\Gamma = t \cdot |n_e - n_o| \qquad \text{Equation 2.7}$$

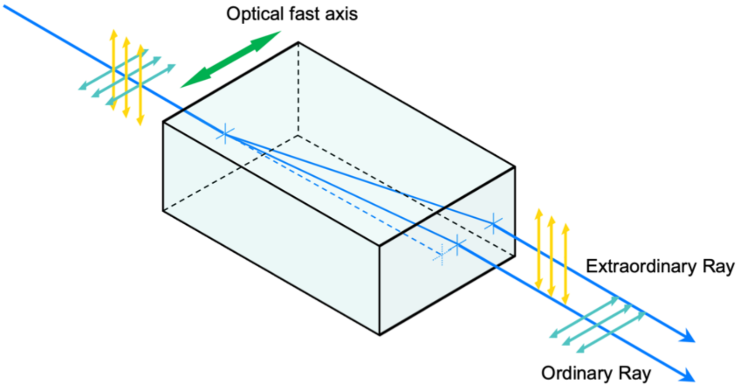

Figure 2.10. Scheme of the birefringence principle in an optically anisotropic material. The incident ray is split in two rays with different optical paths and polarization angles depending on the optical fast axis of the material.

In practice, the birefringence of a material can be determined by studying the polarisation states of the light before and after interacting with an optically anisotropic material. The Stokes vector ($\vec{S}$) describes the polarisation state of electromagnetic radiation, composed of four Stokes parameters. The Stokes parameters describe not only polarised but also unpolarised or partially polarised light. As shown in Equation 2.8, the first parameter, S_0, describes the total intensity of the light; the second parameter, S_1, the degree of light that is linearly horizontal/vertical polarised; the third parameter, S_2, the degree of polarization in ±45°; and the fourth parameter, S_3, the degree of right-/left-handed circular polarisation.[32, 33]

$$\vec{S} = \begin{pmatrix} S_0 \\ S_1 \\ S_2 \\ S_3 \end{pmatrix} = \begin{pmatrix} E_{0x}^2 + E_{0y}^2 \\ E_{0x}^2 - E_{0y}^2 \\ 2E_{0x}E_{0y}\, cos\, \delta \\ 2E_{0x}E_{0y}\, sin\, \delta \end{pmatrix} \qquad \text{Equation 2.8}$$

The polarisation state of the light will change after interacting with an optically anisotropic material. An incoming wave with initial polarisation state $\vec{S}$, interacting with a material, is linearly related to the output wave with state $\overrightarrow{S'}$, by a 4×4 transformation matrix, known as Mueller matrix (Equation 2.9). Thus, an optical element that interacts with the polarisation state of light can be represented by its respective Mueller matrix (M).[33, 34]

$$\begin{pmatrix} S_0{}' \\ S_1{}' \\ S_2{}' \\ S_3{}' \end{pmatrix} = \begin{pmatrix} M_{11} & M_{12} & M_{13} & M_{14} \\ M_{21} & M_{22} & M_{23} & M_{24} \\ M_{31} & M_{32} & M_{33} & M_{34} \\ M_{41} & M_{42} & M_{43} & M_{44} \end{pmatrix} \times \begin{pmatrix} S_0 \\ S_1 \\ S_2 \\ S_3 \end{pmatrix} \qquad \text{Equation 2.9}$$

The result of an incoming beam of light with initial polarisation state $\vec{S}$, passing through a series of optical elements with Mueller matrix M_1, M_2, …, M_n, and coming out with polarization state $\overrightarrow{S'}$ can be described as:

$$\overrightarrow{S'} = M_n\left(\dots\left(M_2\left(M_1\vec{S}\right)\right)\dots\right) = M_n \dots M_2 M_1 \vec{S} \qquad \text{Equation 2.10}$$

This principle allows birefringence microscopy to measure the changes in the polarisation of light passing through a sample. It uses a combination of polarisers and photoelastic modulators (PEM) to calculate the Stokes parameters of the outcoming light beam.[35] It retrieves the change in the polarisation angle (θ) and the phase difference (δ) of the ordinary and extraordinary waves using the Mueller matrix of the optical components, as described in Equation 2.11.

$$M_{PEM} = \begin{pmatrix} 1 & 0 & 0 & 0 \\ 0 & cos^2(2\theta) + sin^2(2\theta)\,cos(\delta) & cos(2\theta)\,sin(2\theta)\,(1 - cos(\delta)) & -sin(2\theta)\,sin(\delta) \\ 0 & -cos(2\theta)\,sin(2\theta)\,(1 - cos(\delta)) & cos^2(2\theta)\,cos(\delta) + sin^2(2\theta) & cos(2\theta)\,sin(\delta) \\ 0 & sin(2\theta)\,sin(\delta) & -cos(2\theta)\,sin(\delta) & cos(\delta) \end{pmatrix}$$

Equation 2.11

The retardance of the sample (Γ) (Equation 2.12) and angle of the optical fast axis (θ) (Equation 2.13) can the therefore obtained using the appropriate elements of the Mueller matrix.[36, 37]

$$\Gamma = arctan\sqrt{(M_{24}/M_{44})^2 + (M_{34}/M_{44})^2} \qquad \text{Equation 2.12}$$

$$\theta = \frac{1}{2}arctan(M_{24}/M_{34}) \qquad \text{Equation 2.13}$$

Birefringence in biological and polymeric materials is the consequence of the optical anisotropy caused by the orientation of molecular chain segments in what is called intrinsic birefringence.[38-40] At a higher hierarchical level, ordered arrangements of optically isotropic (or anisotropic) materials with different refractive indexes can lead to effective birefringence if the feature size is smaller than the wavelength.[33] Supramolecular organisation can produce form birefringence when particles with anisotropic shapes are in a media with a different refractive index. Isotropic structures such as polymeric micelles are not birefringent; however, more complex structures such as fibrillar proteins like collagen, agglomerations of micelles, cylinders and worm-like micelles, and crystal-like structures with anisotropy in at least one dimension can develop optical anisotropy.[41, 42]

Chapter 3

Biological Hierarchical Materials

Hierarchical structure refers to an arrangement of items in a structured organisation with different levels of importance or at different length scales. In natural sciences and engineering, hierarchical materials are associated with structures in which there is an organisation in different sublevels, each composed of different subunits. Each of these subunits forms the building blocks for the next level and may have different physical and/or chemical properties than the units of the levels above or below. Thus, hierarchical materials need to fulfil two requirements. First, its building blocks must be present in more than one length scale. Second, the properties of the different structural units have to be different but have complementary functionality. That can be fulfilled by creating an arrangement of subunits of the same material but different dimensions or units of different materials in a composite.[43]

3.1. Hierarchical Structures in Nature

Hierarchical materials are widely found in nature, from dendritic mineral growth, structural support in biology or unique abilities and functionalities in plants and animals.[44] These hierarchical materials are often created by self-assembly mechanisms perfectioned during thousands of years of evolution and adaptation to the environment. One fascinating example of a material structured in a hierarchy is gecko pads and their adhesion on rough surfaces without the use of any secretion or adhesive. The adhesion is due to Van der Waals interactions created by thousands of nanoscopic fibres on the surface. As illustrated in Figure 3.1a-b, the pads of geckos are composed of several structures which contain thousands of hair-like structures called *setae*. Each *seta* is also composed of hundreds of fibrillar endings called *spatulae* which multiply the active surface area in contact with the walking surface, adapting to its roughness. Researchers and engineers use these structures to inspire new materials with exceptional functionalities.[45] Gecko pads use one single material hierarchically structured in different levels and length scales to obtain a completely new functionality, impossible to obtain by the same material in the bulk state.

On the other hand, materials with different properties can be combined to create composite hierarchical structures with high adaptability and performance. The mineralised tissue found in mollusc shells is an example of a natural composite material. Even though there are several types of mollusc shells, nacre is one of the most studied due to their extraordinary mechanical properties. Nacre is a layered structure of polygonal calcium carbonate platelets, as represented in Figure 3.1e-f, which constitutes about 95 – 99.9% of the total shell weight. In between those mineral platelets, there is an organic phase formed of proteins and polysaccharides that keep the plates together.[46] The plates in nacre adopt a brick-wall structure with high toughness. The primary toughness mechanism of nacre is crack deflection. The discontinuous brick structure of flat ceramic platelets deflects the crack perpendicular to the stress direction, and the adhesion between the mineral and the polymer matrix prevents crack propagation and delamination.[47, 48]

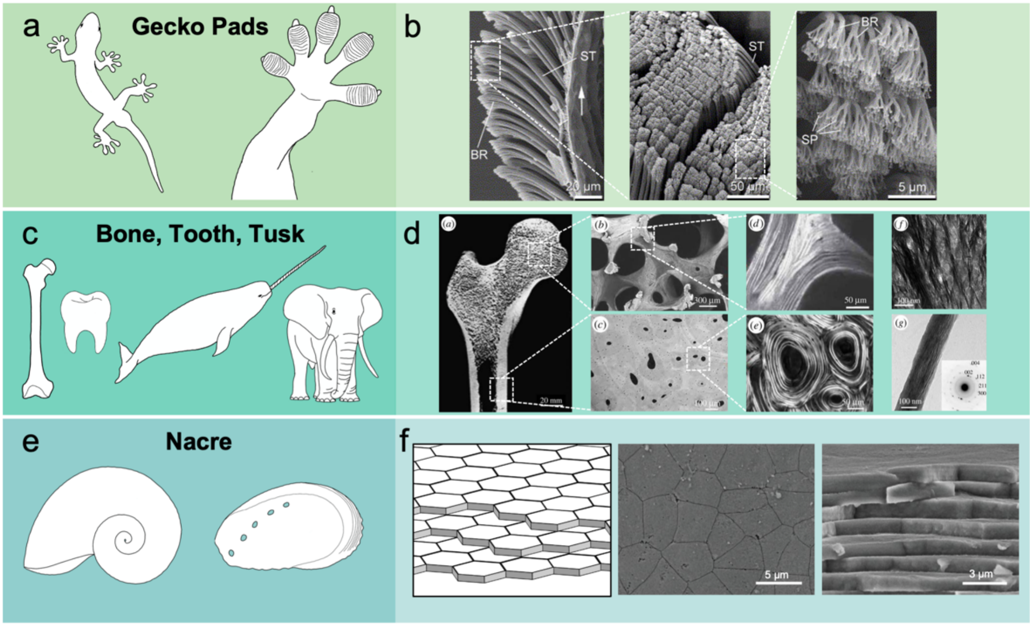

Figure 3.1. Hierarchical biological structures in nature. **a**) Gecko pads have a hierarchical structure that confer them extraordinary adhesion. **b**) The surface of the pads is covered with hundreds of microscopic *setae* (ST), which have hundreds of *spatulae* (SP). **c**) Mineralised tissues such as bone, tooth and tusk use a combination of composite materials and hierarchical structures. **d**) In bone, compact and porous structures share a common microstructure of layered bone lamellae, made of the same building blocks: mineral particles and collagen fibres. **e**) Mollusc shells made of nacre are examples of composite materials. **f**) Calcium carbonate platelets are assembled in a brick-wall structure. A polymeric matrix keeps them in place and attached to each other. This combination of ceramics and polymers create a very though material with high resistance to impacts and crack propagation. Adapted with permission from Gao et al.[49] (Copyright 2005, Elsevier), Georgiadis et al.[50] (Copyright 2016, Royal Society) and Mao et al.[51] (Copyright 2016, American Association for the Advancement of Science).

Mineralised tissue such as bones, teeth and tusk use both strategies: composite materials as in nacre, assembled in a hierarchical structure with multiple architectures at different length scales as in the gecko pads. Collagen fibres and calcium phosphate nanoparticles constitute the basic building blocks for these types of mineralised tissues at the nanoscale, creating a composite material. Collagen fibres are mineralised with calcium phosphate particles, which are later assembled in bundles, organised in larger structures depending on the tissue they are part of. In the microscale, bone has either compact (cortical) or very porous structures (trabecular), which distribute the mechanical load depending on the needs of the bone (Figure 3.1c-d).[1] Tooth and tusk are made of dentine, cementum and enamel, which combines the same two basic building blocks in different proportions and architectures (except for enamel, which does not contain collagen but other proteins).[52] This wide variety of microscopic structures are based on the same nano constituents. They are part of one of the main structures in our bodies, which make them very interesting to be studied, for relevant applications in medicine and society.

3.2. Building Blocks of Mineralised Tissue in Mammals

Mineralised tissues in mammals belong to a family of materials that can be considered composites with two phases, polymeric fibres and mineral particles. Most mineralised tissues in mammals share the same basic ingredients: collagen and hydroxyapatite. Their complex organisation and adaptability make it possible to find multiple arrangements that offer extraordinary mechanical properties.

Collagen is one of the most important proteins and structural biopolymers, as it is a key component in many tissues such as tendons, ligaments, skin, and bone. There are more than twenty types of collagens composed of at least 46 different polypeptide chains; however, in this chapter, only types that create fibrillar collagen are considered. In particular collagen type I is the most relevant form of fibrillar collagen for the tissues described in this section. The feature that gives fibrillar collagen its characteristics is the different hierarchical levels in its structure. Collagen is formed of three polypeptide α-chains (0.5 nm diameter) folding in a left-handed triple helix called tropocollagen (1.24 nm diameter),[53] with a pitch of about 10.4 nm and about 300 nm in length.[54] As shown in Figure 3.2, groups of five triple helices assemble in a parallel conformation with an offset between each other forming microfibrils, which are organised in fibrils of variable diameters and lengths depending on the tissue they form. The collagen structure has a periodicity of 67 nm (D-period) along the molecule axis, with a 40 nm gap between the ends of the molecules and a 27 nm overlap region with the adjacent molecules.[55] Collagens have functional groups capable of interacting with calcium and phosphate ions, the two main groups forming the mineral particles.[56]

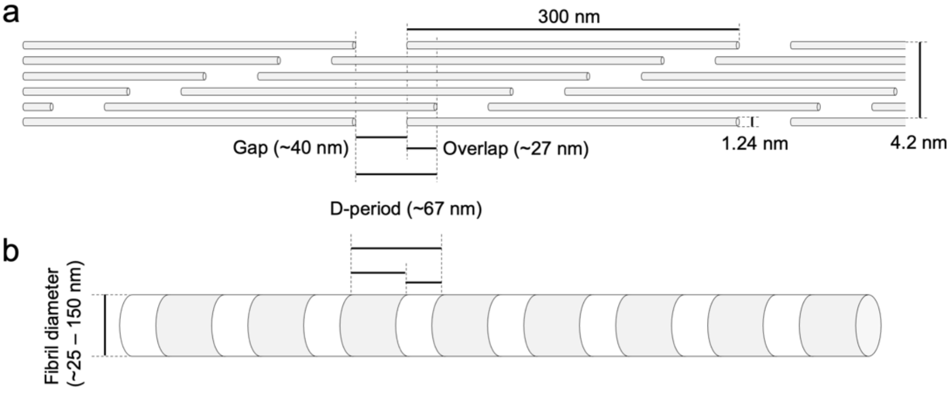

Figure 3.2. Morphology of collagen fibrils. **a**) Tropocollagen is arranged axially with a gap between microfibrils of ~27 nm and parallelly with an overlapping of ~40 nm, which forms a staging period of ~67 nm (D-period). Multiple ordered microfibrils create a collagen fibril (**b**) with a diameter of variable dimensions depending on the tissue they form.

The mineral phase present in bone is a form of calcium phosphate related to the hydroxyapatite family ($Ca_{10}(PO_4)_6(OH)_2$), with a significant amount of carbonate CO_3. There are also small amounts of Ca^{2+} and OH^- deficit, substituted by other cations (H, Na, Mg, K) and anions (F, Cl).[55] The carbonated hydroxyapatite forms crystals with a hexagonal unit cell and platelet-like shapes. Several studies have shown that the crystal size of the platelet particles varies along the different species and tissues, but they are approximately 30 – 50 nm in length, 20 – 30 nm wide and 1.5 – 4 nm thick.[50] In the last years, researchers have shown that the mineral particles are formed of fractal aggregates instead, offering a new perspective on this system. The mineral phase comprises needle-like particles that eventually merge laterally, forming platelet-like particles.[57] The carbonated hydroxyapatite forms after the collagen matrix has been secreted by the osteoblasts. They nucleate in the collagen gaps within the fibrils and on the fibril surface. The crystals in the fibril gaps have their c-axis oriented in the fibril direction.[58, 59]

Beyond the triple helix and the mineral particles, the properties and functionality of mineralised tissues depend on the organisation of those two components at the nano and microscale. It is difficult to generalise in these terms since there is a broad distribution of mineral densities in bones and teeth; however, there are some shared features across most mineralised tissues. The collagen fibres are organised into fibrils of about 80 – 120 nm in diameter.[55] Crystals of carbonated hydroxyapatite nucleate and grow from amorphous clusters within the gaps of the collagen fibrils (interfibrillar) and on the surface (extrafibrilar), forming the mineralised collagen fibrils.[60] The formation of this structure is steered by the nucleation of anisotropic particles in the collagen matrix and the functional groups of collagen molecules, where collagen type I plays a fundamental role.[61] This hierarchical structure is the primary building block of the higher order structures. Bone and tooth, described in the following sections, are composed of mineralised collagen fibrils, whether they form ordered or disordered tissue.[62]

3.3. Hierarchical Structure of Bone

Bone is a complex tissue and part of the muscoskeletal system, which plays and important structural and metabolic function. Bone is made up to 25 – 30 %wt. of protein, mainly collagen type I, and calcium phosphate particles, making the remaining 70 – 75 %wt. Bone also serves as an important reservoir of metabolic ions such as calcium and phosphates, which play an essential role in signalling and energy storage. To keep the ion balance regulated, bone needs to interact with many other organs like liver, muscles or kidneys, interacting through hormones. The tissue in bone is constantly being remodelled in response to mechanical load throughout life. Several cell types are responsible to maintaining bone tissue, but the most important include osteoblast, osteoclast, osteocytes and mesenchymal stem cells. While osteoblasts create new bone, osteoclasts are responsible for bone resorption, maintaining a fine balance between the amount of tissue created and dissolved. When either deposition or resorption dominates, several problems can emerge creating bone fragility.

Osteocytes are found embedded in the mineralised matrix of bone forming an interconnected network. They are believed to be embedded osteoblasts in a terminal differentiation. They are responsible for releasing factors to regulate the remodelling process depending on mechanical load. Mesenchymal stem cells are in the bone marrow and they are a source of progenitor cells.[63] The bone matrix acts as a scaffold for the formation of bone tissue and it is composed of organic and inorganic materials. A large number of collagen fibres secreted by osteoblasts form the organic matrix, which also contains small amounts of hydroxyapatite crystals that will eventually form new mineralised tissue.[64]

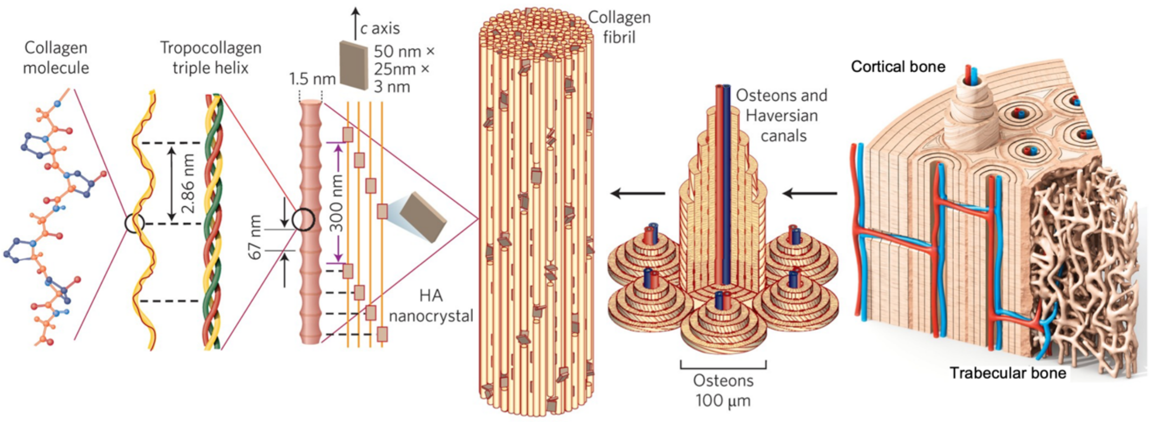

Figure 3.3. Hierarchical structure of bone. Cortical and trabecular bone are composed of osteons, which have a lamellar structure. Each individual lamella consists of an arrangement of fibres made of several mineralised collagen fibrils. Fibrils are made of collagen protein molecules composed by three chains of amino acids and hydroxyapatite nanoplatelets. Adapted with permission from Wegst et al.[1] (Copyright 2015, Nature Publishing Group).

Those building blocks are assembled in a composite material with two different structures: cortical and trabecular bone. The microscopic structure of cortical and trabecular bone is composed of osteons. In cortical bone, the osteon structure is known as Harvesian system. It contains a central Harvesian canal with blood vessels and nerves, surrounded by concentric layers of bone or *lamellae*. Uniformly spaced in the bone layers, there are lenticular cavities called *lacunae*. From these cavities, *canaliculae* branches radially in all directions, penetrating through the bone layers and creating a continuous network of cavities.[65] In trabecular bone osteons are referred as bone packets which consists of bone layers stacked, separated by cement lines. At a smaller length scale, cortical and trabecular bone present tissue with a woven or lamellar structure. Woven bone has a disordered collagen fibril arrangement. It is a sign of newly created or immature bone, which gradually turns into lamellar bone. Lamellar bone has an organised arrangement of collagen fibrils into layers or *lamellae* and it is a sign of mature tissue.[66]

Macroscopically, cortical bone appears at the outer part of long bones, and it has a dense structure. It makes approximately 80 %wt. of the total skeletal mass. It has high compressive strength contributing to most of the mechanical support. Even though it is solid, it contains small pores that allows vascular and neural supply. Trabecular bone has a very porous structure (pore volume up to 50 – 90 %) made of a network of interconnected small structures called *trabeculae*. Its sponge-like structure decreases the compressive strength to 1/10 compared with cortical bone, however it has a high surface area for the red bone marrow, provides internal support, and distributes the mechanical load.[50, 66]

3.4. Hierarchical Structure of Tooth and Tusk

Teeth and tusks are the strongest tissues in mammals and are designed to withstand enormous mechanical stresses and resist during the whole life span of the individual. Similar than bone, tooth and tusk are created of an organic matrix, mainly collagen, mineralised with hydroxyapatite nanoparticles. Those two components are assembled on the microscale, forming three very different structures: enamel, dentine, and cementum. In addition, the inner part of teeth and tusks have the pulp, a soft tissue containing cells, nerves, and blood vessels directly connected with the bloodstream. Teeth and tusks have two differentiated regions: the root, which is attached to the jawbone, and the crown, facing the outside. The root is attached to the bone by the connection of the cementum and the periodontal ligaments. The crown is covered in enamel in tooth; however, tusks often have different morphologies and may have enamel, cementum or only dentine.

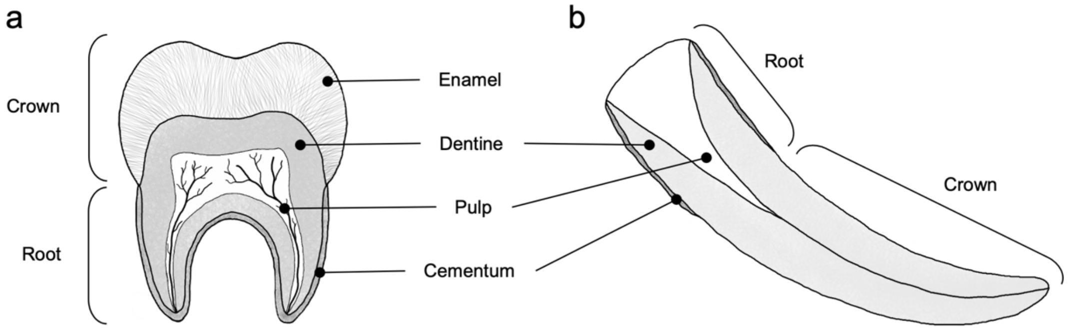

Figure 3.4. Schematic representation of the structure of tooth (**a**) and tusk (**b**). Tusks often do not have enamel, and the crown is mainly composed of dentine. The structure of dentine varies extensively between different species, but it is generally composed of dentine tubules with different microscopic arrangements. The cementum is a thin layer covering the root in contact with the ligaments that attach the tooth and tusk to the bone.

Tusks are a form of elongated teeth that extend out of the mouth of the individual due to continuous growth. Tusks generally have the same structure of enamel, dentine and cementum as teeth, but they have an elongated pulp chamber with an extensive blood supply to support the constant growth.[67] In contrast with teeth, tusks are exposed to the environment suffering dehydration, temperature changes, high salinity in marine environments and constant wear with the surroundings. Very limited or no enamel is present on the surface. The vast majority of the tusk is then formed by dentine (known as ivory), which has different patterns in different species.[68, 69]

Enamel is the hardest material in mammals and has several functions such as mechanical support, chemical barrier, and friction and fatigue resistance. Contrary to other mineralised tissues such as bone, the enamel is acellular and therefore cannot be repaired or remodelled by the organism. Enamel is found in the crown, and it is made of a mineral phase (95 %wt.), an organic matrix (1 %wt.) and water (4 %wt.). The mineral phase is composed of carbonated hydroxyapatite reported to be platelet- or needle-like crystals of approximately 50 nm in width and several tens of microns in length.[52, 70] The crystalline needles run parallel, assembled into rods of 4 – 6 μm in diameter, oriented with the c-axis along the rod axis. The rods are then wrapped in a sheath of an organic matrix that, contrary to the rest of the tooth and bone, does not contain collagen but other proteins. The actual organisation of enamel is not fully understood, and it appears to vary between different species with a wide combination of shapes. In humans, enamel appears to be formed of rods oriented perpendicular to the surface, which degenerates to a woven pattern towards the dentine junction.[71, 72] In other mammals, such as mice, the rods are parallel to each other in layers with alternate orientations at 60° from each other,[73] and in bovine enamel, the crystals in a rod are not parallel, but they twist like fibres in a wool thread.[74] Generally, enamel and dentine are connected via the dentoenamel junction, a transition zone where the different microstructures meet, and mechanical load is redistributed.

Dentine is the main material in teeth and tusks and is created by dentine-producing cells called odontoblasts. Dentine is less mineralised than enamel, containing approximately 70 %wt. of minerals, 18 %wt. of the organic matrix, mainly collagen type I, and 12 %wt. of water.[72] The mineral crystals in dentine are made of hydroxyapatite, comparable to the ones found in bone, with platelet-like shapes between 2 – 4 nm in thickness, 30 nm wide and up to 100 nm long.[75] They are highly associated with the organic matrix, with the c-axis parallel to the collagen fibril axis. The organic matrix in dentine comprises collagen fibrils of approximately 10 μm in length, such as the ones found in bone. They form a fibrillar mesh that controls the deposition and orientation of the mineral crystals.[76] The mineralised collagen fibrils have a more isotropic distribution close to the pulp chamber, reaching a high degree of anisotropy with increasing distance from the pulp.[77] The dentine microstructure is composed of tubular structures (2 – 10 μm in diameter) distributed radially from the pulp chamber. Those tubules are formed by tall columnar cells called odontoblasts. They mineralise the dentine in an inwards process towards the pulp chamber. The collagen structure in the tubules has a helical-like structure[76] with a higher mineral content around the tubules than in the intertubular space. There is a decrease in the particle thickness in the intertubular space and areas close to the pulp chamber.[78]

Cementum is a thin layer in the root of the tooth and tusk between the root dentine and the bone, which makes it difficult to study. It covers the dentine and plays a significant role in impact absorption and the attachment of the tooth/tusk to the bone.[79] Cementum comprises 65 %wt. of mineral particles, 23 %wt. of an organic matrix (90 %wt. collagen), and 12 %wt. water. There are two types of cementum. Cellular cementum is deposited and mineralised by cementoblasts and has an organised lacunar structure. It has a structure similar to bone with a lamellar and trabecular bone-like structure. In contrast, acellular cementum has no cell presence and a non-organised structure. Cementum joins with dentine in the cementum-dentine junction. In this transition zone, two materials with similar compositions but very different microstructures merge, which makes it a material of high interest. In this region, there is a low content of minerals and a high content of fibrillar collagen and other proteins such as proteoglycans, which contribute to the adhesion, stability of the components and stress release.[80]

3.4.1. An Anomaly: Narwhal Tusk

External dentitions, as seen with elephant tusks, are uncommon, but the narwhal stands out as the rarest due to its impressive, straight spiralled tusk. Narwhals are odontocete (i.e., toothed) whales that inhabit the Atlantic area of the Arctic Ocean. Narwhals have two pairs of maxillary teeth; one of each develops into elongated teeth, and the other pair remain vestigial. In males, the left elongated tooth grows and becomes a tusk, protruding the maxillary bone and facial skin with a left-hander spiral structure (Figure 3.5a). The right tooth in males and both in females remain inside the skull;[81] however, irregularities in the process are frequently seen. Females may have a tusk; males occasionally have no tusk, and, in some cases, both teeth develop as tusks (Figure 3.5b).[82]

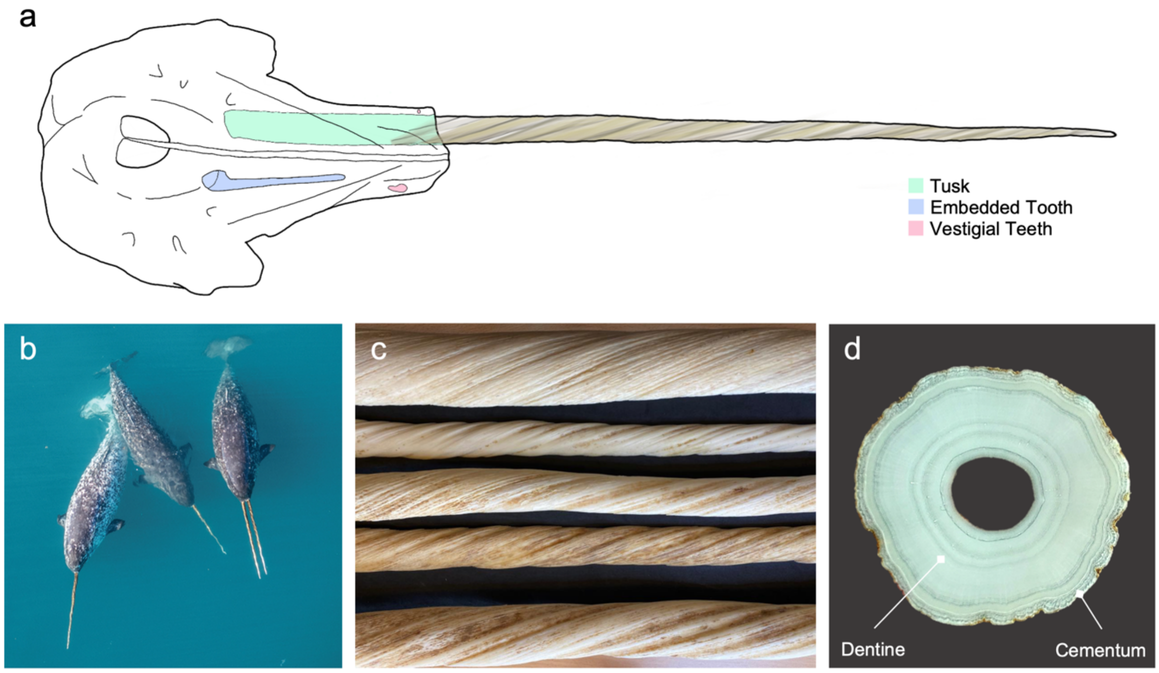

Figure 3.5. Narwhals and their tusks. **a**) Schematic representation of a narwhal skull and teeth. Females have one pair of vestigial teeth and another pair of embedded teeth. In males. The left embedded tooth develops into a tusk, which also creates a high distortion in the shape of the skull. **b**) Group of narwhals with a rare double tusked specimen in Qaanaaq, Greenland (June 2021). **c**) Detail of narwhal tusks of different sizes showing their left-hand chirality. **d**) Cross-section of a narwhal tusk. The outer cementum layer and the inner dentine are visible, the second showing the characteristic yearly growth layers. Adapted with permission from Garde et al.[80] (Copyright 2022, Polar Research).

Narwhal tusks twist in a left-handed spiral with a pitch of about 44 cm,[83] as seen in Figure 3.5c, which grows during the animal's whole life, reaching lengths of up to 3 m. Such macroscopic chirality is extremely rare, especially in bilateral animals like mammals. Narwhal tusks are composed of a central pulp chamber surrounded by primary dentine. However, unlike other tusks, the surface does not contain dentine, but it is covered by a layer of cementum (Figure 3.5d).[81, 84] They contain an intricated network of nerve endings that is hypothesised that could serve as a sensory tool for pain but also chemicals or salinity.[85] This would give a biological advantage to males; however, no difference in the swimming capacity or survival has been seen between males and females.[81] That together with the fact that a large variation in tusk length points to the fact that the narwhal tusks are sexually selected.[86] The dentine in narwhal tusk has been reported to be less mineralised and softer than other mammals.[87] The highly anisotropic structure dramatically impacts the mechanical properties of the narwhal tusk. When split along the long axis, a large torsional force is manifested, resulting in a twist along the tusk of no less than 90°.[83] The details of its nano and microstructural characterization are further discussed in Section 6.1 and in ***Paper IV***.

The origin and formation mechanism of the narwhal tusk is still unknown; however, their exceptional mechanical properties suggest that its macroscopic chirality could be repeated at lower length scales down to the most basic components, collagen and hydroxyapatite. These mineralised tissues with complex hierarchical structures are advanced composite materials. Their complex architectures often expand from the nano to the macroscopic 3D structures. To understand such hierarchical materials, experimental tools spanning several length scales from atomic to micrometre must be combined, which remains a significant challenge, but can inspire a new generation of materials for future generations.

3.5. Techniques to Study the Ultrastructure of Mineralised Tissues

The structure of mineralised tissues can be investigated by studying the orientation of each of the individual components: the crystalline lattice, the mineral particles, the collagen fibrils and the fibril bundles.[50] As described in previous sections, there is a correlation between the orientation of the collagen fibrils and the minerals particles. This thesis discusses two main methods to study the ultrastructure of bone and tusk: X-ray diffraction and scattering and birefringence microscopy. These techniques rely on measuring different signals and indirectly reconstructing an image based on a certain contrast.[50]

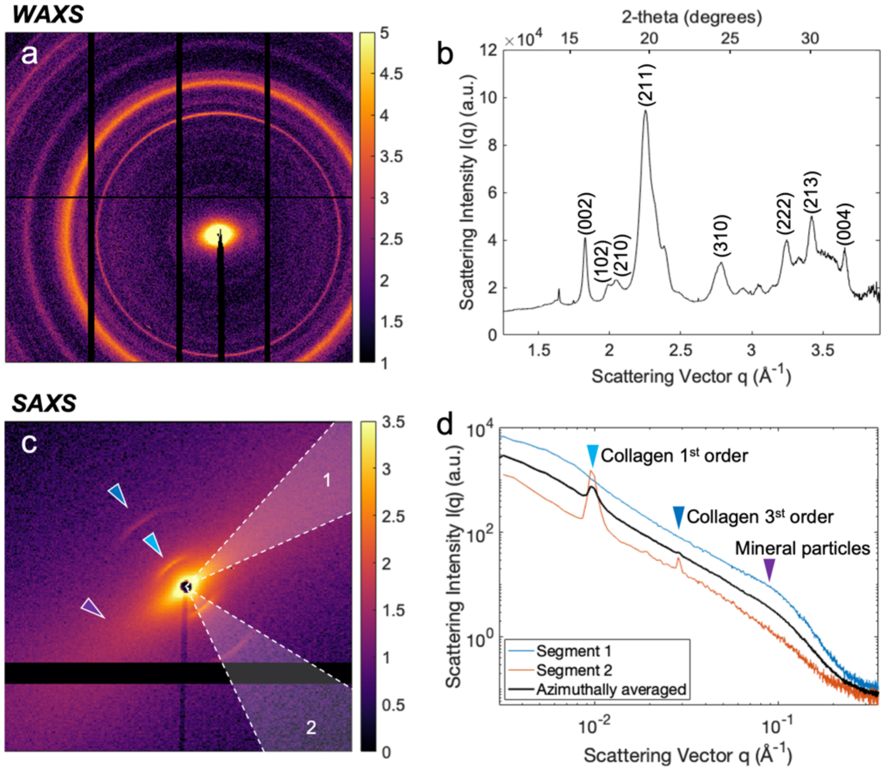

Figure 3.6. Representative diffraction (**a**) and scattering (**c**) patterns of narwhal tusk. The integrated signals show the diffraction of the hydroxyapatite mineral particles (**b**) and the scattering of two 90°-opposed segments, and their azimuthally integrated signal (**d**). Segment 1 shows the scattering contribution of the mineral particles and segment 2 the diffraction of the mineralised collagen fibrils.

X-rays can be used to study the arrangement of the mineralised collagen fibrils. Wide-angle X-ray scattering (WAXS) provides information about ordered structures below the nanometre level. WAXS can be used to study the crystalline structure of the mineral particles by obtaining the diffraction signal of the atomic crystalline planes in the hydroxyapatite nanoparticles (Figure 3.6a-b). In contrast, small-angle X-ray scattering (SAXS) probes the electron density contrast of larger structures between 1 – 100 nm. SAXS can study the orientation and morphology of collagen fibrils and mineral particles. It has been previously discussed that an anisotropic material results in an anisotropic scattering signal, a projection of the anisotropy of the 3D reciprocal space map (see Chapter 2). The scattering pattern of collagen is mainly given by the scattering contribution of the collagen fibril diameter and the diffraction of the axial periodicity of the collagen molecules along the fibrils. The diffraction signal is created by the periodicity in the electron density of the collagen molecules and the mineral particles in the gaps (or water in the case of tendons) with a spacing of ~67 nm, depending on the tissue (see Figure 3.2). That signal corresponds to the staggering period of the collagen fibrils along their axis (D-spacing), which anisotropy is along the collagen fibrils axis. In bone and tooth, only the first and third order are often visible (Figure 3.6c-d).[88, 89] The scattering from the mineral particles is the result of a group of particles in a matrix with different electron densities and reflects the size and shape distribution. In this case, the scattering signal of a flat particle would result in an elongated ellipsoid perpendicular to the particle. On the one hand, if these particles are assumed to be oriented in multiple directions along a common axis (e.g., as in the intrafibrillar particles in collagen fibrils), it creates an elongated ellipsoid oriented in various directions (e.g., disk-like signal). On the other hand, the scattering pattern of a needle-like particle is also a disk perpendicular to the needle axis. Therefore, platelet or needle-like particles with a certain degree of axial isotropy are virtually indistinguishable in most scattering experiments.[90] The anisotropy of the scattering signal of the mineral particles is perpendicular to the scattering signal of the mineralised collagen fibrils (Figure 3.6a-b) and the long-axis of the particle (i.e., c-axis of the crystal). The mineralised collagen fibrils and the c-axis of the mineral particles are parallel and share the same orientation.[91]

The mineral particle size varies between different stages in the maturity state of the individual, bone type and species.[92] Assuming anisotropic particles of any shape, the smallest dimension of the particle can be estimated using different models to describe the scattering signal. A first approximation is using a model independent of any specific particle shape and arrangement. The scattering signal of a particle in a two-phase system can be described as a constant (I_0), a form factor from the shape of the particles ($F(qT)$), a structure factor of particle-particle interaction ($S(q)$) and the average particle size (T) as in Equation 3.1.

$$I(q) = I_0 T^3 F(qT)(1 + S(q)) \qquad \text{Equation 3.1}$$

The size of a particle (T) can be obtained by the surface (S) to volume (V) ratio as in $T = 4V/S$. The scattering of a particle is followed by a Porod law contribution ($I(q) = P/q^4$) at high q-values, with Porod constant:[93, 94]

$$P = \frac{4}{\pi T}\int_0^\infty q^2 I(q)\, dq \qquad \text{Equation 3.2}$$

The particle thickness (T) has been shown to be related to the mineral volume fraction (ϕ) and the total surface area per volume (σ) as in Equation 3.3.

$$T = \frac{4\phi(1-\phi)}{\sigma} \qquad \text{Equation 3.3}$$

Therefore, T can be estimated assuming particles in a two-phase system with sharp interphases, assuming a volume fraction of 50% using the *T-parameter*, developed by Fratzl et al.,[93] by directly determining the Porod constant (P) and the invariant (J) using Equation 3.4.

$$T = \frac{4J}{\pi P} = \frac{4}{\pi}\frac{\int_0^\infty q^2 I(q) dq}{\lim\limits_{q\to\infty} q^4 I(q)} \qquad \text{Equation 3.4}$$

The invariant (J) is proportional to the volume of the particle per unit volume and can be determined by the Kratky plot as the integrated intensity of $q^2 I(q)$ vs q. The difficulties with this model come from the fact that the scattering function $I(q)$ is experimentally defined for a limited range, while J extends from 0 to infinity. The value of $q^2I(q)$ can be extrapolated at high q-values using Porod's law, however at low-q there is not a universal method to extrapolate it.[92] The determination of the invariant from the Kratky plot is only possible when the slope of the scattering signal at low-q is lower or equal to 2. A power law fitting in the Guinier region of the mineral platelet can be done in order to evaluate the slope as described in Liebi et al.[95] The scattering intensity $I(q)$ decays as a function of the amplitude, a, and the exponent, $-G$, as:

$$I(q) = aq^{-G} \qquad \text{Equation 3.5}$$

The T-parameter can be related to the distance distribution function of the particles ($I_P = 4\phi/\sigma$) and matrix ($I_M = 4(1-\phi)$) as $1/T = 1/I_P + 1/I_M$.

In the "stack of cards" model, an arrangement of plate-like particles in a parallel stack with uniaxial orientation in the direction of the collagen fibril matrix is assumed.[96] A rescaled function $G(x)$ ($x = qT$) containing the information about the shape and arrangement of the crystals was introduced, such as:

$$G(x) = \frac{x^2 I(x/T)}{JT^3} \qquad \text{Equation 3.6}$$

Where $G(x)$ must fulfil the condition:

$$\int_0^\infty G(x)dx = 1 \qquad \text{Equation 3.7}$$

The particle thickness (T) can be obtained using Equation 3.8, where $x = qT$. The rescaled function $G(x)$ can be calculated as shown in Equation 3.9, where the parameter α controls the damping of the oscillations (i.e., indicates the extent of the order) and β represents the degree of spatial correlation between particles.[97]

$$q^2 I(q) = \frac{\pi}{4} PT^2 G(x) \qquad \text{Equation 3.8}$$

$$G(x) = \frac{4}{\pi} \frac{x^2 + (\alpha - 1)(\alpha^2 + \beta^2)}{(x^2 + \alpha^2 - \beta^2)^2 + 4\alpha^2\beta^2} \qquad \text{Equation 3.9}$$

Even though some efforts have been done to correct the mineral volume fraction in the present model,[98] a drawback is the assumption of a specific particle shape, It relies on determining the Porod's constant from the high q-values, which have a significant statistical error associated. A different approach from Bunger et al.[99] considers the possible crystal size and distribution irregularities affecting the assumed volume fraction. This model describes the form factor $P(q)$ of platelet particles with infinite lateral dimensions as in Equation 3.10 and defines an average form factor $P_{av}(q)$, including the possible polydispersity of the system. All this is then included in an effective form factor $P_{eff}(q)$, which uses a random phase approximation (RPA) to adjust the mineral fraction in the system by a parameter that increases with increasing concentrations. It is based on the assumption that when crystals are large, they will be located closer to each other, modifying the electron density distribution.

$$P(q) = \frac{1}{q^2}\left|\frac{sin(qT/2)}{qT/2}\right|^2 \qquad \text{Equation 3.10}$$

In addition, a structure factor that contains the variations in electron density at smaller length scales from the inhomogeneities in size and arrangement of the crystals is introduced in the model. These variations are described as a fractal system with a scaling factor and a parameter describing the fractal dimension. The resulting intensity is, therefore, the contribution of the effective form factor $P_{eff}(q)$ and the fractal structure factor $S_{frac}(q)$ (Equation 3.11).

$$I(q) = P_{eff}(q)\, S_{frac}(q) \qquad \text{Equation 3.11}$$

Organised collagen is intrinsically birefringent, with an increase in the birefringence with its anisotropy. Apart from X-rays, polarised light interacts with the aligned collagen fibres in biological tissues. In circular polarised light the contrast in the image is given by the out-of-plane orientation of the mineralised collagen fibres, getting the highest intensities when perpendicular to the light beam, and also the in-plane orientation in the case of linearly polarised light.[100] The contrast is also affected by other factors such as the overall degree of order of the fibres in the probed area, sample thickness and optical transparency. These factors complicate the quantification of the 2D and 3D arrangement, making this technique difficult to use for quantitative estimations.[101] For this purpose, birefringence microscopy, introduced in Chapter 2, uses polarised light to retrieve the change in the polarisation angle and the phase difference or retardance, which adds valuable quantitative information about the degree of order.

3.6. Challenges in Bone and Tooth Regeneration

Bone loss as a consequence of disease, osteoporosis or trauma affects millions of people globally and is one of the leading causes of disability worldwide.[102] Bone fractures alone affect over 150 million bone fractures every year.[103] For these reasons, bone healing and regeneration is a problem of high medical and social relevance. The remodelling process in bone is a fundamental characteristic of this tissue that brings an extraordinary capacity for adaptation and self-repair. Cells in bone are responsive to changes in mechanical load and can adjust the balance between bone formation and resorption, changing its architecture according to the local stress applied. Tooth and tusk injuries are prevalent; however, these tissues have a very limited capacity for self-repair since they do not have the same remodelling capacities as bone. Enamel is decellularized, and defects cannot be repaired. Dentine has a very minimal regeneration capacity and depends on the action of the pulp stem cells. Cementum stands out from the other two tissues since it is vascularised and cellularised.

The remodelling activity of cementum in some regions in the root is very similar to bone, responding to mechanical load.[79, 104]

3.6.1. Phases of Bone Regeneration

The remodelling process is a spontaneous response to relatively low-intensity stimulus in the musculoskeletal system during relatively extended periods, from a few weeks to several months. In case of severe damage, the same principles of bone remodelling will contribute to creating new tissue; however, several other factors need to be considered. The different phases in the regeneration of bone fractures are the following:

Inflammatory phase: The process starts with the accumulation of blood cells in the fracture site to prevent further bleeding in the hematoma formation. After a few hours, the blood cells and fibrillar proteins form the hematoma, forming the callus template. The hematoma supplies the fracture site with growth factors, collagen and inflammatory molecules to initiate the regeneration.[105, 106] The inflammatory process is essential for the successful regeneration process. It is activated after the hematoma formation, and it serves two purposes. First, it triggers the pain signal forcing the individual to immobilise the affected part. Second, it attracts a large number of cells that activate the immune system and promote the generation of extracellular matrix and new tissue.[107]

Reparative phase: After the inflammatory phase, the fracture site forms granulation tissue, a loose aggregate of cells in the extracellular matrix. Neutrophils destroy necrotic tissue, and the waste material is digested by macrophages. Fibroblasts produce new collagen, and small new blood vessels are created. A soft callus is formed, extending throughout the fracture gap and connecting the bone endings. This process improves stability at the fracture site for the ossification process to start. A hard callus consisting of woven bone is then formed. Depending on the fracture type, the hard callus will replace the cartilage tissue previously formed, depositing minerals in the collagen matrix. With the formation of the hard callus, the bone recovers most of its original strength.[105, 107]

Remodelling phase: Remodelling is the final stage of the regeneration process and starts 3 – 4 weeks after the fracture and often lasts for 3 – 5 years. It represents a gradual and continuous modification of the architecture of bone that eventually establishes the native osteon structure. During this stage, the bone in the hard callus is reabsorbed and regenerated to accommodate the new structure to the actual needs of load and functionality.[105, 107]

3.6.2. Critical-Size Bone Defects

When a patient loses a significant amount of bone, the regenerative ability of the tissue is very limited. As the gap in the bone increases, the possibility of spontaneous healing is significantly reduced, leading to non-union. That is a particular case in bone regeneration called critical-size defect, which presents a great challenge for researchers and clinicians. The large size of the defect (~3 – 4 cm in humans) disrupts the normal healing process, interfering with osteogenesis (i.e., formation of new bone) and angiogenesis (i.e., formation of new blood vessels).[108] The current standard methods to treat critical-size defects include mechanical stabilization to prevent motion and autogenous bone grafting. However, these methods require several surgical procedures to collect enough tissue from several anatomical locations in the patient, associated with high rates of infection, severe pain, and long recovery periods extending from months to years.[109] Finding new methods to promote bone regeneration in critical-size defects is highly needed, which is discussed in Section 6.2.1 and ***Paper III***.

Chapter 4

Synthetic Hierarchical Materials

In the last decades, the interest in materials with controlled structures in the nanoscale has increased enormously due to the development of new production and characterisation methods that brought a whole new world to science.[110, 111] The significant impact of these methods comes from the interest on manipulating atom-by-atom (equivalent to molecule-by-molecule) to create new structures at the nanoscale.[112] New devices were possible with improved performances and functionalities than the ones fabricated by the standard manufacturing technologies. Some examples of nanomaterials applied to different fields are gas and biosensors using the high specific surface and plasmonic properties of nanoparticles.[113] The field of electronics, optoelectronics and photovoltaics greatly benefitted from nanomaterials such as thin films, nanoparticles, nanotubes and nanowires.[114] In biomedicine, numerous improvements have been made thanks to the access and development of nanomaterials compatible with the organism that reduce the drug usage, smartly target cancer cells or allow us to track and treat complex diseases.[115, 116]

4.1. Bioinspired Hierarchical Materials

Nature can be a source of inspiration for modern advanced materials, where we can find systems with properties and mechanisms to solve daily problems that go beyond the current knowledge of technology. The study of the biological materials found in nature has the potential to lead the path to innovative solutions to modern society's problems.

Biological materials found in nature share several features that researchers should keep in mind while designing new bioinspired materials. Excluding a few exceptions, biological materials are formed at room temperature, ambient pressure and in aqueous media. They are formed from a very limited source of elements surrounding them, which defines their composition, morphology, and final properties. Natural materials often profit from self-assembly to build larger ordered structures from those simple components, assembled in a *bottom-up* process rather than the more usual *top-down* synthesis we are used to. The arrangement of the different self-assembled blocks brings different physical and chemical properties to the next level of hierarchy. Considerable efforts are being made to study each of these levels in detail, understanding their individual properties and collective functionality in the material. Biological structures tend to have a multi-functional purpose. As in bird feathers or mammal fur, they provide insulation, camouflage, social communication and protection from the environment. The key to their excellent performance but simple composition is their hierarchical structure.[117]

The process of designing bioinspired materials starts with studying the design of new or unknown natural structures with superior functionality that we aim to imitate or trigger our curiosity based on their properties or structure. It starts with discovering a unique and interesting material and using scientific analysis to unravel the fundamental mechanism/structure behind it. This new knowledge sets the basis of the relationship between composition, structure and properties that can be later used to address a specific engineering problem. In the development step, the new principles learnt from nature are applied to the design and production of synthetic materials with the desired properties and improved performance. The new fabrication routes define the challenges in this field to be able to synthesise such intricate structures as well as be able to transfer highly sophisticated laboratory equipment to industrial production.[118]

An excellent example of applying the scientific method to learn from nature at the same time that we find solutions to complex problems is the development of biomaterials inspired in, and for our own body. As described in Chapter 3, bones are one of the largest organs in our body. They offer structural support, mobility and protection to vital organs. In bone, collagen molecules form long fibres assembled in bundles with intercalated ceramic hydroxyapatite nanoplatelets. Several bundles of fibres oriented in the same direction create collagen fibrils packed in geometrical structures with a very defined orientation, such as lamellae and osteons. Those structures create the cortical (compact) and trabecular (spongy) bone, creating a polymer-ceramic composite with high anisotropy that forms the skeleton of vertebrates.[1] Despite their inherent ability to continuously regenerate themselves, bones are exposed to many pathological conditions such as trauma, cancer, osteoporosis, etc.

In the quest to find better solutions for bone healing and regeneration, biocompatibility and bioactivity are the keys. The old trend of designing biomaterials with a purely structural function is being replaced by new strategies that prime bioinspiration and integration with the body. Implants that aim to be unnoticed by the body are changing to materials able to interact and develop with the body's environment, interacting with the cells and surrounding elements. To achieve this goal, we need to put effort into understanding the complexity of the tissue, its environment and the role it plays in the body.

Many strategies have been developed to mimic the hierarchical structure of bone to repair bone defects. Bone graft substitutes are a great option made of synthetic material which will fill the gap in the defect; at the same time, they could provide mechanical support, promote cell migration or deliver controlled amounts of chemicals to prevent infection or boost the healing process.[119]

One example of bio-inspired bone graft is biocompatible polymeric fibres such as PLGA (poly(DL-lactic–glycolic acid) with amorphous calcium phosphate particles, which can replicate the cellular environment while promoting osseointegration and cell migration (Figure 4.1a).[120] While electrospun fibres create a highly porous scaffold that facilitates cell adhesion, proliferation and vascularisation,[121, 122] calcium phosphate particles improve their mechanical properties and enhance their osteoconductivity and bioactivity.[123, 124] These scaffolds also can mimic and promote the generation of extracellular matrix (ECM). Anisotropic scaffolds with fibres aligned in a defined direction have the potential to produce an anisotropic extracellular matrix as in the native bone. The extracellular matrix comprises fibrous collagen, proteoglycans, growth factor and hydroxyapatite, among others.[125] Due to its complexity, it is challenging to mimic; therefore, promoting its growth is a better option to create the appropriate environment for cells to develop and create new bone tissue. ***Paper III*** tested this approach *in vitro* and *in vivo* to study the growth process and bone quality of such bioinspired materials using scattering imaging techniques (Figure 4.1b).

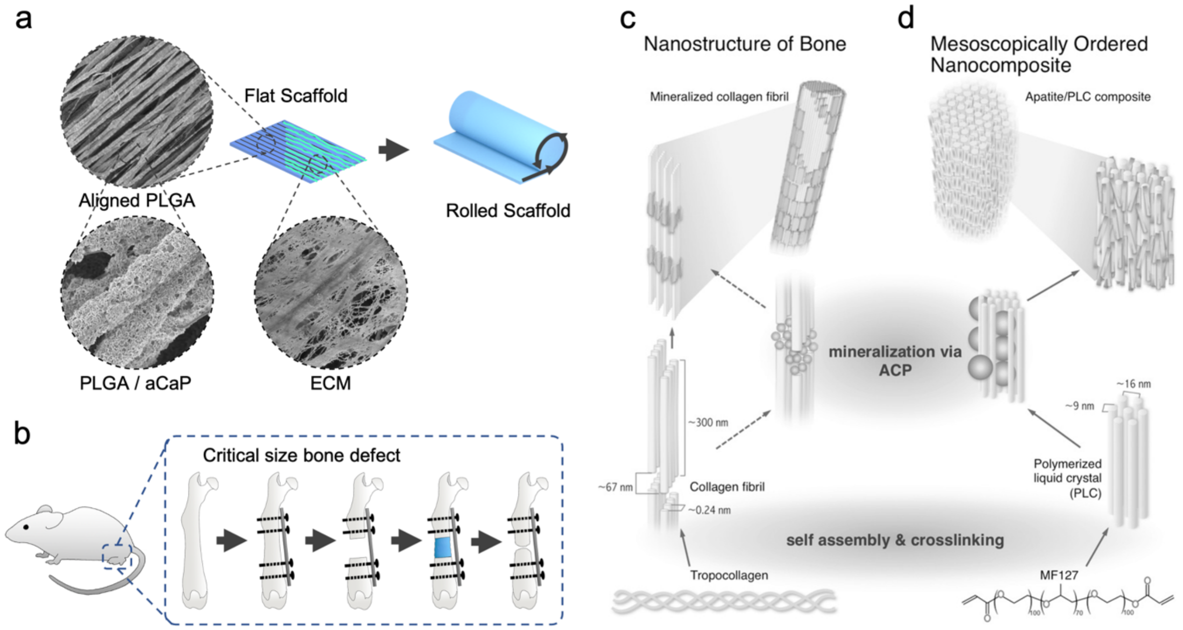

Figure 4.1. Examples of bio-inspired material for bone grafts. **a**) Electrospun aligned PLGA fibres mineralised with amorphous calcium phosphate nanoparticles (aCaP) and rolled to create bio-inspired scaffolds for critical-size bone defects. These scaffolds promote the growth of extracellular matrix (ECM), mimicking the natural cell environment of the bone and promoting the regeneration process *in vivo* (**b**). On the other hand, mineralised lyotropic liquid crystals, bio-inspired in the nano and microstructure of bone (**c**, **d**), can be used for implants with anisotropic mechanical properties. Adapted with permission from Wen-Xiao et al.[4] (Copyright 2015, John Wiley and Sons).

Another example of bioinspired composite materials for bone grafts that uses the principles of self-assembly discussed before is lyotropic liquid crystals mineralised with calcium phosphate particles. Inspired by the natural growth of bone tissue and the mineralisation process of collagen fibres,[126] templating can be used to produce composites with anisotropic structures (Figure 4.1c-d). In order to mimic the mechanical properties of bone, self-assembly can be used to create the polymeric matrix before the mineralisation step, which can define the structural anisotropy at the nanoscale. Aligned liquid crystals of block co-polymers via, e.g., extrusion or 3D printing, can be used for this purpose, in which hexagonally packed cylinders act as collagen fibres. Bilayers can be used in a lamellar stack as in the lamellar compact bone. These anisotropic structures create a confined space that is used as a template for a further mineralisation step. Calcium phosphate solutions are often infiltrated in a matrix, where amorphous ceramic particles are forced to precipitate in the gaps. When aged, amorphous calcium phosphate transforms into crystalline hydroxyapatite, the most common ceramic component in bone. When mineralised, the ceramic particles also have a high anisotropy, which confers their different mechanical properties in different load directions.[4] ***Papers I and II*** study the production process of these composite materials and the fundamental mechanisms that lead to the alignment of the polymeric matrix, described in the following sections.

4.2. Self-Assembly at the Nanoscale

There are two general routes for the formation of materials with controlled nanostructure known as *top-down* and *bottom-up*. The *top-down* strategy has been used mainly in physics and engineering and consists of reducing the dimensions of a macroscopic material via mechanical, chemical or optical processes. The efficiency of this method is considerably low, and the maximum resolution is limited by the techniques (usually around 100 nm). In contrast to this approach, basic units such as atoms or molecules are hierarchically assembled in larger structures via chemical or physical processes in the *bottom-up* route. The size of the materials created is in the range of nanometres; however, the production of those materials is driven by chemical and/or physical forces, which are sometimes hard to control and predict. A combination of both approaches is also often used, where *top-down* and *bottom-up* routes achieve the best results for a specific application.[127]

Specific macromolecules such as block copolymers are used as molecular units in the *bottom-up* synthesis of nanomaterials. These polymers offer a well-controlled structure and composition of repeated organic molecules that form the different blocks, which are covalently linked together in long polymer chains. They are composed of two or more segments with different chemical compositions and often contain hydrophilic and hydrophobic blocks, which give them an amphiphilic behaviour. The interests of these block copolymers lie in their ability to self-assemble in organised structures. Self-assembly is a process where individual components organise into larger ordered structures by the action of local interactions without any external forces. The building blocks in self-assembled structures can vary from molecules to macromolecules, particles and aggregates. As described in the previous section, self-assembly is a common feature in biology, where biomolecules and phospholipids organise, forming the cell membranes that compose every living entity.[128] The driving force for the self-assembly of amphiphilic macromolecules is the minimisation of the free energy, dominated by weak Van der Waals forces, hydrogen bonds and electrostatic interaction. That translates into the interaction between the hydrophilicity/hydrophobicity of each block in a given environment.[129] In a polar solvent, the hydrophobic block tends to stay away from the solvent, resulting in the association of several copolymer chains together so that the hydrophilic block(s) face the polar domain and the hydrophobic block(s) form the apolar domain (see Figure 4.2) in what is called the micellisation process in solutions or the microphase segregation in concentrated systems.[130, 131] This process reduces the total free energy of the system when the hydrophobic chains dissociate themselves from the polar environment. In the case of the systems described within this thesis, an association of polymeric chains need to occur and ordered clusters of polymer chains form different geometries defined by the total polymer concentration in the system.[132] This process can be enhanced by adding an apolar solvent to the mixture. The presence of an apolar solvent in a polar environment facilitates the creation of polar/apolar domains and the assembly of polymer chains in their interphase.

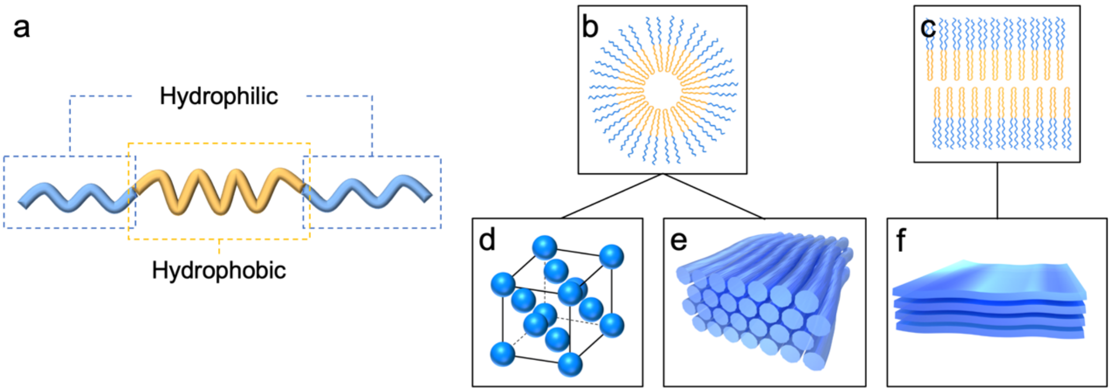

Figure 4.2. Formation of self-assembled structures in block copolymer systems. The amphiphilic block copolymer (**a**) is assembled in spheres (**d**), cylinders (**e**) or bilayers (**c**, **f**) which can get an extended range of order on the microscale.

Depending on the chemical composition and amphiphilic structure, various arrangements can be achieved. Dominated by the packing parameter, the final shape of the self-assembled structure is defined by the volume and contact area of the polar and apolar chains of the polymer in the different conformations of the hydrocarbon chain. Spheres, cylinders, worm-like micelles (cylinders with micrometre length), vesicles and bilayers are some of the possible structures, among many others.[133, 134] The basic parameters which control the assembly of these structures in the case of block copolymers are defined by the block composition (i.e. ratio of hydrophilic/hydrophobic blocks and their length), concentration, temperature, solvent, pH, etc. The action radius of self-assembly does not end at the molecular scale, and such systems can re-arrange at the nanoscale forming complex superlattices under certain conditions.[135, 136]

4.3. Liquid Crystals

Unlike other crystalline materials, which are associated with a solid and stiff behaviour, liquid-crystalline materials have a liquid-like fluidity and an anisotropic arrangement of their molecular components. They can be described as materials with a degree of order between the complete disorder of a liquid and the three-dimensional long-range order of a crystal.[128] They have an orientational order and may also have a positional order.[137] This order distinguishes them from regular liquids from a structural point of view and their anisotropic physical properties. Molecular anisotropy is the key to liquid crystals, usually formed by stiff molecules with a high aspect ratio, either length-to-diameter (needle-like) or diameter-to-thickness (discs). The existence of a liquid-crystalline state is often guided by the interaction between molecules and the volume constraints imposed by a highly concentrated and densely packed system.

An illustrative example is thermotropic liquid crystals, which transit between the ordered and disordered states by changes in their temperature. When the temperature of the system is reduced, molecules do not have enough available energy to overcome the intramolecular rotational-energy barrier, and they adopt more extended conformations. That leads to an increase in the volume of the molecule and, therefore, in the molecular interaction energy that is minimized by acquiring a more densely packed fraction and increased long-range order. On the other hand, in so-called lyotropic liquid crystals, a transition to an ordered state can also be produced by a change in concentration. Whereas thermotropic liquid crystals do not need a solvent to form liquid crystal phases, lyotropic liquid crystals are always formed by amphiphiles in solution. Their crystalline structure is defined by the concentration of polymer, i.e. by increasing the concentration of molecular units, the available free space is reduced, and a liquid-crystalline order is favoured.[137]

The liquid crystalline state is generally discussed with simple molecules; however, the production of those materials is not only limited to molecules but some other larger structures have been proven to form liquid crystals. Rod-like inorganic particles have been observed forming liquid crystalline phases[138] and long peptide molecules assembled in fibres forming lyotropic liquid crystals.[139] Block copolymers in water or a solvent mixture represent one category which forms lyotropic liquid crystals. The phase diagrams of the lyotropic liquid crystals used within this thesis are introduced in Section 5.2. Block copolymers, self-assembled in micelles, cylinders, bilayers, etc., become suitable building blocks to create liquid crystals. The interaction and assembly of these larger structures create a new level of hierarchy on a larger length scale. A hierarchical structure with two different types of long-range order is thus formed: the molecular and the aggregate scale.[140] The nanostructures created by self-assembled processes can be used in the bottom-up approach as an ordering mechanism at the lower length scales. In order to create hierarchical systems, the control over the macro and microstructure is crucial as well, and it is elaborated on in the following two sections.

4.4. Inducing Anisotropy

The anisotropy in the nanoscale can be extended to the micro and macro scale using different processing methods such as additive manufacturing. Commonly known as 3D printing, additive manufacturing is a production method in which objects are manufactured from a CAD (Computer-Aided Design) model layer-by-layer. Slicing the total volume of the object in thin layers allows to produce geometries with high complexity avoiding moulds, dies and generating much less or no excess waste material. This method has raised a high academic and industrial interest in the recent years, which led to the development of multiple technologies for every type of material and environments.[141]

Electrospinning is an additive manufacturing method to produce micro and nanofibers in a continuous process. In this process, a polymeric solution is ejected from a micrometric nozzle to which an electric potential is applied. The electric field overcomes the surface tension of the fluid droplets, ejecting them in the form of fibres to a collecting plate or wheel, which grounds the electrical charge. The fibres form a mesh or mat on the surface of the collecting plate with a specific orientation and morphology.[142] The diameter and morphology of the printed fibres can also be easily controlled by the type of material in the solution and its concentration, processing parameters and ambient factors such as temperature and humidity level.[143] This method is especially interesting for extruding polymers with multiple compositions, such as block copolymers. It also allows extruding polymers loaded with nanoparticles such as the previously described calcium phosphates and different molecules such as drugs or cell growth factors.[105] The degree of anisotropy or randomness of the final fibre mat highly depends on the collection device, whether it is a fixed plate, a mobile platform or a spinning wheel. Highly anisotropic mats are usually obtained using a rotating collector where the fibres are aligned and stretched as it rotates, or electrostatic/magnetic alignment in which an external field is used to manipulate the ejected fibres during the deposition.[144] This deposition method reaches a macroscopic alignment and can produce fibres with a highly anisotropic molecular structure in which the polymer chain stretches and aligns in the fibre direction.[145] This method was used to produce the scaffolds in ***Paper III***, which usability as template for bone regeneration was investigated.

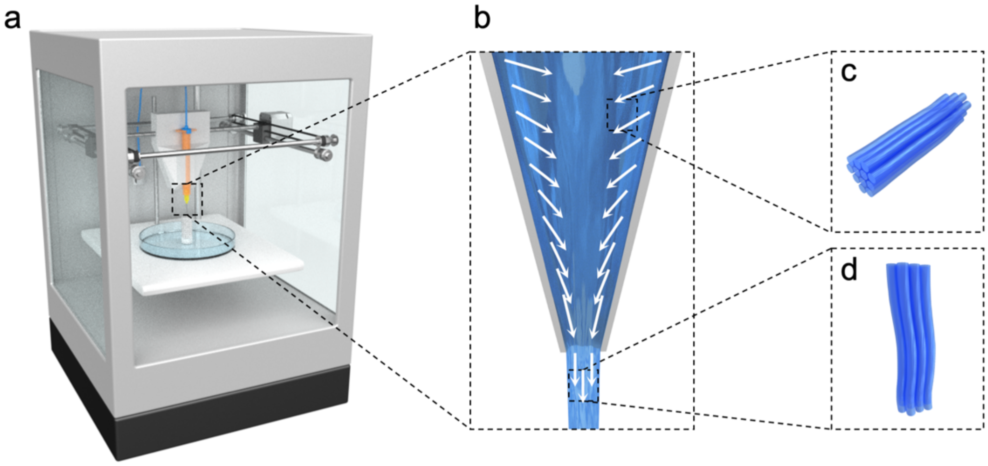

Figure 4.3. 3D printing can be used to induce macroscopy anisotropy in hierarchical materials. The fluid in a cartridge is 3D printed by extrusion (**a**), which aligns the entitles that form the liquid crystals. The flow in the 3D printing nozzle (**b**) induce alignment by extensional and shear flows. The white arrows indicate the most common/probable directions of flow, where the nano entities of the liquid crystal are expected to be found oriented (**c**-**d**).

Extrusion-based 3D printing is another additive manufacturing technique with a high interest in the field of anisotropic materials. The printing material (i.e. the ink) in a fluid-like state is loaded in a cartridge and extruded through a nozzle, producing a continuous filament. A mobile platform in the horizontal plane (xy-plane) produces the layered geometry, and a stage on the z-axis allows to move between layers. The interest in this method lies in the effect that extrusion has on the ink, aligning the particles or molecules and creating a certain degree of anisotropy depending on the processing parameters, as explained in Figure 4.3. Anisotropic filaments are highly interesting in science and technology, for example, for producing 3D printed optically responsive devices[146] or creating composites with complex hierarchical structures.[147] The nozzle is designed with a constriction towards the outlet that reduces the inner space, increasing the velocity of the fluid at that point. The generated extensional flow in the central part creates a stretching strain in the ink, which may eventually align the anisotropic molecules, polymeric chains or particles in the flow direction. The small dimensions of the nozzle also generate high shear rates in the proximities of the walls, which also contribute to the alignment process. During shear, fluids with anisotropic components tend to align in the shear plane, reducing the interparticle interaction, reducing the viscosity and facilitating the flow in what is known as shear thinning. An ideal material suitable for 3D printing should have a combination of shear thinning behaviour that facilitates the printing process, but sufficient viscosity and yield strength to self-stand and hold the shape after the extrusion. The variability in the nanostructure and rheology of the different printing materials brings about the importance of evaluating the behaviour and effect of extensional and shear forces in each system.

There are multiple methods to analyse the anisotropy in the nanoscale, where several fields use different calculations adapted to the different measuring techniques. High-resolution microscopy techniques (e.g. scanning and/or transmission electron microscopy, etc.) can visualise the structures directly. They rely on image analysis algorithms which identify shape, size and other contrast parameters; however, they only reach a small field of view and achieving a complete overview is sometimes difficult. Methods to indirectly probe the alignment of the material include techniques such as scattering or birefringence (see Chapter 2 and Chapter 5 for more details). They use the interactions of photons with matter to probe the nanostructure of materials, which leads to an anisotropic scattering, diffraction of refraction.[50]

Several approaches have been developed to estimate or quantify the degree of mutual alignment of nanoelements, or in more general words, how much (or how less) randomness is in the observed material, developed in the context of scattering and birefringence in Section 2.3.1 and Section 2.4. Taking an ensemble of fibres as a model, one extreme case would be when all of them are distributed perfectly isotropic, and the average orientation is therefore 0. No preferential direction is observed. The other extreme case would be when the fibres are perfectly aligned in a given direction, the averaged orientation of the system is in the direction of any of the fibres, and the standard deviation is 0. In this frame, any possibility between both extremes will contain a certain amount of order and a certain amount of disorder/randomness, which is attempted to be quantified by the orientational order parameter. The orientational order parameter S_N (Equation 4.1) describes the distribution of orientations of the anisotropic axis of molecules, particles or fibres, where a perfectly aligned system will result in a value of 1, a perfect disorder system in a value of 0, and -0.5 in case of perpendicular alignment.

$$\mathrm{S_N} = \frac{3\langle\cos^2\theta\rangle - 1}{2} \qquad \text{Equation 4.1}$$

The orientational distribution function $P(\theta, \phi)$ in spherical coordinates, with the polar (θ) and azimuthal (ϕ) angles, relates with the orientational parameter through Equation 4.2.[137] This method is extendedly used in the Hermans' Orientation Parameter in scattering (described in Section 2.3.1) or in birefringence experiments, applied to materials with a high degree of anisotropy.

$$\langle\cos^2\theta\rangle = \frac{\int_0^{\pi}\int_0^{2\pi} \cos^2\theta \, P(\theta, \phi) \sin\theta \, d\phi \, d\theta}{\int_0^{\pi}\int_0^{2\pi} P(\theta, \phi) \sin\theta \, d\phi \, d\theta} \qquad \text{Equation 4.2}$$

Chapter 5

Materials and Methods

The following chapter describes the procedures during the sample preparation and the characterization techniques used to perform all the experiments that led to the results presented in Chapter 6. The basic theory behind the methods and the essential equations used for the data analysis are explained in Chapter 2. Details about the specific samples, experimental parameters and other methods not relevant for the purpose of this thesis can be found in the methods section of the appended papers at the end.

5.1. Biological Samples

5.1.1. Animal Models and *In Vivo* Experiments

Twenty 10-week-old, pathogen-free, immunocompromised NOD.CB17-prkdscid mice (Charles River) were used for the work presented in this ***Paper III***. The animal housing and the study protocol were approved by the Cantonal Veterinary Office, Zurich (ZH 094/2019) and were in accordance with the Swiss Animal Protection Law and the European Directive 2010/63/EU of the European Parliament and the Council on the Protection of Animals used for Scientific Purposes. Animals were randomly assigned to four treatment groups (5 mice per group):

- Random scaffold seeded with cells.
- Random scaffold with extracellular matrix (after decellularization).
- Aligned scaffold seeded with cells.
- Aligned scaffold with extracellular matrix (after decellularization).

The entire surgery was done under strict aseptic conditions by the Department of Trauma Surgery at University Hospital Zurich (Switzerland). In brief (Figure 5.1a), an osteotomy (critical size bone defect) in the femur was performed by exposing the anterior surface of the right femur and fixing a 6-hole Internal Fixator Plate (RISystem, Internal Fixator Plate AO-MouseFix) with locking screws (RISystem AG, Davos, Switzerland). The 3.5 mm bone defect was subsequently filled with an equally sized piece of a scaffold according to the specific treatment groups. After scaffold insertion, 5-0 non-absorbable Dermalone sutures were used to close the skin. Seven weeks after the surgery, all mice were sacrificed, and the femurs were collected for further analysis.

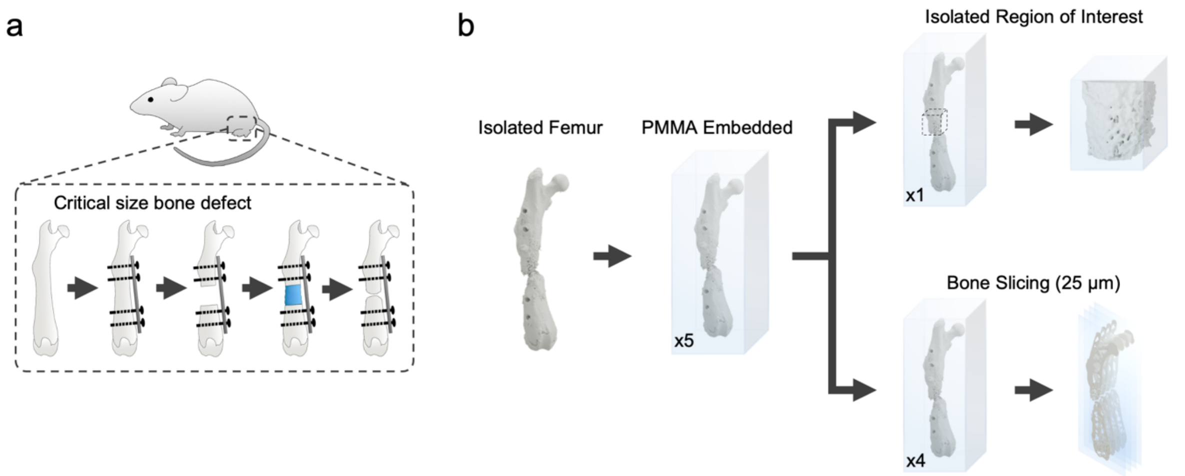

Figure 5.1. a) Surgical procedure of the *in vivo* experiments. The femurs were fixed with a metallic plate and an osteotomy was performed. The gap was filled with the different scaffolds and let heal for 7 weeks. **b**) The isolated bones were embedded in PMMA and prepared for the X-ray experiments in thin slices (x4 per group) and as subvolume of the bone (x1 per group).

The integration capabilities of 3D printed titanium (Ti6Al4V) implants,[148] presented in Section 6.2.2, were tested *in vivo* in a trabecular model in sheep distal femurs with a healing time of 6 months. The animal study was conducted according to FDA Good Laboratory Practice (GLP) regulations, using skeletally mature sheep. In brief, the implantation sites were exposed by a cutaneous incision followed by blunt dissection of the underlying tissues. The periosteum was carefully removed from the bone surface. An orthopaedic drill was used to create the implant holes. Sequential enlarging of the drill holes was done with 2, 4.3, and 5mm diameter drills under constant irrigation with saline solution (NaCl 0.9%). The implants were then installed by press fitting. The incision was closed in layers where both capsule and muscles were sutured with absorbable thread, and the skin layer was closed using surgical staples. The operated legs were not restrained in any manner after the surgery procedure. After 6 months, the sheep were euthanised by an intravenous overdose of pentobarbital.[148, 149]

5.1.2. Bone Fixation and Embedding

The bones used for the *in vivo* experiments (***Paper III***) were embedded in poly(methyl methacrylate) (PMMA) for later use in the X-ray experiments (Figure 5.1b). After the surgical procedure and recovery period, all isolated bones were dehydrated using a sequential water substitution process in ethanol in increasing concentrations (40%/24 h, 70%/72 h, 96%/72 h and 100%/72 h) and fixed in formalin. The ethanol solutions were replaced every 24h. The pre-infiltration procedure for embedding was performed using methyl methacrylate (MMA, Sigma Aldrich) for one week at 4°C. The samples were then embedded in MMA containing 0.5% Perkadox 16S (Dr Grogg Chemie AG), 15% dibuthylpthalate (Sigma Aldrich), and 0.01% Pentaerythrit-tetrakis-(3,5-di-tert-butyl-4-hydroxyhydrocinnamat) (Sigma Aldrich) for 48 h at 4°C. The polymerisation was then continued for 24 h at 27°C. The temperature was increased to 37°C for 24 – 48 h in cases when the polymerisation did not occur. Four embedded samples from each treatment group were cut using a Mecatome T180 to 25 μm sections. All 25 μm sections were fixed on a Kapton tape for the scanning SAXS experiment. One specimen from each experimental group was chosen for the SAXS tensor tomography experiments. In that case, the PMMA-embedded bone was cut at the extremities to isolate the region of interest around the scaffold and shaped into a cylinder using a metal file.

The implants used in the *in vivo* experiments in Section 6.2.2 were harvested with the surrounding tissue, fixed in 10% neutral buffered formalin and dehydrated in a series of ethanol of increasing concentration. The specimens were embedded in plastic resin (LR White, London Resin Co. Ltd, UK) following a standard infiltration and polymerisation procedure. The embedded implant/bone blocks were bisected by sawing and grinding, and one half-block of each specimen was used to prepare a central ground section (15–20 μm thick), which was stained with toluidine blue.[148, 149]

5.1.3. Narwhal samples

Two narwhal specimens were collected from Greenland. The narwhal skulls with tusks originates from the Inuit subsistence hunt and were purchased as part of scientific research granted by the Danish Environmental Protection Agency. The specimens were exported under the CITES (Convention on International Trade in Endangered Species of Wild Fauna and Flora) export permit and imported to Denmark with a CITES import permit. Small slices and cylinders where then imported to Switzerland for measurements (CITES permission number 22EB001588-AS).

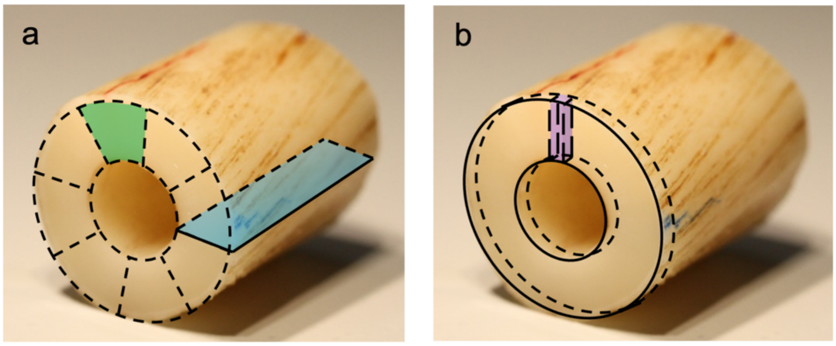

Figure 5.2. Narwhal tusk section. Sample preparation for the 2D scanning SAXS and XRF experiments (**a**), and 3D SAXS tensor tomography (**b**).

The skulls were sawn transversally in segments of approximately 14 cm long (Figure 5.2). Longitudinal and transverse sections of the tusks ~1 mm in thickness were then prepared (Figure 5.2a) using a diamond saw (Struers Accutom-5, Denmark). The slices were grinded down to 30 – 50 μm for the X-ray and birefringence experiments using SiC abrasive paper. Prismatic blocks of 1.0×1.0×2.5 mm for SAXS tensor tomography were prepared from the same sections (Figure 5.2b) and then shaped into cylinders using a metallic file. The samples for high-resolution SAXS tensor tomography were prepared as cylinders of 300 μm in diameter and length using a home-built lathe system inspired by the one developed by Holler at al.[150]

5.2. Self-Assembled Lyotropic Liquid Crystals

The lyotropic liquid crystals used in ***Paper I*** and ***II*** were prepared by dissolving the block copolymer in water or a mixture of water and a water-immiscible solvent. In the appropriate ratio, the minority solvent creates micro or nano droplets where the polymer is located at the interface. The hydrophilic block is dissolved in the polar liquid. In contrast, the hydrophobic block locates in the apolar solvent creating the different self-assembled structures guided by the interfaces of the two liquid phases. In the absence of apolar solvent, micro segregation takes place. The hydrophilic block is dissolved in water while the hydrophobic parts interact to form isolated apolar domains. In both cases, vigorous mixing is necessary to facilitate the creation of the polar/apolar interface and to homogenise the mixture since the concentration of polymer and solvent will define the self-assembled structure.

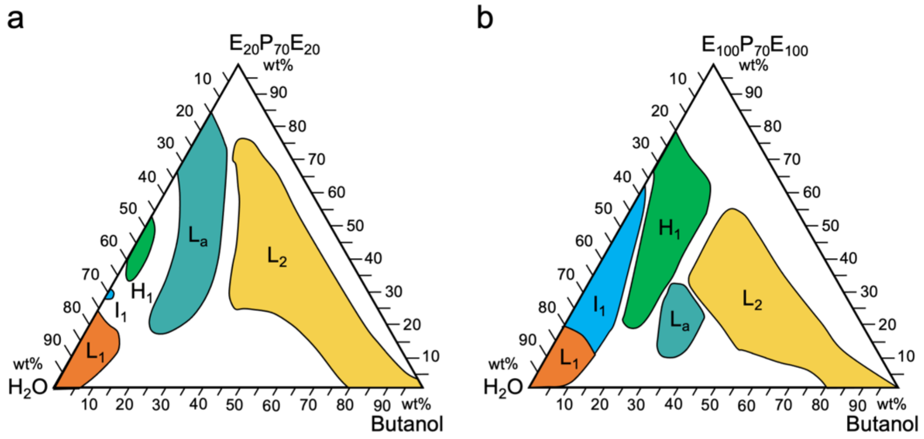

Figure 5.3. Phase diagrams of the ternary system Pluronic®-Water-Butanol for the polymers F-127 ($E_{100}P_{70}E_{100}$) (**a**) and P-123 ($E_{20}P_{70}E_{20}$) (**b**). Adapted with permission from P. Holmqvist et al.[151] (Copyright 1998, American Chemical Society).

The materials used in this thesis are based on the ternary system copolymer, water and 1-butanol, extensively described by Lindman et al. as shown in Figure 5.3.[151-155] The polymer of choice is a non-ionic amphiphilic tri-block copolymer formed by poly(ethylene oxide) (PEO) and poly(propylene oxide) (PPO) chains. Under the commercial name Pluronic®, several combinations of chain length and molecular architectures are available, F-127 ($PEO_{100}PPO_{70}PEO_{100}$) and P-123 ($PEO_{20}PPO_{70}PEO_{20}$) were the choices for this work. From the available range of self-assembled structures, we focused on two types that present anisotropy in their structures: the hexagonal and the lamellar phase (compositions detailed in Table 5.1). The mixture was centrifuged to remove the air bubbles introduced during the mixing stage and stored at 4 °C overnight before further use.

Table 5.1. Compositions of the prepared self-assembled lyotropic liquid crystals in percentage by mass. The labels in the sample name refer to the self-assembled structure, being H_1 for Hexagonal and L_α for Lamellar.

Sample	Structure	F-127	P-123	H_2O	Butanol
FH_1	Hexagonal	35.0	-	50.0	15.0
FL_α	Lamellar	25.0	-	47.5	27.5
PH_1	Hexagonal	-	45.0	55.0	-
PL_α	Lamellar	-	75.0	25.0	-

5.3. Synchrotron-Compatible Microfluidics

Microfluidics is a well-known tool for studying chemical reactions, physical processes and reproducing biological conditions. The main advantage of microfluidic channels is the low sample volume, homogeneity in flow, and adaptability to a wide range of geometries. Typically, one or several channels with sizes in the micrometre range are produced in a bulk material through which a fluid flows under controlled conditions. The confinement in the microscale produces a low Reynold's number where the viscous forces ensure a laminar flow with a smooth constant motion of the fluid. These conditions make it possible to study and predict some structure-related features in soft materials during flow, such as phase transitions, ordering or segregation.

Microfluidic channels with low thickness, which offer confinement in two dimensions, are frequently used together with microscopy and spectroscopy techniques to visualize the dynamics of fluids and suspensions in flow. Scattering techniques, especially X-rays, allow access to the nanostructural information, and the radiation damage is minimized by the continuous flow in the channel, which avoids long exposure to high-intensity radiation. However, the interaction of the scattering signal with the channel is often problematic, absorbing a considerable part of the scattered radiation or adding a significant contribution to the background level. A suitable approach to produce microfluidics compatible with synchrotron radiation was adapted from Lutz-Bueno et al.[156] in which a sandwich structure with glass and a layer of poly(imide) offers high transmission and low background.

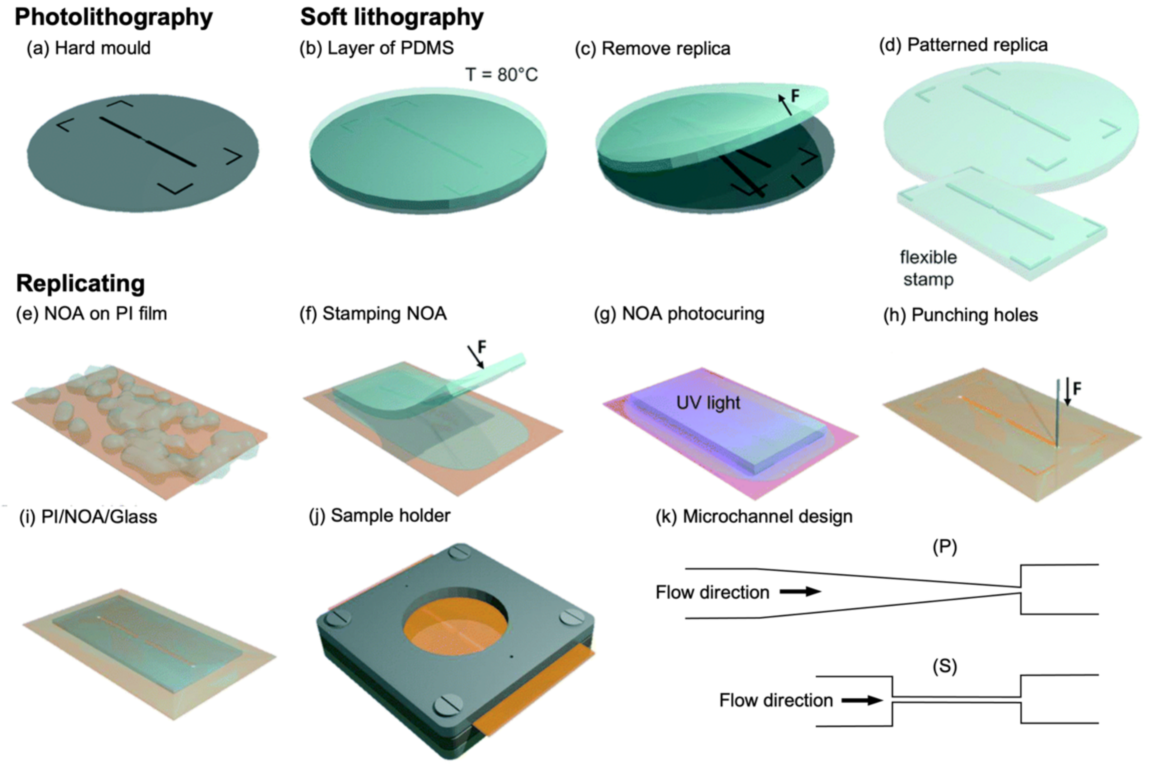

Figure 5.4. Fabrication process of the microfluidic channels compatible with synchrotron radiation (**a**-**i**). The lithographed silicon master (**a**) is used to obtention the flexible PMMA stamp (**d**). The channel design is stamped on the NOA layer (**f**) which is later photocured using UV light (**g**). The channels are mounted in an aluminium holder (**j**) containing all the necessary connections. The selected designs (**k**) have a progressive (P) and sharp (S) contraction from 1.25 mm to a microchannel of 100 μm. Adapted with permission from Lutz-Bueno et al.[156] (Copyright 2016, Royal Society of Chemistry).

As shown in Figure 5.4, the process starts with the channel design transferred from a silicon hard-mould to a flexible stamp. The silicon master was fabricated by photolithography on a 4 inches silicon wafer to obtain the negative patterns. The silicon master was used to produce several flexible stamps with positive features by soft lithography of poly(dimethyl siloxane) (PDMS). For this purpose, PDMS and crosslinker were mixed in the appropriate ratio and poured on the silicon hard-mould, followed by a degasification step with a rotatory pump to remove all the trapped air. The mixture was placed in an oven and baked at 70 °C for 60 min for the curing process.

After obtaining the PDMS stamps, the following fabrication process was entirely performed in clean room conditions to prevent dust or other microparticles from blocking the channel. A polyimide (PI) film (25 μm thickness) (Goodfellow Corp., Cambridge, UK) was carefully cleaned with isopropanol, and a droplet of UV curable resin (Norland Optical Adhesive, NOA#81) was poured on it. The PDMS stamp was pressed on the resin until the contact between the PI film and the stamp was reached, and a pre-curing step was carried out. A UV lamp (365 nm) at a power of 6 mW/cm^2 for 12 seconds was used to partially cure the resin, after which the PDMS stamp was carefully removed, leaving the PI film with the resin spacer containing the pattern (i.e. the channel) stamped on it. After this, two holes were punched as inlet and outlet, a glass cover slip was placed on top, and the whole sandwich structure was exposed to UV radiation for 300 s to complete the curing of the structure.

The selected designs for microchannels were intended to reproduce the two most used 3D printing nozzles: blunt and conic, as shown in Figure 5.4k in the channels with the sharp (S) and progressive (P) contraction, respectively. Both channels were designed with an equal contraction ratio from 1.25 mm to 100 μm in width. The blunt channel has a straight channel as a sample reservoir of 1.25 mm width followed by a sudden contraction to 100 μm x 3.25 mm straight channel. The conic design has a similar wide channel as the sample reservoir, followed by a progressive contraction of 5 degrees to 100 μm with a total length of 6.5 mm. The thickness of the NOA layer defining the height of the channel was 250 μm for all the produced channels. The microfluidic channels and the necessary tubing were assembled in an aluminium holder fixed in the scanning SAXS setup. Syringe pumps (Cetony, neMESYS 290N) were used to have a controlled flow of 0.03, 0.30 and 3.00 μL/s during the whole experiment.

5.4. Rheology

Rheology is the branch of science that studies the deformation and flow of matter and aims to relate the macroscopic behaviour with the nanoscopic structure. Two common ideal states for matter are perfectly elastic solids and ideal viscous liquids. Real-life materials are far from ideal, especially soft matter commonly presents a complex behaviour called viscoelasticity. Elasticity is the ability to resist a deformation caused by a force, returning to the original shape when it is released. In general terms, it is generated by strong but flexible bonds in the atomic structure. Viscosity, in contrast, is the flow resistance caused by the internal friction of molecules or particles with non-permanent bonds when they are forced to move from their equilibrium positions. The viscosity (η) is usually defined in systems with shear, where it is dependent on the shear stress (σ) and the velocity gradient or shear rate ($\dot{\gamma}$) as in Equation 5.1. The shear viscosity can have two different behaviours. If the viscosity is independent of the shear rate, it is considered a Newtonian fluid. However, when the viscosity depends on the shear rate, the fluid is considered non-Newtonian, and its response becomes not linear.[157]

$$\sigma = \eta\dot{\gamma} \qquad \text{Equation 5.1}$$

A common way to measure the viscoelastic behaviour is through oscillatory tests, in which the sample is sheared between two plates with small amplitude oscillations at different frequencies. In such measurements, the upper plate oscillates with a given stress or strain amplitude and at a given frequency. A sinusoidal wave can represent the movement in time with the stress or strain as the amplitude. If the stress is controlled, the plate applies torque, and the displacement is measured. In a strain-controlled experiment, the angular displacement is controlled, and the necessary torque to reach that displacement is measured (from where shear stress is calculated). The result of these experiments is the complex modulus (G^*) which measures the deformation resistance (stiffness) as in Equation 5.2. The elastic component of the complex modulus (storage modulus: *G'*) represents the stored elastic energy, and the viscous component (loss modulus *G''*) represents the energy lost during the deformation due to the internal friction of the fluid. In the mathematical description of the complex modulus, the storage and loss moduli represent the real and imaginary parts, respectively. From this expression, the complex viscosity (η^*) can also be defined in Equation 5.3 such as the total resistance to flow as a function for the angular frequency of the oscillation (ω).[158]

$$G^* = G' + iG'' = \frac{\sigma_{max}}{\gamma_{max}} \qquad \text{Equation 5.2}$$

$$\eta^* = \eta' + i\eta'' = \frac{G^*}{\omega} \qquad \text{Equation 5.3}$$

The rheological characterization of the lyotropic liquid crystals used in ***Paper I*** and ***II*** were carried out using an Anton Paar MCR702 TwinDrive rotational rheometer in a separate motor-transducer (strain-controlled) configuration. The viscoelastic modulus in ***Paper I*** and viscosity curves in ***Paper I*** and ***Paper II*** were obtained by oscillatory and steady shear measurements. A configuration of parallel plate geometries of 25 mm in diameter was used for all the experiments, except for the oscillatory tests in the hexagonal liquid crystal of the polymer F-127, where parallel plates of 7 mm and 15 mm were used. Strain sweep tests were performed at 1.0 rad/s for a shear strain amplitude range from 0.02 to 200 %. Frequency sweep tests were performed at angular frequencies, with a constant strain amplitude of 0.01 % in the linear viscoelastic range, as determined from the strain-sweep tests. The steady shear tests were performed at a shear rate from $9.0 \cdot 10^{-4}$ to 30 s^{-1}.

5.5. Small-Angle X-ray Scattering (SAXS)

Small-angle X-ray scattering (SAXS) experiments were carried out at the cSAXS beamline, Swiss Light Source (SLS) at the Paul Scherrer Institute (PSI, Switzerland) with a micro-focused X-ray beam. A monochromatic beam with a photon energy of 11.2 keV (1.107 Å) was defined using a fixed-exit double crystal Si (111). The beam was vertically focused with a bendable Rh-coated mirror and horizontally focused by bending the second monochromator crystal. A flight tube with a length of 2 m was placed between the sample and the detector to minimize the air scattering and absorption. The transmitted beam was used for transmission correction of the scattering signal.[159] The transmission signal was measured with a photodiode on a beamstop placed inside the flight tube for ***Paper I*** and ***II***, and by measuring the X-ray fluorescence of a steel beamstop with a CyberStar (Oxford Danfysik) detector, proportional to the direct beam intensity, in ***Paper III*** and ***IV***. The scattering signal was recorded by a Pilatus 2M detector (1475×1679 pixels, 172×172 μm^2 per pixel) after the flight tube.[160, 161]

The high-resolution SAXS tensor tomography experiments in ***Paper IV*** were done at the microfocus beamline (ID13) of the European Synchrotron Radiation Facility (ESRF, France). A beam of 13.0 keV (0.954 Å) was defined by a channel-cut Si(111) monochromator with a bandwidth of approximately 10^{-4}. The beam was focused by a pair of Pt-coated fixed elliptical curvature Kirkpatrick Baez (KB) mirrors and by a set of beryllium compound refractive lenses. A small flight tube was placed between the sample and the detector to minimize the air scattering and absorption after which there was a small beamstop to block the direct beam. The scattering signal was recorded using a Eiger 4M detector (2070×2167 pixels, 75×75 μm^2 per pixel) placed after the flight tube.

5.5.1. Scanning SAXS

The 2D samples for the scanning SAXS experiments were mounted on a motorised stage with movement in 2 axes in the plane perpendicular to the incoming beam (X-Y plane), which allows for a raster scan. We carried out the experiments using fly-scanning in the horizontal direction for ***Paper I*** and ***II***, and in the vertical direction for ***Paper III*** and ***IV***, using the experimental parameters summarised in Table 5.2.

Table 5.2. Experimental parameters used in the scanning SAXS experiments. A smaller area in selected samples was measured at a higher resolution, denoted as HR in ***Paper IV***.

	Paper I	**Paper II**	**Paper III**	**Paper IV**	**Paper IV (HR)**
Synchrotron	SLS	SLS	SLS	SLS	ESRF
Beamline	cSAXS	cSAXS	cSAXS	cSAXS	ID13
Beam Energy (keV)	11.2	11.2	11.2	11.2	11.2
Sample-to-Detector Distance (mm)	2 158	2 158	2 183	2 166	2 166
Beam Size (μm)	40×40	40×40	20×7.5	25×8	25×8
Step Size (μm)	40×40	40×40	25×25	20×20	10×4
Exposure Time (ms)	200	80	35	40	40

The scattering patterns for each scanning point were divided into 16 (***Paper III*** and ***IV***) or 64 (***Paper I*** and ***II***) azimuthal segments and integrated using the cSAXS MATLAB package.[162] The data obtained in ***Paper I*** and ***II*** using lyotropic liquid crystals were analysed by calculating the Hermans' orientation parameter and angle of orientation in each scanning point. The principal diffraction peak in both samples, which corresponds to the cylinder/lamella interspace(see Figure 4.1), was also fitted using a Gaussian peak, from which the peak position, width and amplitude were obtained.[18] The scattering signal in ***Paper III*** and ***IV*** contained information from the biomineral particles and the D-spacing of the collagen fibrils. This collagen peak manifests itself as a multi-order high-intensity peak at $q = 0.095$ nm^{-1} which was extracted from the rest of the signal in each of the 16 azimuthal segments as described for the myelin peak in Georgiadis et al.[163] The anisotropy was quantified using the procedure described by Bunk et al.,[18] fitting a cosine signal to the 16-segment azimuthal intensity. The mineral particle dimension was estimated using the models discussed in Chapter 3.

5.5.2. SAXS Tensor Tomography

SAXS tensor tomography was done in bone in ***Paper III*** and narwhal tusk in ***Paper IV***. The 3D samples were mounted on a metallic needle in a dual-axis goniometer that allows for rotation, (α) around a tomography axis (Y-axis), which in can be tilted around the X-axis (β), and scanning in the X-Y plane.[6] The stability of the samples in the X-rays was checked after each full set of rotations at each tilt angle as shown in the radiation damage. The 2D projections were measured at 6 tilt angles (β) between 0 and 45 degrees (β_{max} = 40° at ID13) and rotation angles (α) between 0 and 180 degrees for a tilt $\beta = 0°$ and 0 to 360 degrees for $\beta \neq 0°$, as summarised in Table 5.3. The angular step was reduced to a factor of $\cos(\beta)$ to ensure equal angular sampling for each tilt.

Table 5.3. Experimental parameters used in the SAXS tensor tomography experiments. High resolution measurements were done for the samples of ***Paper IV*** at ID13 (ESRF), denoted as HR.

	Paper III	**Paper IV**	**Paper IV (HR)**
Synchrotron	SLS	SLS	ESRF
Beamline	cSAXS	cSAXS	ID13
Beam Energy (keV)	11.2	11.2	13.0
Sample-to-Detector Distance (mm)	2 183	2 166	119
Beam Size (μm)	20×7.5	25×8	3×3
Step Size (μm)	45×45	25×25	3×3
Exposure Time (ms)	35	30	5
Angular Sampling $\Delta\boldsymbol{\alpha}$	5.5	3.6	2.0
Angular Sampling $\Delta\boldsymbol{\alpha}$ ($\boldsymbol{\beta} \neq \mathbf{0}$)	9.0	9.0	5.1
Tilt angles $\boldsymbol{\beta}$ (°)	$0, 9, 18, 27, 36, 45$	$0, 9, 18, 27, 36, 45$	$0, 8, 16, 24, 32, 40$

The 2D projections were aligned using an iterative alignment method.[164] The reconstruction of the reciprocal-space map was carried out following a procedure based on that described by Liebi et al.[6, 22] and further developed by Nielsen et al.[27] The 3D reciprocal space for the mineral platelet in each voxel was reconstructed using a series of spherical harmonics with coefficients a_ℓ^m with degree $\ell = [0, 2, 4]$ and order $m = [-\ell, -\ell + 1, \dots \ell - 1, \ell]$, and the main structure orientation of each voxel determined from the eigenvector associated with the smallest eigenvalue of the rank-2 tensor derived from the reconstructed $\ell = 2$ harmonic.[26] The robustness of the reconstruction was checked by visual comparison of 2D orientation, anisotropy, and degree of orientation between the measurements and simulated projections of the reconstructed data. The degree of orientation was calculated as the ratio between the isotropic tensor coefficient, a_0^0 and the full tensor.[6] In addition, A q-resolved reconstruction was performed on the SAXS tensor tomography datasets in order to extract the mineral platelet thickness. In more detail, the scattering vector q was divided in 180 logarithmically spaced bins, and a reconstruction of the first coefficient of the spherical harmonics ($\ell = 0, m = 0$) was performed for each of them using as input the azimuthally averaged intensity.

5.6. X-Ray Fluorescence Spectroscopy

The fluorescence data was collected in the cSAXS beamline of the Swiss Light Source (SLS) at the Paul Scherrer Institute (PSI, Switzerland). A monochromatic X-ray beam of 11.2 keV was focused to 25×8 μm in the horizontal and vertical direction, respectively, using the monochromator and focusing mirrors as previously described in Section 5.5. The samples were oriented perpendicular to the X-ray beam in a transmission set-up and raster-scanned through the beam with a motor step of 20×20 μm for 40 ms per point. The fluorescence emission was recorded at an angle of 45° using a Ketek VIAMP KC00-C1T0-H030-ML8B 133 Silicon drift detector with XIA FALCONX electronics. The fluorescence data measured was analysed using the software package PyMCA.[165] The spectra were calibrated and fitted to obtain the element maps for each measured 2D slice. The K fluorescence signals of Ar, Ca, Fe, Ni, Ti, V, and Zn were fitted in each pixel, considering the escape and pile-up signals in the model.

5.7. Birefringence Microscopy

Birefringence microscopy, introduced in Chapter 2, was used to quantify the retardance and angle of the optical fast axis of the lyotropic liquid crystals in ***Paper II*** and narwhal tusk in ***Paper IV*** using the imaging system Exicor Birefringence MicroImager™ (Hinds Instruments, Inc., OR). The optical set-up consists of a linear polarizer at 0°, a photoelastic modulator (PEM) at 45°, a PEM at 0° and a linear polarizer at 45°. The samples are placed in the image stage between the two PEM and measured with magnifications of 2x, 10x and 20x. A 2048×2048 pixel 12-bit CCD camera created a field of view of 5×5 mm (2.5 μm/pixel), 1×1 mm (0.50 μm/pixel) and 500×500 μm (0.25 μm/pixel), respectively. A stroboscopic LED source with a wavelength of 475 nm was used to calculate the Mueller matrix components (M) and provide quantitative measurements of the sample retardance Γ (Equation 5.4) and angle of the optical fast axis θ (Equation 5.5) with spatial resolution.[36, 37] The angle of the fast axis is colour-coded from -90° to 90° for a more straightforward interpretation.

$$\Gamma = \arctan\sqrt{(M_{24}/M_{44})^2 + (M_{34}/M_{44})^2} \qquad \text{Equation 5.4}$$

$$\theta = \frac{1}{2}\arctan(M_{24}/M_{34}) \qquad \text{Equation 5.5}$$

Chapter 6

Results and Discussion

In the following sections, different imaging methods are used to study the nanostructure of biological and bioinspired materials in 2D and 3D. The chiral structure of narwhal tusk is investigated using X-ray scattering and polarised light. The same techniques are later used to assess the quality of regenerated bone and its degree of integration in two environments: polymeric fibrillar scaffolds and metal-based 3D printed implants. Lastly, the 3D printing process of bioinspired self-assembled lyotropic liquid crystals is followed to understand their nanostructure and anisotropy during flow. This chapter contains a summary of the results included in more detail in ***Paper I*** to ***IV*** as well as some unpublished results obtained during the same period.

6.1. Nanostructure of Narwhal Tusk

The results shown in this section summarise main findings of ***Paper IV*** using X-ray imaging techniques and birefringence microscopy as well as additional measurements using X-ray fluorescence spectroscopy to investigate the hierarchical structure of one interesting example of mineralised tissue: narwhal tusk. These results set the baseline in the basic nanostructure of tusk and bone (i.e., mineralised collagen fibrils), applied in the following sections with direct applications of materials for bone regeneration (Section 6.2) and bone-inspired composites (Section 6.3).

The essential building blocks of the tusk are identical to tooth and bone. Ordered collagen microfibrils are mineralised with calcium phosphate nanoparticles, as described elsewhere.[55, 57, 60] The diffraction and scattering signal of representative points in the narwhal tusk in the dentine area are shown in Figure 6.1. At wide angles, the X-rays diffract from the crystalline structure of the biomineral particles in the tusk, corresponding to hydroxyapatite nanocrystals (Figure 6.1a-b). The scattering pattern of narwhal tusk at small angles (Figure 6.1c-f) is dominated by a strong contribution at high q-values from the mineral nanoparticles. Their anisotropic shape and orientation in the tissue produce an anisotropic intensity distribution in the scattering, as shown in two opposite azimuthal orientations. The mineral particle scattering anisotropy is perpendicular to the long dimension of the particle, which is known to be mostly parallel to the collagen fibrils.[58, 59, 91] One feature of collagen, evident in the scattering signal, is a multi-order high-intensity peak corresponding to the axial periodicity between the electron density of the microfibrils and the mineralised gaps (D-period). Only the 1st and 3rd order are often visible in bone, tooth, and tusk, with anisotropy along the fibril-gap axis due to the superposition of higher order by the mineral plates.[88, 89] At low q-values, collagen has a contribution perpendicular to the previous one from the fibril diameter.[166, 167] As shown in the X-ray scattering experiments, tusk and bone are comparable in the basic arrangement at the nanoscale.[92, 93]

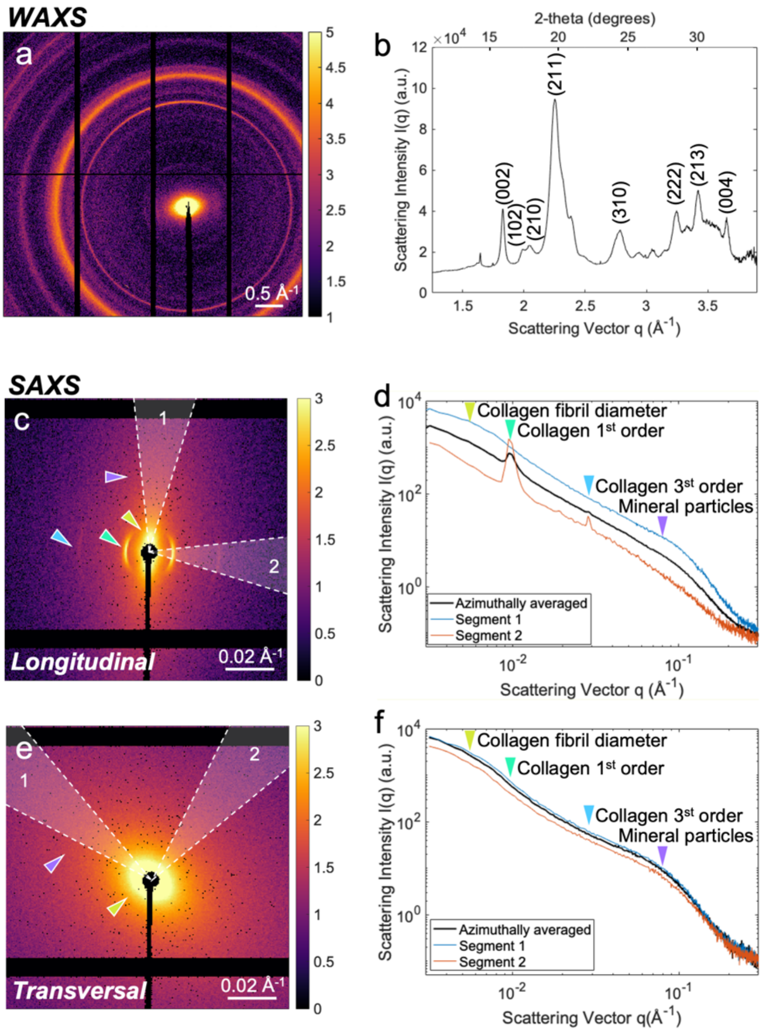

Figure 6.1. Representative scattering patterns of the narwhal tusk from dentine. Wide-angle X-ray scattering pattern (**a**) showing the diffraction of the hydroxyapatite crystals in tusk (**b**). Small-angle X-ray scattering patterns of the tusk longitudinal (**c-d**) and transversal (**e-f**) cuts. The scattering pattern is composed of the diffraction signal of collagen and the scattering contribution from the mineral particles. **d, f**) Integrated signal for two 90°-opposed segments and their azimuthally integrated signal. The segments show the difference in the anisotropy of the scattering intensity.

The narwhal tusk appears to have a very strong anisotropy, as reflected in the scattering patterns at different orientations. Significant differences are observed between two perpendicular slices in the longitudinal and transversal directions. Even though the effect is significantly stronger in dentine, cementum also has a relatively high anisotropy compared with other mineralised tissues such as bone. As seen between Figure 6.1d and 6.1f, while the signal of the collagen fibrils is evident in the longitudinal sections, it is only weakly present in the transversal section. The orientation of the scattering of the mineral particles (perpendicular to the orientation of the scattering of collagen fibrils) is homogeneous and with a high degree of anisotropy in the longitudinal slice, which contrasts with the orientation of the transversal slice. Those two projections of the scattering signal reflect an in-plane / out-of-plane orientation of collagen in the longitudinal and transversal directions, respectively. When the collagen fibrils are in out-of-plane orientation, the diffraction signal is not in Bragg conditions, and therefore it cannot be visible in those scanning points.

6.1.1. Microstructure of the Spiral Tusk

In order to understand the arrangement of the mineralised collagen fibrils, SAXS tensor tomography was used, which allows to retrieve the three-dimensional orientation spatially resolved in each voxel of a three-dimensional sample.[22] The reciprocal space map of the scattering signal corresponding to the mineral particles (q = 0.36 – 2.25 nm^{-1}) was reconstructed with a cubic voxel size of 25 μm. Two differentiated regions with low and high degree of orientation, cementum and dentine respectively, are clearly visible in Figure 6.2a. The orientation of the mineralised collagen fibres, represented by the direction of the streamlines is mostly aligned in the longitudinal direction of the tusk. Two additional projections show a curved pattern rather than straight lines, showing a slight turn in the transversal plane (Figure 6.2b-c). An additional projection of the streamlines in the radial direction clearly shows that the collagen fibrils in dentine have a twist with respect to the radial axis of approximately 6.15 °/mm in the dentine (Figure 6.2d). An offset between the orientation of the dentine and cementum of ~6° is also obvious in Figure 6.2e.

Multiple intensity maxima were found while visualising the spherical harmonics reconstructed in the cementum area (Figure 6.2f), a sign of multi-domain averaging, which may contain multiple orientations in a single voxel. For that reason, higher resolution SASTT was done reducing the voxel size from 25 μm to 3 μm (Figure 6.2h). The orientation of the reconstructed reciprocal space map shows the consistent axial orientation in the dentine (Figure 6.2i). In the cementum region, an overall lower degree of orientation is found, but some areas with more complex orientation are visible. Some variations from the axial direction can be observed in the outer surface (Figure 6.2j), where vertically oriented domains appear embedded in an axially oriented matrix.

Complementing the SASTT, 2D scanning SAXS measurements were performed in longitudinal and transversal slices to study the microstructure in a larger area. The spatial distribution of the tusk hierarchical structure based on the anisotropy of the scattering signal of mineralised collagen fibrils was studied by fitting a cosine function to the azimuthal intensity distribution as described by Bunk et al.[18] The symmetric intensity of the q-ranges associated with the mineral particles (q = 0.36 – 2.25 nm^{-1}) and mineralised collagen fibrils ($q = 0.86\times10^{-1} - 1.13\times10^{-1}$ nm^{-1}) is relatively homogeneously distributed in the longitudinal sample within the dentine (Figure 6.3a and 6.3g), where the cementum layer has a generally lower intensity in the signal related to collagen. Similarly, the transversal sample shows an increasing scattering intensity for minerals across the whole sample from the pulp chamber to the cementum junction (Figure 6.3b). The diffraction of collagen is in Bragg conditions only in the cementum layer and not in the dentine (Figure 6.3h); therefore, it cannot be detected there. In contrast to dentine, the symmetric intensity of both components in cementum is comparable in the transversal and longitudinal cuts. That is in line with the predominant orientation of collagen in dentine in the longitudinal direction found in SASTT, and a more complex orientation in the cementum.

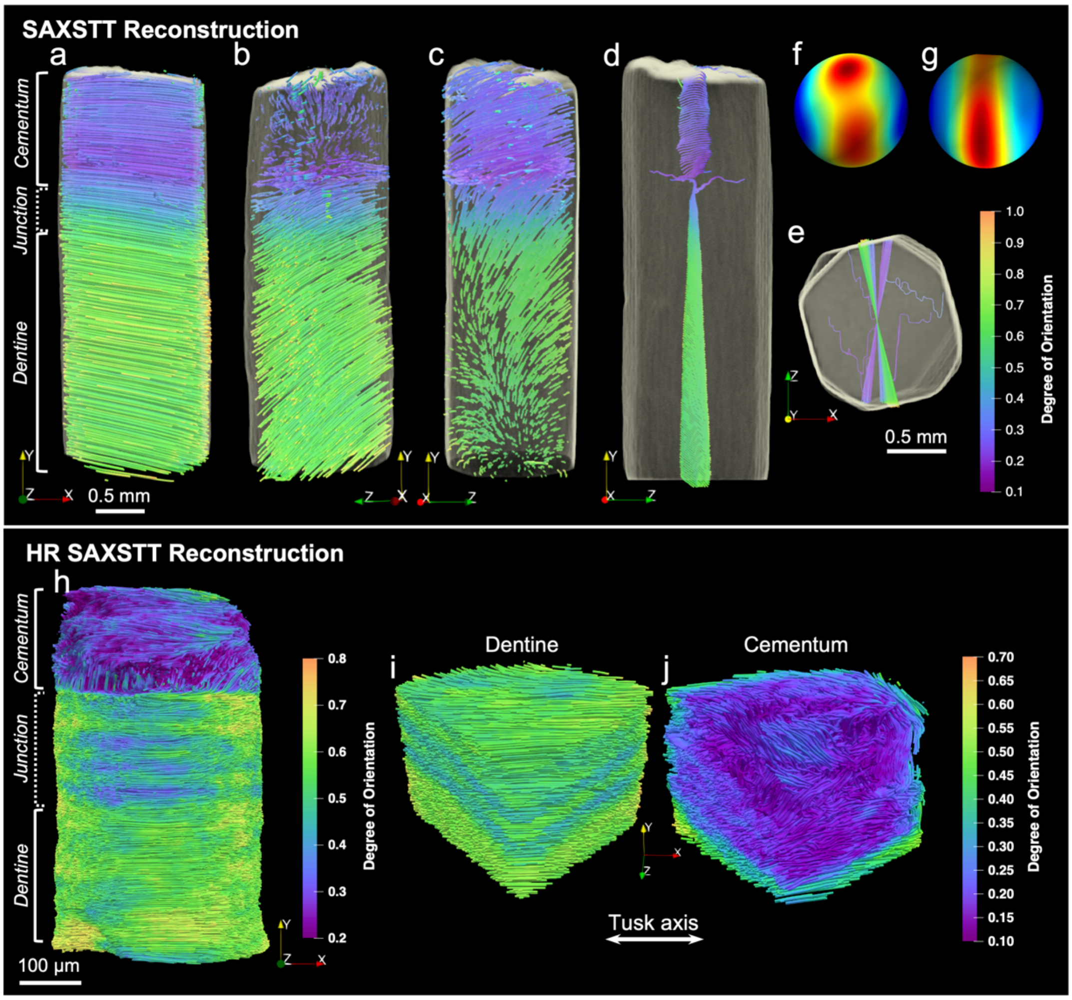

Figure 6.2. 3D representation of the mineralised collagen fibrils orientation in the narwhal tusk. The reciprocal space map of the scattering in a q-range corresponding to the mineral particles was reconstructed using SAXS tensor tomography with a cubic voxel size of 25 μm (**a-c**) and 3 μm (**h-j**). The morphology of the sample was reconstructed using the X-ray transmission signal measured during the experiment. Narwhal tusk at three different perspectives showing the main orientation of dentine and cementum (**a-c**). A vertical slice shows the twist in the radial direction and an offset between the orientation of cementum and dentine (**d-e**). The 3D reconstruction is plotted in parallel view to avoid perspective artefacts. The virtual slices are represented for every second point for easier visualisation. Reconstructed spherical harmonics of cementum (**f**) and dentine (**g**) in representative positions. High-resolution SAXS tensor tomography of narwhal tusk (**h**) and two subvolumes in the dentine (**i**) and cementum (**j**) regions.

A high degree of orientation was obtained in the longitudinal samples for both the mineral (Figure 6.3c) and collagen (Figure 6.3i) contributions, and a very homogeneous direction of orientation in the tusk axial direction (Figure 6.3e and 6.3k). The transversal samples show a low degree of orientation for the scattering of the mineral particles (Figure 6.3d) and mineralised collagen in dentine (Figure 6.3j), which is in line with a main orientation along the tusk. The orientation of the anisotropy, although low, has a wide distribution of angles. A fan-like orientation is seen in the dentine with discontinuous radial structures from the pulp chamber to the cementum (Figure 6.3f). A more complex orientation is observed in the cementum layer, which presents a top region with a wave-like pattern and a layered bottom area (Figure 6.3f and 6.3l).

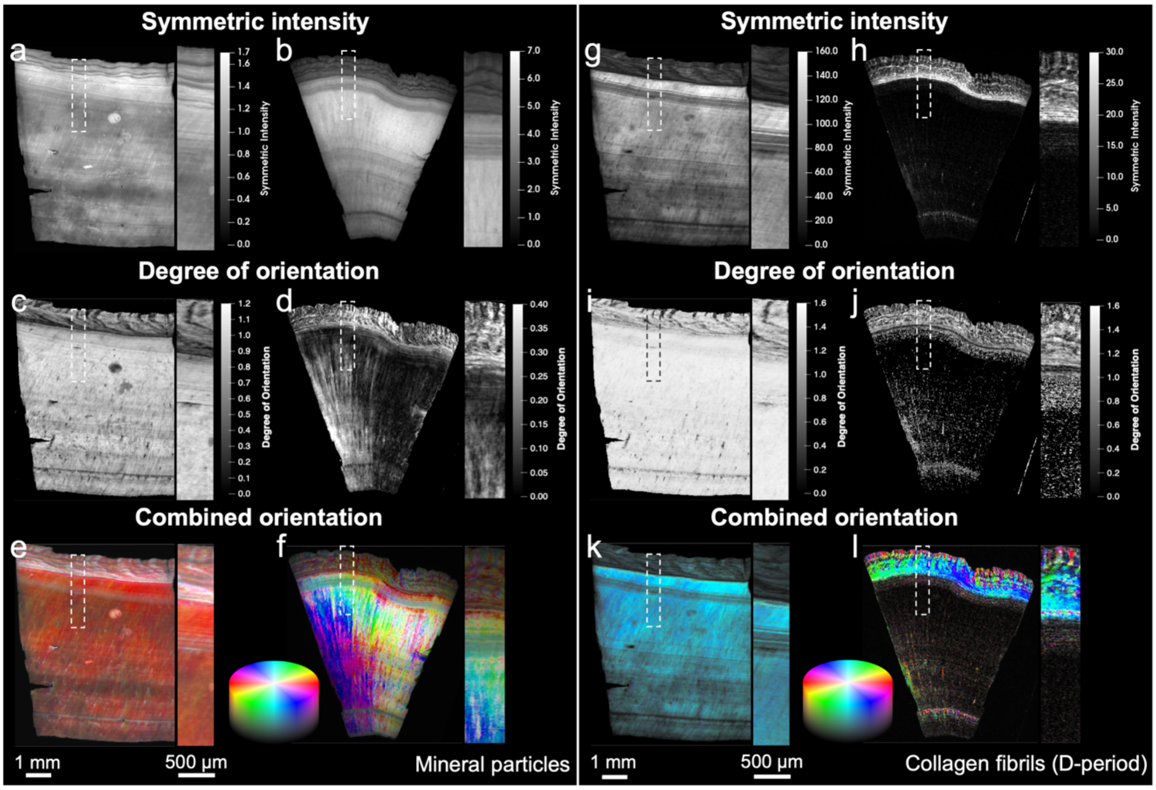

Figure 6.3. Anisotropy of the scattering signal of longitudinal (**left**) and transversal (**right**) cuts of narwhal tusk with a resolution of 20×20 μm and 4×10 μm in an area marked with dashed lines. The anisotropy has been calculated for the contribution of the mineral particles (**a-f**) (q = 0.36 – 2.25 nm^{-1}) and mineralised collagen fibrils (**g-l**) (q = 0.86×10^{-1} – 1.13×10^{-1} nm^{-1}). The symmetric intensity (**a-b** / **g-h**) and degree of orientation (**c-d** / **i-j**) are plotted according to the colour scale. A symmetric intensity mask was applied to the degree of orientation to avoid artefacts from the background noise. The combined orientation (**e-f** / **k-l**) is colour-coded according to the colour cylinder. The hue shows the direction, the value shows the symmetric intensity, and the saturation shows the asymmetric intensity. Highly oriented material appears with bright colours, whereas low-oriented material appears in grayscale, with the grey value proportional to the total scattering intensity.

Figure 6.4 shows the intrinsic birefringence of collagen fibrils in the tissue.[100] The retardance is proportional to the in-plane degree of anisotropy of collagen and inversely proportional to the out-of-plane orientation. A much higher retardance is observed in the longitudinal than in the transversal sample (Figure 6.4a-b), in line with the degree of orientation obtained from scanning SAXS. Within each sample, the retardance in the dentine increases from the pulp to the cementum layer in the longitudinal sample and decreases in the transversal cut. In birefringence, the collagen in the dentine is visible in the transversal slice and not only in the cementum due to the different origin of the measured signal. The angle of the fast-axis, which shows the angle of orientation in the mineralised collagen fibrils, is combined with the retardance, showing brighter colours for the regions with higher anisotropy. The fast-axis in the longitudinal sample shows the fibrils aligned in the longitudinal direction (Figure 6.4c), contrary to the transversal slice where the radial fan-like patterns and columnar structures are seen (Figure 6.4d). That supports the distribution of orientations found in the scattering experiments. Higher magnification images show the radial columnar structures, which have been referred to as matrix bands[168] (Figure 6.4i and 6.4k). A perpendicular projection of those structures has a much more homogeneous orientation, as seen in the longitudinal samples (Figure 6.4e and 6.4g). The cementum region has an interesting distribution of angles, with the already mentioned wave-like pattern in the outer layer (Figure 6.4f and 6.4h). Below that, woven patterns between two relatively perpendicular orientations can be observed (Figure 6.4m). Vertically oriented features with low retardance can be observed in Figure 6.4f and 6.4h with a yellow colour, matching the high retardance areas in Figure 6.4j and 6.4l. Those opposed patterns reflect the perpendicular orientation of collagen for each region.

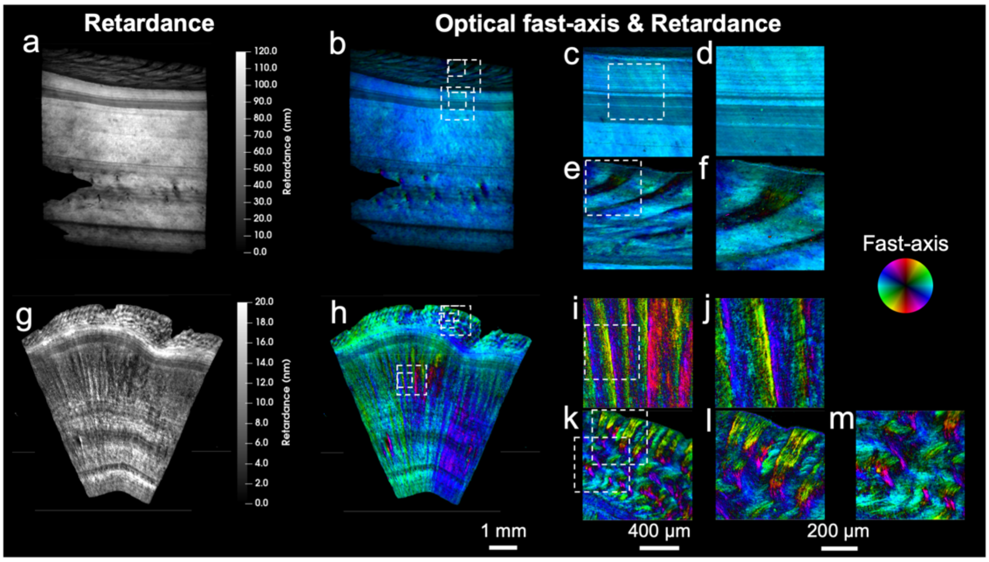

Figure 6.4. Anisotropy of the birefringence signal of longitudinal (**left**) and transversal (**right**) cuts of narwhal tusk. The samples were imaged with a wavelength of 475 nm. The retardance of the samples is expressed in nanometres (**a-b**). The angle of the fast axis is plotted with the retardance according to the colour wheel. The hue shows the direction of the optical fast-axis, and the value shows the retardance (**c-d**). Material with high retardance appears with brighter colours. Several regions of interest in the dentine (**e**, **g**, **i** and **k**) and cementum (**f**, **h**, **j**, **l** and **m**) were imaged at higher magnifications.

The multiscale orientation analysis provided by the scattering and birefringence results have two main implications. First, the scattering signal of the mineralised collagen fibrils is strongly oriented in the longitudinal direction. That is shown in both the X-ray scattering and birefringence experiments, especially in the 3D orientation in SASTT and in the high degree of orientation and constant orientation in the longitudinal cuts in scanning SAXS. The transversal direction has a low degree of orientation and no presence of the diffraction signal from the collagen gap along the fibres. Thus, the mineralised collagen fibrils are oriented along the longitudinal direction, relatively parallel to the tusk axis. Scattering experiments to study the microstructure of tusks are rare; however, other research has also shown that the mineralised collagen fibrils present a strong anisotropy in the axial direction in elephant tusk.[169] In this scenario, it can be assumed that the orientation seen in the transversal samples is the minor deviations from the tusk axial direction. These results also show a lower degree of orientation in cementum, as confirmed by SASTT and consistent values in scanning SAXS and birefringence. A low degree of orientation is a consequence of a less defined orientation at this length scale, as well as a broader distribution of angles. That is supported by observations done with high-resolution SASTT and birefringence microscopy.

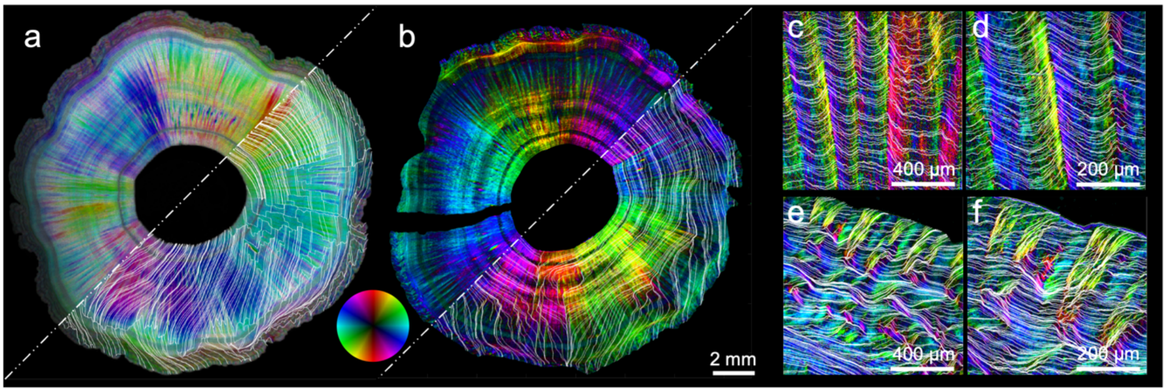

Figure 6.5. Streamlines of the real-space orientation of mineralised collagen fibres measured in scanning SAXS (**a**) and birefringence (**b-f**). Complete transversal cuts of the narwhal tusk imaged by scanning SAXS (**a**) and birefringence microscopy (**b**). High-resolution birefringence microscopy images from the dentine (**c-d**) and cementum (**e-f**) in the transversal plane, as previously shown in Figure 6.4. The scanning SAXS image was obtained at the cSAXS beamline with a different experimental configuration than the one explained in Materials and Methods, using a 35 μm step size and an exposure time of 30 ms at a photon energy of 12.4 keV. The birefringence images were obtained using a wavelength of 475 μm. The images were post processed before calculating the streamlines with a Gaussian filter to decrease the noise level in the vectorial components of the angles using a kernel of 2×2 for (**a**) (field of view 571×571 pixels), 20×20 for (**b**) (field of view 7500×7500 pixels) and 3×3 for (**c-f**) (field of view 2048×2048 pixels).

Secondly, the axial deviations (i.e., out-of-plane orientation in the transverse cuts) in dentine do not follow a random pattern but an ordered arrangement at the microscale. The mineralised collagen fibrils are highly aligned in the axial direction with small deviations arranged in a helical distribution, as shown in Figure 6.5a-b and in the 3D representation in Figure 6.2c. The streamlines calculated from the vectorial components of the angles at each point show an organised pattern where the mineralised collagen fibrils wrap around the pulp chamber with an increasing radius in a helical shape. The columnar structures observed in the higher resolution birefringence images (Figure 6.4i and 6.4k) correspond to micro-lamellae of dentine (i.e., matrix bands) previously observed in histological studies.[168] The representation of the orientation of these bands using the streamlines in Figure 6.5c-d, show a ridged pattern with peaks of high / low retardance, corresponding to the orientation changes in the collagen fibrils.[170] Similar patterns have been found using polarised light in the Schreger patterns of elephant tusk, where the collagen fibrils were the source of the birefringence signal.[171] The axial deviations in cementum show a very different structure compared to dentine. The degree of orientation in the reconstructed reciprocal space map, and the retardance in birefringence are comparable in magnitude when viewed in transverse and longitudinal cuts, resulting from a much smaller anisotropy, not aligned in the axial direction. A repeating feature is found in the outer layer of cementum with orientations perpendicular to the surface of about 100 – 200 μm in diameter. In these areas, aligned collagen is observed in the transversal direction radially oriented to the surface of the tusk. In the high-resolution SASTT visualisation, radially oriented voxels are also observed (Figure 6.2j), embedded in an axially aligned matrix. The size of those aligned collagen bands is comparable to the average size of the periodontal ligaments, which are inserted in the cementum at the growth chamber, holding the tusk in place and connecting it to the maxillary bone.[172]

6.1.2. Nanostructure of the Mineralised Collagen Fibrils

The nanostructure of the collagen fibrils can be followed by studying the diffraction signal of collagen. The 1st order of the collagen diffraction signal along the fibril axis was fitted using a Gaussian, where the amplitude, position and full width half maximum were obtained. The diffraction signal of collagen is not in Bragg conditions in the transversal cuts, only visible in some areas of the cementum with very low intensity. Therefore, only the diffraction peak measured in the longitudinal slices is shown in Figure 6.6a-c. The peak position, given by the period in the collagen fibril along its long axis, has an average value of 9.77×10^{-3} Å^{-1}, corresponding to a collagen D-period of 64.25 nm (Figure 6.6a). Certain variations within the dentine and a slightly higher average value in the cementum are found. The cementum presents a peak position of 9.95×10^{-3} Å^{-1}, corresponding to a D-period of 63.15 nm. The peak amplitude has a very similar texture as the peak position, with an equivalent value between dentine and cementum (Figure 6.6b).

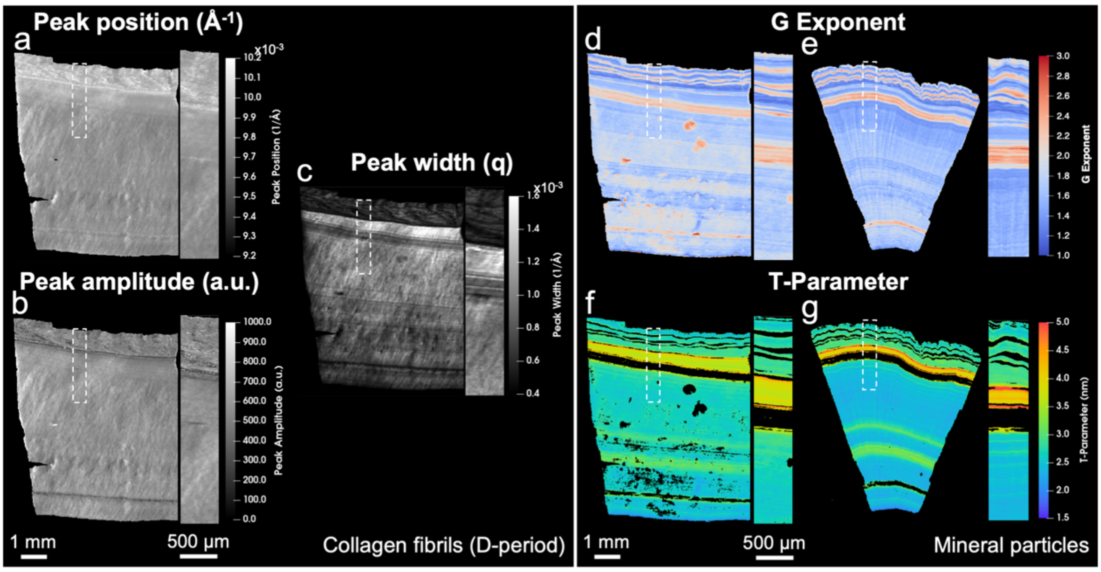

Figure 6.6. Peak fitting of the 1st order reflection in the collagen diffraction signal ($q = 0.90\times10^{-1} - 1.13\times10^{-1}$ nm^{-1}), showing the position (**a**), amplitude (**b**) and width (**c**) in the longitudinal cut. The collagen diffraction signal in the transversal slices was only present in the cementum, where the intensity was too low to be fitted. Mineral particle morphology in the longitudinal and transverse cuts. In the SAXS experiments, the *G* exponent (**d**-**e**), used to describe the shape of the particle, was calculated in the Guinier regime of the of the mineral particles ($q = 0.30 - 0.55$ nm^{-1}). The T-parameter estimated the particle thickness (**f**-**g**), calculated in the Porod region of the mineral scattering signal ($q = 1.08 - 1.67$ nm^{-1}).

In the SAXS signal, the slope at low q is an indicator of the particle shape. The G exponent obtained by fitting a power law in the Guinier region of the mineral particle scattering signal ($q = 0.3 – 0.55\ \text{nm}^{-1}$) is shown in Figure 6.6a-b. G exponents below 2 are typical of anisotropic particles, with $G = 2$ for platelet-like and $G = 1$ for needle-like particles. Higher exponents are found for rounded or spherical particle shapes.[88, 173] The G exponent in the narwhal slices has a consistent layered pattern that correlates between the transversal and longitudinal cuts. Low G exponent ($G < 2$) in the dentine is observed in Figure 6.6d-e, while cementum has a multi-layered structure of concentric bands of consecutive high and low G exponent.

The T-parameter calculated using the stack of cards model is related to the mineral particle thickness in the material. The T-parameter in Figure 6.6f-g was calculated for each scanning point with a G exponent equal to or lower than 2 to fulfil the model's particle shape assumptions.[97] The T-parameter in dentine present value between 2.0 nm and 3.0 nm in dentine, increasing up to 3.5 nm in the layers with the lowest G exponent. A generally higher value of the T-parameter is observed in the longitudinal cut compared with the transversal slice. The cementum region has a higher T-parameter with a similar value in the longitudinal and transversal projections. There is an apparent correlation of the T-parameter with the G exponent, being higher in regions with a lower G exponent, such as the cementum or the concentric bands in dentine with a lower G. The T-parameter also appears affected by the anisotropy of the material. The high anisotropy in dentine creates artifacts in the result, increasing the T-parameter in the longitudinal cut and decreasing it in the transversal one. The number of studies using scattering in tusk is scarce. However, the T-parameter was previously calculated in elephant tusk, which reached values between 2.0 nm and 2.6 nm, with lower values in the inner dentine.[169]

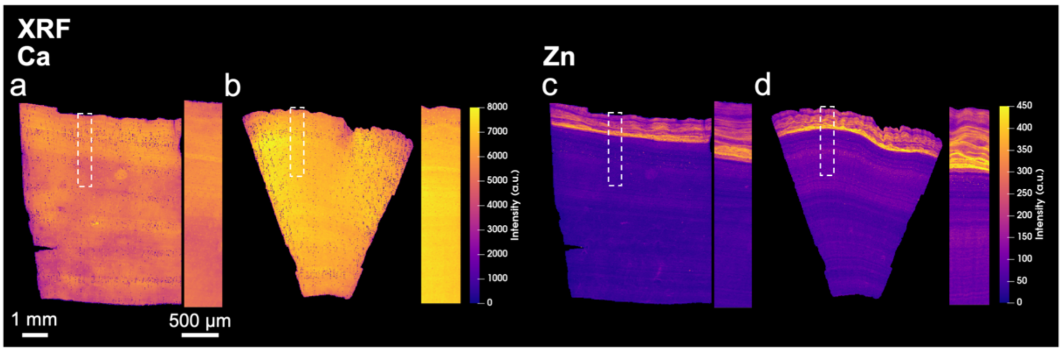

Figure 6.7. X-ray fluorescence signal of the longitudinal (a, c) and transversal (b, d) slices. The fluorescence spectrum was fitted using the software PyMCA and the distribution map for calcium (a, b) and zinc (c, d) plotted in 2D.

The elemental composition of the tusk was studied using X-ray fluorescence spectroscopy (XRF). The distribution of calcium (Figure 6.7a-b) and zinc (Figure 6.7c-d) in the transversal and longitudinal sections was obtained by fitting the fluorescence spectra in each scanning point. Even though cementum has been reported to be less mineralised than dentine, the intensity of the calcium fluorescence, related to the calcium concentration in the tissue, is homogeneously distributed in both samples. However, higher intensity is evident in the transversal slice, which can only be related to the larger thickness of that sample, which is within the reasonable penetration depth of the fluorescence signal.

Zinc is an important trace element in mineralised tissue, found in many factors and proteins that contribute to the biomineralisation process.[174] Zinc has a higher presence in the cementum than in the dentine, showing high-intensity bands as shown in the previous scattering data (Figure 6.3 and Figure 6.6). Growth bands in narwhals have been previously investigated concerning their feeding patterns and mercury exposure.[175] Such bands have been associated with the feeding patterns during the lifetime of the animals, which leave traces in the tusk. More research can be found on the growth bands of other odontocetes, such as beluga whales, whose teeth also grow continuously throughout life.[176] The formation mechanism of those bands is not entirely known, but it is hypothesised that it could be the product of changes in the mineral content. In this experiment, no solid evidence of the growth bands can be observed in the calcium and zinc elemental maps. Better resolution and higher sensitivity could be needed to resolve the changes in the element content of the growth bands. Future experiments are planned to study in more depth the growth bands in narwhal tusk, where higher energy radiation will allow for styling the fluorescence signal of other important oligo-elements in biomineralisation such as strontium.[177]

6.2. Nanostructure of Regenerated Bone

6.2.1. Fibrillar Scaffolds for Critical-Size Defects

The regenerative potential of aligned versus random PLGA/aCaP scaffolds seeded with adipose-derived mesenchymal stem cells (AD-MSC) or coated with AD-MSC-derived extracellular matrix (ECM) was investigated *in vivo*, shown in ***Paper III***. A mouse model for femoral segmental critical-size defect was used to provide information regarding the integration of the construct with surrounding tissue along with how well it sustains in the union of an otherwise non-healing bone defect.[178] Cell-seeded or decellularized scaffolds with aligned and randomly oriented PLGA fibres were implanted into the bone gaps. In total, four treatment groups were investigated: random scaffold with AD-MSCs, aligned scaffold with AD-MSCs, random scaffold with ECM and aligned scaffold with ECM (Figure 6.8).

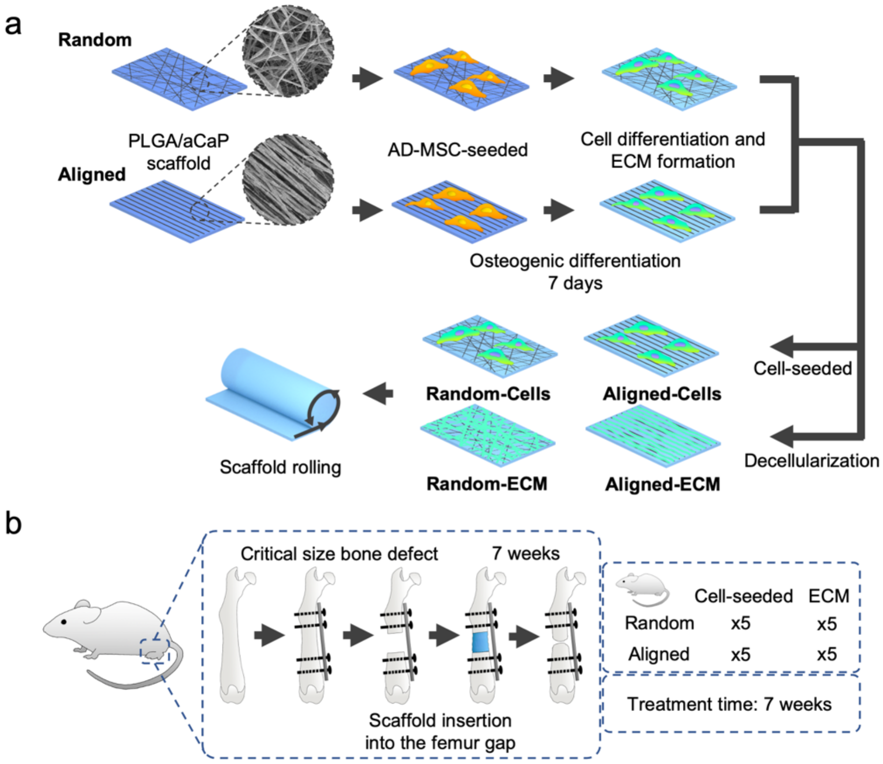

Figure 6.8. a) Preparation of the scaffold for the *in vivo* experiment. Flat aligned and random scaffolds were cultured with cells *in vitro* to obtain a homogeneous distribution of the cells on the scaffold. Half of the scaffolds were decellularized to obtain only the produced ECM. Before transferring into the mouse's femur gap, the scaffolds were rolled along the longitudinal axis, obtaining a 3D structure. **b**) Pieces of 3.5 mm were transferred to the bone defect. Lately, the mice were sacrificed after 7 weeks, and the bones were isolated for micro-CT and SAXS experiments.

Micro-computed tomography was used in the isolated femurs 7 weeks post-surgery to study the amount of bone formed in the scaffold (Figure 6.9). Volume analysis of the segmented data revealed no significant differences in the amount of new bone formed in the critical size gap between the different groups. However, aligned scaffolds with either AD-MSCs or ECM showed a trend toward increased bone formation compared to random scaffolds. Whereas in aligned scaffolds, osseointegration of the scaffold was visible and new bone formation was occurring, in random scaffolds, new bone formation was somewhat uncoordinated, generating disconnected islands of bone reminiscent of pseudo-arthrosis. Osseointegration failure was observable in all random scaffolds independently, whether they were seeded with AD-MSCs or with ECM only, while in the aligned scaffold the gap was almost completely closed through newly formed bone.

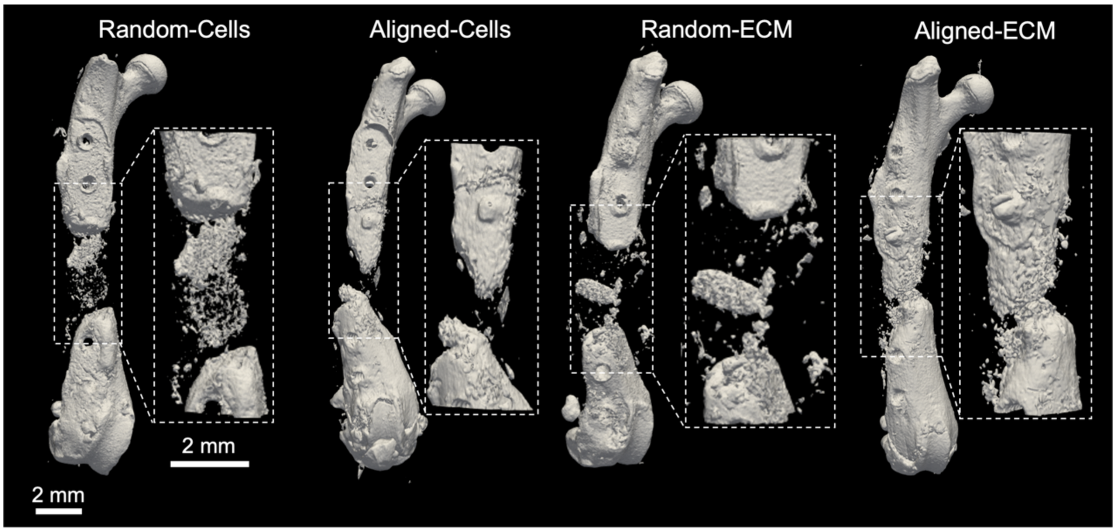

Figure 6.9. Quantification of bone regeneration in the *in vivo* mouse model for critical size bone defect. Isosurface rendering of the three-dimensional reconstruction of microcomputed tomography images of one representative femur for each experimental group. Marked with dashed lines is the region of interest where the gap was originally generated.

The influence of the morphology of the scaffold on the nanostructure of the regenerated bone was assessed using SAXS. In order to get a macroscopic overview of the bone anisotropy, the femurs were sliced and measured using scanning SAXS. Figure 6.10a-b represents the direction and degree of orientation of the mineral particles. In the aligned scaffolds, the overall orientation of the bone nanostructure is ordered along the femur long-axis. On the other side, scaffolds with randomly aligned fibres showed a rounded callus with orientation perpendicular to the femur long-axis and a low degree of orientation. The aligned scaffolds also show a higher amount of bone in the callus area, with an orientation parallel to the bone direction, similar to the direction of orientation in the native bone, indicating a high degree of osseointegration. These results indicate a correlation between the scaffold type and the degree of orientation at these length scales. A slightly more advanced bone growth could be observed in the aligned scaffold with ECM, containing a higher amount of new bone.

On the other hand, poorly aligned tissue with a low degree of orientation was observed in the gap of both random scaffold groups, visualized with grey colour in the gap of the random bones. In that region, a *G* exponent higher than 2 is observed (Figure 6.10c). High *G* exponent has been associated with areas where the bone is being formed,[179] and where the mineral nanoparticles have a more rounded shape than the typical platelet- or needle-like shape.[173] The combination of non-defined orientation, low degree of orientation and high *G* exponent could indicate the presence of tissue with certain mineral content but without the characteristic nanostructure of bone, such as ordered collagen fibrils mineralized with anisotropic particles. The T-parameter cannot be calculated since the platelet-like assumption is not fulfilled. These data further corroborate the observation that random scaffolds lack osseointegration. We further aimed to estimate the mineral particle thickness using the T-parameter for points in which the G exponent was equal to or lower than 2. A mineral thickness of 2.03 ± 0.06 nm is observed in the bone area[180] and lower values between 1.87 ± 0.04 and 1.98 ± 0.07 nm for the random and aligned scaffolds in the callus (Figure 6.10d).

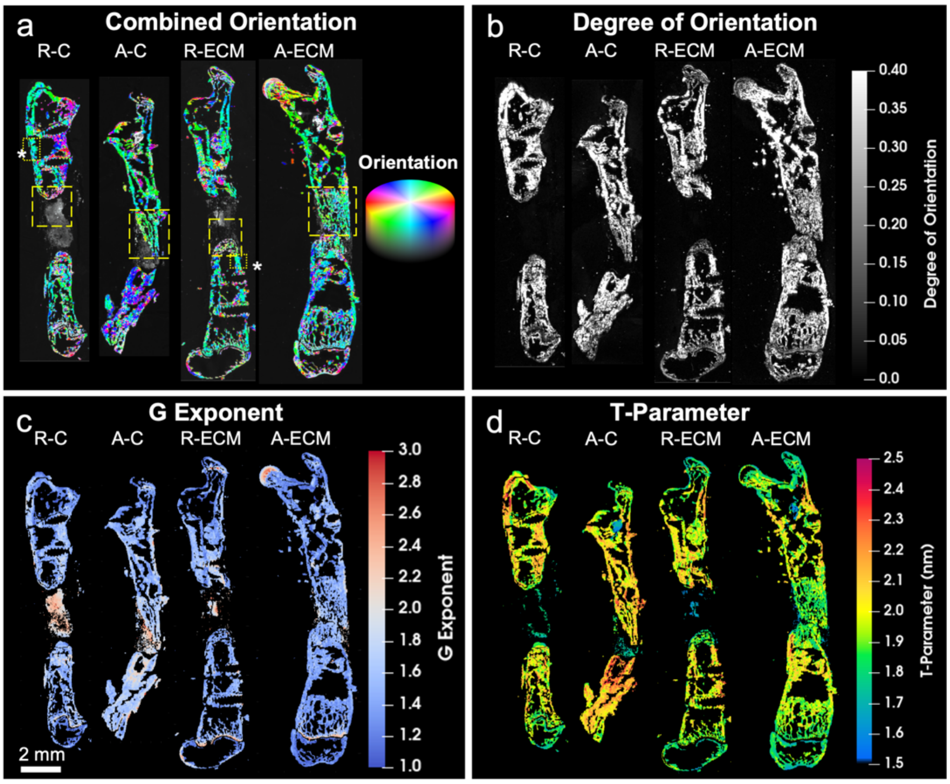

Figure 6.10. Scanning SAXS of bone sections 7 weeks post-surgery. Scattering signal from the q-range corresponding to the mineral platelets ($q = 0.331 – 2.68$ nm^{-1}). The scaffolds with random and aligned fibres are labelled R and A, respectively, containing cells C or only extracellular matrix ECM. **a**) The orientation and scattering intensity are colour-coded according to the colour cylinder, where the hue shows the direction, and the value shows the symmetric intensity. Additionally, the saturation shows the asymmetric intensity.[18] Highly oriented material appears with bright colours, whereas low-oriented material appears in greyscale, with the grey value proportional to the total scattering intensity. Of note, the anisotropy direction of the scattering signal of the mineral particles is perpendicular to their orientation in real space. **b**) Degree of orientation based on the ratio between asymmetric and symmetric intensity. The G exponent of the mineral particles at low-q (**c**) and the T-parameter (**d**), representing the mineral particle thickness in nm, is shown according to the colour scale.

To better understand the nanostructure in the 3D volume of the scaffold, a small volume containing part of the native and regenerated bone in one femur per animal group was measured using SAXS tensor tomography. The reciprocal space map of a q-range corresponding to the mineral particles ($q = 0.331 – 2.68$ nm^{-1}) in the bone was reconstructed. The direction of the mineralized collagen fibrils is represented by the direction of the cylinders and the degree of orientation by the colour scale (Figure 6.11a). Representative 2D slices of the 3D volumes are also shown in Figure 6.11b. There is a clear visual difference between the amount of regenerated bone in the random and aligned scaffolds independent of the presence of AD-MSCs or ECM. Scaffolds with random fibres showed poor growth in the gap and a rounded morphology in the callus. The aligned scaffold presented a more advanced growth with a cylindrical shape, which filled almost all the available space in the gap. The nanostructure of the callus in the aligned scaffolds followed the direction of the long axis of the femur and had similar morphology to the original bone. This factor is an indicator of an advanced regeneration process. This result also indicates a correlation between the orientation of the scaffold fibres and the nanostructure of the regenerated bone. A general lower degree of orientation was observed in the regenerated area than in the native bone, independently whether of they contained AD-MSCs or only ECM.

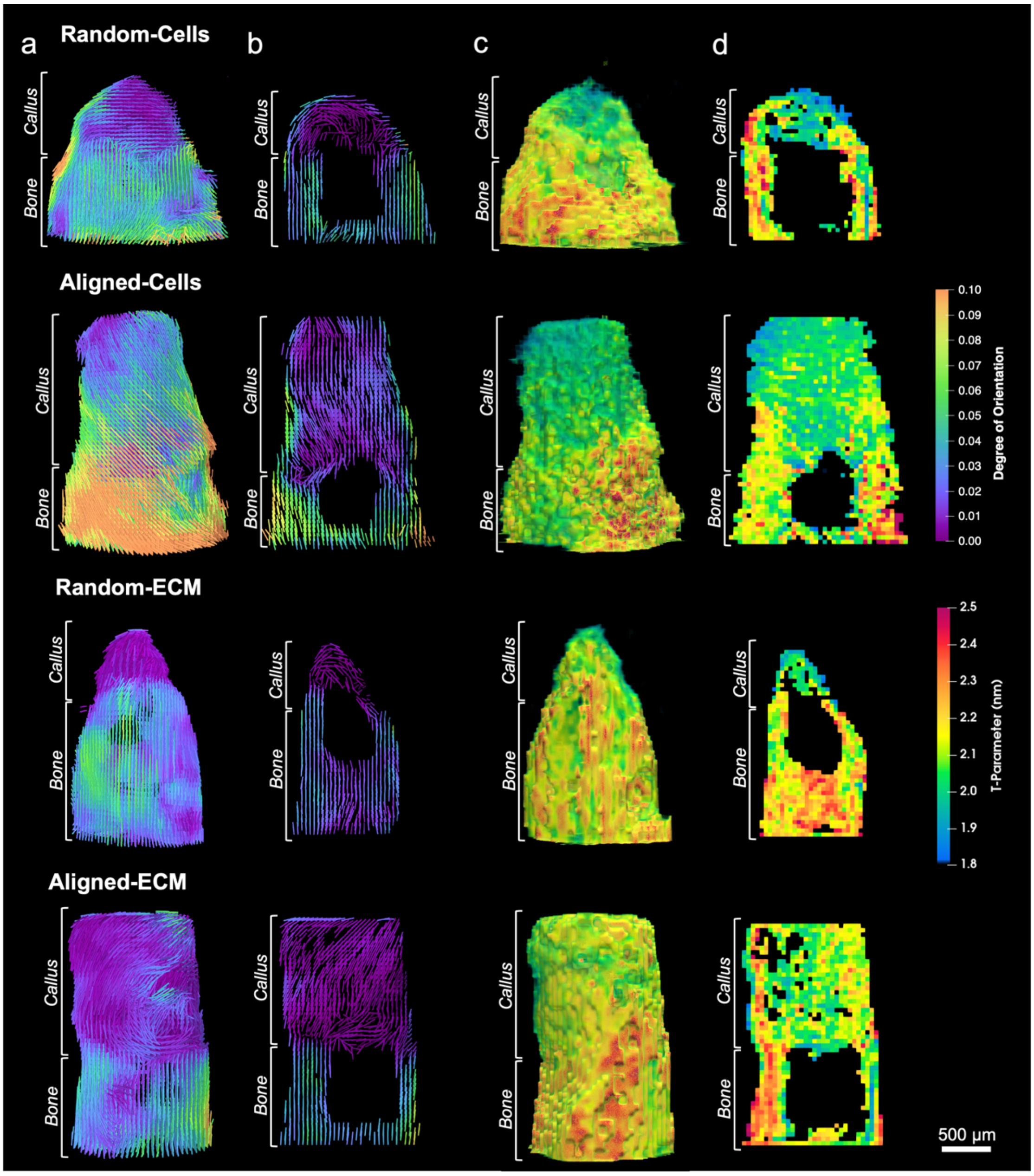

Figure 6.11. SAXS tensor tomography reconstruction of the scattering signal from the mineral particles in the regenerated volume. **a**) 3D representation of the direction of anisotropy of the spatially resolved scattering signal. **b**) Representative 2D virtual slice of each sample taken from the middle position. The direction of the cylinders shows the direction of orientation and the colour scale the degree of orientation. **c**) Thickness of the mineral particles represented in the 3D volume and in a 2D slice in the middle position (**d**).

Additionally, a q-resolved reconstruction allowed to calculate the T-parameter, which is shown in the 3D isosurface renderings in Figure 6.11c and in representative 2D virtual slices in Figure 6.11d. The values of the mineral thickness, calculated as the mean T-parameter, for the native bone is 2.18 ± 0.19 nm, as expected.[180] The regenerated bone in the callus of the random scaffolds shows a mean T-parameter of 2.04 ± 0.13 nm, while the aligned scaffold with ECM has a mean T-parameter of 2.14 ± 0.11 nm. Aligned scaffolds with ECM have a visible porosity in the callus area and a more homogeneous volume shape than the aligned scaffold with cells. In addition, a higher mineral thickness, i.e. T-parameter, indicates a more advanced regeneration process, as found in other studies[181] where more mature mineralized tissue in the callus was composed of thicker mineral particles (higher T-parameter). This observation is very interesting because it suggests that an appropriate amount and orientation of ECM are sufficient to promote bone regeneration and migration of endogenous cells from the native bone into the scaffold.

6.2.2. Metallic Titanium Implants

Metal 3D printing is a promising technology for fabricating bone scaffolds. The versatility of the 3D shape makes them suitable for reproducing cortical and trabecular structures. Titanium alloys are especially interesting for their mechanical strength, the most similar to bone among metals, and their biocompatibility.[105] Those 3D printed structures imitate the trabecular bone allowing a good growth and integration of the implant. The integration capabilities of 3D printed titanium implants were tested *in vivo* in a trabecular model, sheep distal-femurs. The implants were manufactured by powder bed fusion using electron beam melting (EBM) (Arcam AB, Mölndal, Sweden) with plasma-atomised Ti6Al4V powder (Grade 23; ASTM F136 standard).[148] Two different morphologies with large and small struts were used against a solid cylindric implant as a control. The bones were collected after 6 months, embedded in PMMA and prepared in sections for birefringence microscopy.

Birefringence microscopy measures the interaction of an optically anisotropic material with light, obtaining the direction of the optical fast-axis and retardance related to the anisotropy in the material. It is known that collagen is birefringent (see Chapter 3); however, bone has many other components. When performing birefringence microscopy and unless compared with a standard, the source of the birefringence is unknown. In scattering imaging, the information about the structure contributing to that signal can be identified and selected to create an image that will reveal its spatial distribution. Therefore, by combining SAXS and birefringence, both signals can be easily correlated, and their source identified. As shown in Figure 6.12, scanning SAXS images of the 1st order of the diffraction signal of the collagen fibrils were plotted. The same slices were previously measured using birefringence microscopy, where the angle of the anisotropy in the scattering signal and the angle of the fast axis are virtually identical in the trabecular and cortical bones. Similarly, the contrast of the asymmetric intensity and the retardance coincides with the angle of the optical fast-axis and retardance. These results confirm the correlation between the scattering and birefringence images, which confirms that the anisotropy and direction of the collagen fibrils in bone are being imaged with birefringence.

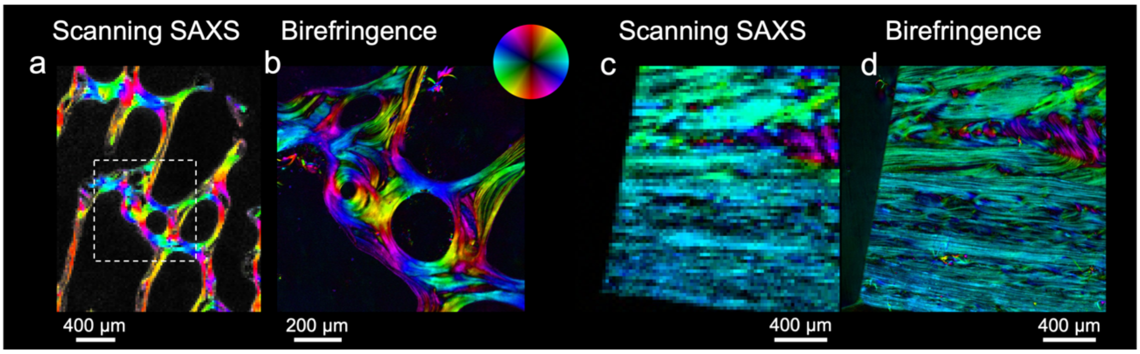

Figure 6.12. Comparison between scanning SAXS and birefringence microscopy in trabecular (**a**-**b**) and cortical (**c**-**d**) bone. The anisotropy of the collagen diffraction signal ($q = 0.80 - 1.12 \times 10^{-1}$ nm^{-1}) is plotted according to the colour wheel, where the value represents the asymmetric intensity (**a**, **c**). Birefringence microscopy shows the direction of the optical fast-axis according to the colour wheel where the hue represents the direction and the value the retardance in nm (**b**, **d**).

The morphology and microstructure of the bone grown around the implant were spatially assessed using birefringence microscopy, as shown in Figure 6.13. In the solid implant, reasonable growth on the surface with a relatively compact morphology is visible (Figure 6.13-left). The porous implants can be observed containing new tissue integrated into the pores and covering the surface of the struts (Figure 6.13-middle and 6.13-right). The implant with smaller struts has a higher degree of penetration than the larger struts, which is visible not only in the intensity images but also in the retardance and orientation. Previous research in porous 3D printed scaffolds has shown that pore size of 400 – 500 μm, as in the implant with small struts, performs the best in terms of integration and tissue regeneration.[182] The tissue formed inside the implant's pores has a higher retardance and a broader distribution of angles relative to the native bone in the surroundings. The tissue covering the surface of the struts can present a higher retardance due to a higher degree of anisotropy of the collagen microfibrils; however, that parameter can also be falsely enhanced by an orientation with a strong component out of the plane of the slice. These two reasons can strongly affect the measured retardance, and complementary measurements using this and other techniques such small-angle X-ray scattering tensor tomography should be used.

In addition to the previous results, higher magnification images were obtained, where the interface between the implant and the bone can be observed with a relatively higher anisotropy than the surrounding bone, as seen in the retardance (i.e., brighter colours in the orientation) (Figure 6.14). Apart from a higher retardance, the regenerated tissue has an orientation with small domains at different angles (Figure 6.14a-f). That is visible in the solid implant and the 3D printed ones, which might indicate the border between the bone defect and the healthy bone where the regeneration process started. The tissue growth on the struts of the porous implants has a structure similar to the individual trabecula in the surroundings (Figure 6.14g-l). The intensity images show the embedded osteons and the layers characteristic of the lamellar bone (Figure 6.14h-i). The combined angle and retardance images show tissue oriented around the trabecular pores, as previously seen in the healthy bone (Figure 6.12b) and literature,[22, 25, 183] indicating a successful bone formation.

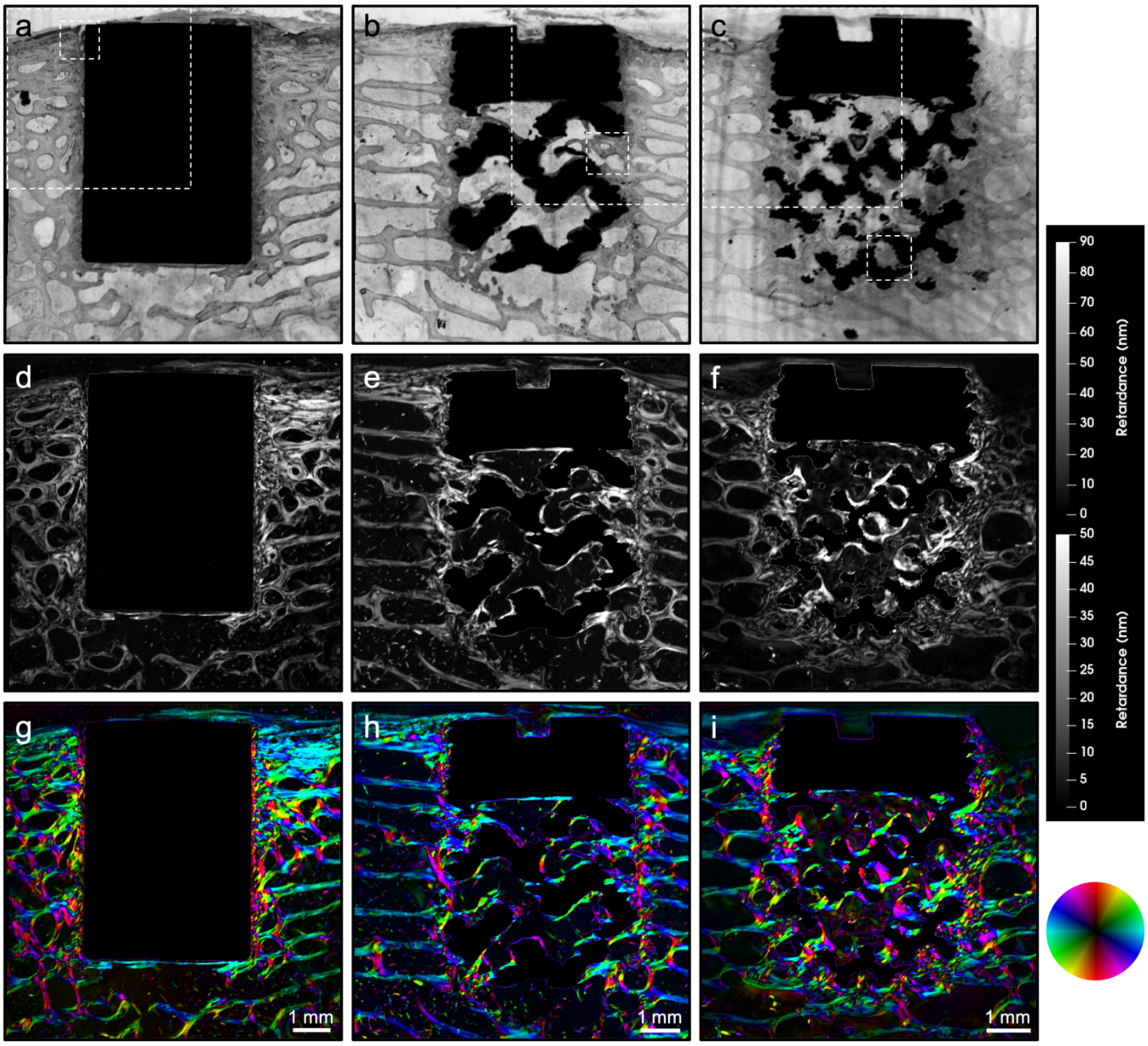

Figure 6.13. Birefringence microscopy of 3D printed metallic implants tested *in vivo* in sheep bone. Three different implant morphologies were used with solid cylinders (**left**), porous with large struts (middle) and porous with small structs (**right**). The images show the intensity (**a**-**c**), retardance (**d**-**f**) with colour scale from 0 – 90 nm for the solid cylinder (**d**) and 0 – 50 nm for the porous implants (**e**-**f**). The angle of the fast axis (**g**-**i**) is plotted with the retardance according to the colour wheel. The hue shows the direction of the optical fast-axis, and the value shows the retardance. Material with high retardance appears with brighter colours. Higher magnification images were obtained in the dashed areas, which are shown in Figure 6.14.

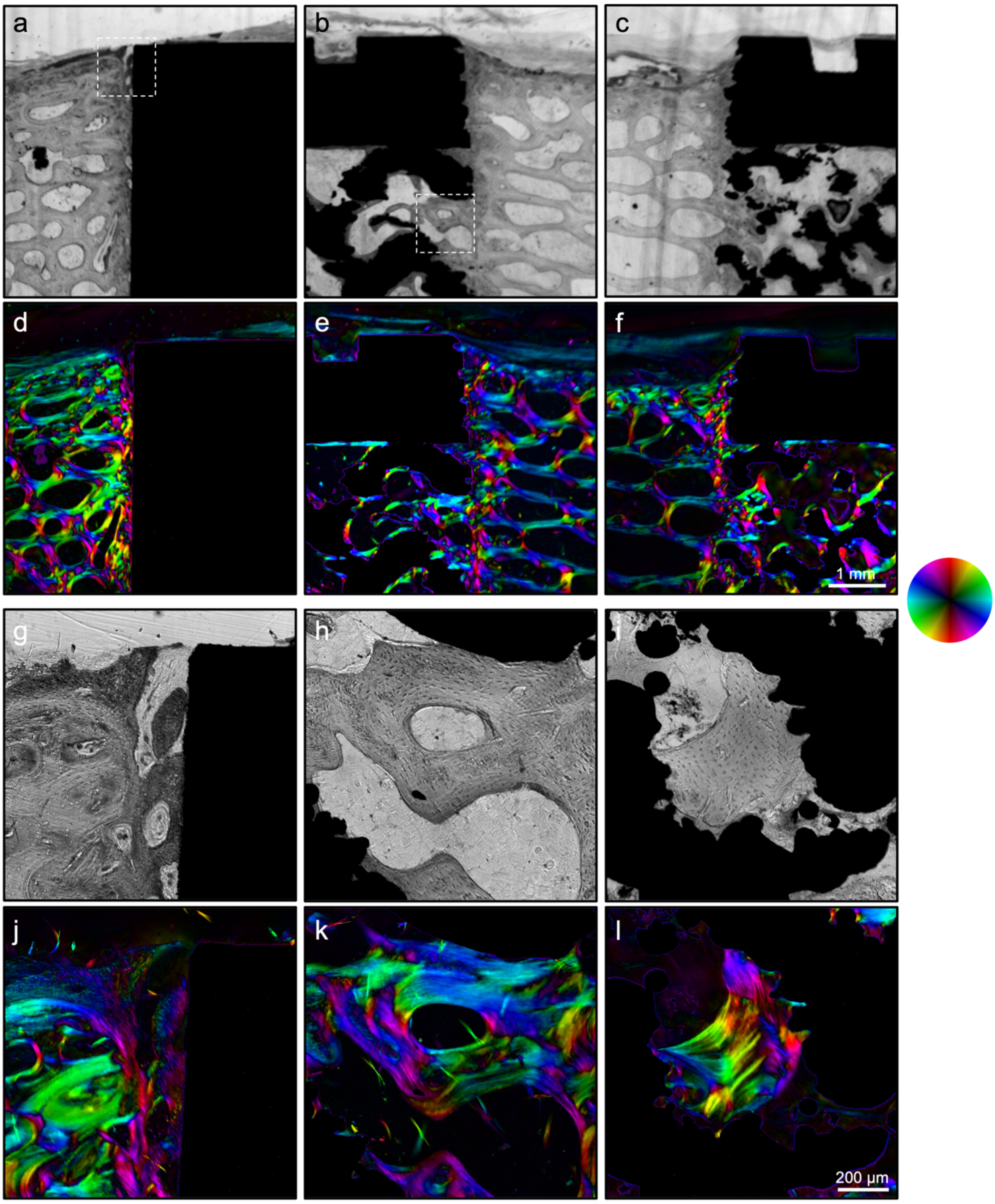

Figure 6.14. Birefringence microscopy of 3D printed metallic implants tested *in vivo* in sheep bone. Higher magnification images of the three implants: solid cylinders (**left**), porous with large struts (middle) and porous with small struts (**right**). The images show the intensity (**a**-**c** and **g**-**i**) and the angle of the fast axis (**d**-**f** and **j**-**l**) at two different magnifications. The angle is plotted with the retardance according to the colour wheel. The hue shows the direction of the optical fast-axis, and the value shows the retardance.

The use of metallic implants or polymeric scaffolds presents several advantages and drawbacks. Compared to the fibrillar scaffolds shown in the previous section, metallic implants often offer better mechanical support. They usually have a higher elastic modulus to resist the load during movement even at an early stage after surgery. The higher stiffness also brings a better interlocking mechanism between bone and implant, which reduces the chances of the implant moving inside the defect.[184] However, metallic alloys have a low degrading rate, and the implant often gets permanently integrated into the bone. Some biodegradable alloys such as magnesium-based implants have been developed,[185] but titanium alloys are still the most commonly used metal in implants.[182] In contrast, the polymeric scaffolds aim not to offer mechanical support to the individual but to the cells, steering the growth of new tissue. They tend to be manufactured in highly biodegradable materials, leaving no trace after months or even weeks and being substituted by new tissue.

6.3. Bioinspired 3D Printed Lyotropic Liquid Crystals

Bioinspired self-assembled lyotropic liquid crystals were studied in this part of the thesis (***Paper I*** and ***II***). This ternary system is based on the tri-block co-polymer poly(ethylene oxide)-poly(propylene oxide)-poly(ethylene oxide) (PEO-PPO-PEO), in which the chain length of each block was either $PEO_{100}PPO_{70}PEO_{100}$ (Pluronic® F-127), labelled as polymer *F*, or $PEO_{20}PPO_{70}PEO_{20}$ (Pluronic® P-123), denoted as polymer *P*. These polymers offer a wide variety of possible phases, as first described by Holmqvist et al.[151] The hexagonal and lamellar structures were selected for this study due to their anisotropy and periodicity in two and one spatial dimensions, respectively.

6.3.1. Self-Assembled Structure of Lyotropic Liquid Crystals

There are multiple analysis strategies to study the nanostructure and anisotropy of the material. The phase of the self-assembled liquid crystal can be identified by the relationship between the diffraction peaks using small-angle X-ray scattering.[151] A representative radial integration of the scattering signal from the SAXS measurements carried out in the microfluidic channels in ***Paper I*** and the *in situ* 3D printing in ***Paper II*** are shown in Figure 6.15. The diffraction peaks prove long-range order, the phase can be deduced by calculating the ratio between the diffraction peak positions. Following the ratio polymer:water:butanol, detailed in Section 5.2, Table 5.1, the liquid crystals produced using polymer *F* with composition 35:50:15 and *P* with 45:55:0 have a peak ratio of $1:\sqrt{3}:2:\sqrt{5}:4$ (Figure 6.15 blue line) which reveals a hexagonal system (H_1). These two materials are therefore labelled as FH_1 and PH_1, respectively. Due to the amphiphilic character of the polymer, it assembles in a cylindric arrangement with the hydrophobic PPO block in the inner part and the hydrophilic PEO block towards the water media (Figure 6.16a). The cylinders are further assembled in a

2-dimensional hexagonal lattice (Figure 6.16b) with cylinder interdistance of 165.4 Å and 151.4 Å for FH_I and PH_I, respectively, as determined from the first diffraction peak.

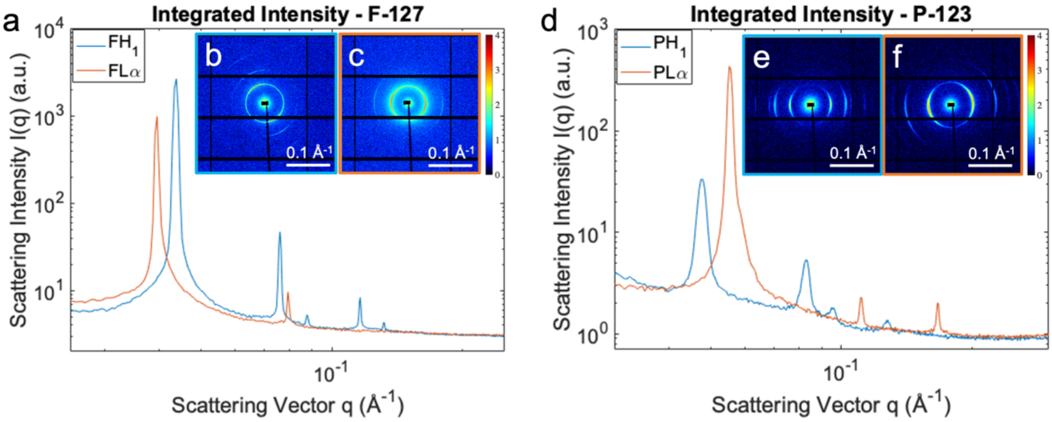

Figure 6.15. Integrated intensity of the SAXS signal from the lyotropic liquid crystals in hexagonal (H_I) and lamellar (L_α) phase for the polymer F-127 (**a**) and P-127 (**d**). The insets show the 2D scattering patterns recorded for the hexagonal (**b**, **e**) and lamellar (**c**, **f**) self-assembled structures.

The lyotropic liquid crystals prepared with the composition 25:47.5:27.5 for polymer *F* and 75:25:0 for polymer *P* have a peak ratio of 1:2:3 (Figure 6.15 red line), characteristic of a lamellar self-assembled structure (L_α). The polymers create bilayers in a lamellar stack with the PEO blocks facing the water media and the PPO block the inner part of the bilayer (Figure 6.16d), which have an order in the nanometre range, but are considered to have infinite lateral dimensions.[153, 186] Those samples were therefore denoted as FL_α and PL_α, which have an interlamellar dimension of 159.5 Å and 113.9 Å, respectively (Figure 6.16e).

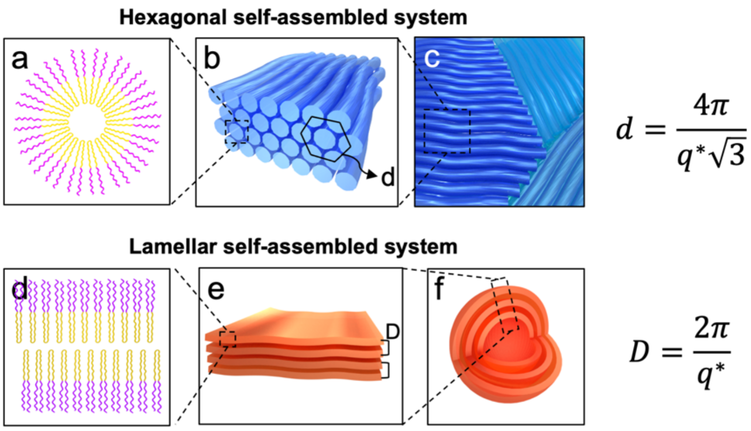

Figure 6.16. Triblock co-polymer in cylindrical cross-section (**a**), self-assembled in in cylindric micelles in a hexagonal lattice (**b**) with cylinder distance *d*. The cylinders can eventually form microdomains with different relative orientations (**c**). The amphiphilic polymer can for bilayers (**d**) as well, may create extended lamellae (**e**) or multilamellar vesicles (**f**), with interlamellar distance *D*. The pink and yellow parts in (**a**) and (**d**) corresponds to the hydrophilic and hydrophobic blocks respectively in the tri-block co-polymer. q^* represents the value of the scattering vector in the first diffraction peak, which corresponds to the crystalline plane (100).

Oscillatory tests of the self-assembled liquid crystals were performed to reveal the rheological behaviour of the hexagonal and lamellar phases. The linear viscoelastic storage (*G'*) and loss (*G''*) moduli (Figure 6.17a-b) were measured in a frequency sweep for a constant strain rate (γ) of 0.01 % within the linear viscoelastic regime. For both hexagonal and lamellar phases, the response is dominated by the elastic component, *G' > G''*. The moduli are independent of the angular frequency and parallel between each other, which is characteristic of a gel-like behaviour with the exception of FL_α, which has a trend to a more fluid-like characteristic with convergent slopes.[187] The rheological response of these materials is dominated by the interaction between the self-assembled structures.[188]

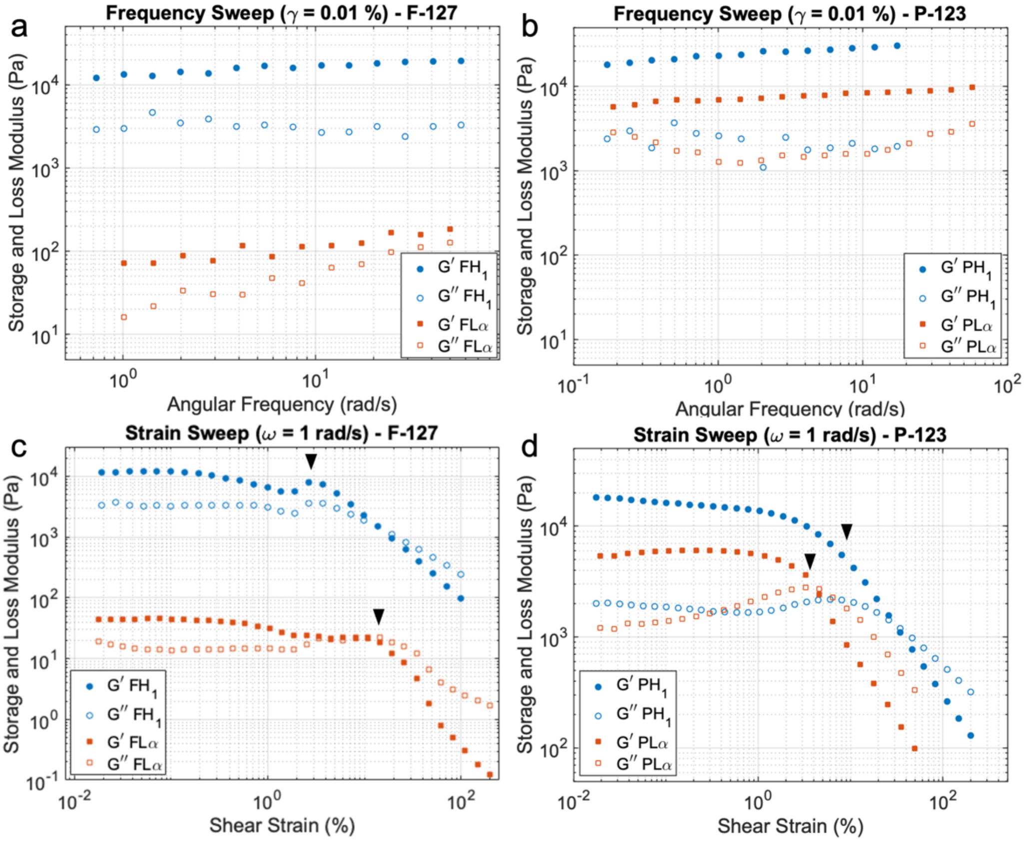

Figure 6.17. Rheology characterization of the liquid crystals measured by oscillatory tests. The storage (*G'*) and loss (*G''*) moduli are represented for the frequency and strain sweeps of the hexagonal and lamellar phases of polymers F-127 (**a**-**b**) and P-123 (**c**-**d**). For an easier comparison, the viscoelastic moduli in the frequency sweep is shown with the same scale. Black arrows indicate the point where strain overshoot can be identified.

Figure 6.17c-d represents the strain sweep of the liquid crystals for an angular frequency (ω) of 1.0 rad/s. Beyond the linear viscoelastic regime, two characteristic behaviours are characterised by an increase in the loss modulus and/or the storage modulus. An increase in both *G'* and *G''*, as seen for FH_1, is known as a strong strain overshoot.[189] It is related with intermolecular interactions between the polar chains in large ordered materials, which could be explained as cluster size growth of hexagonally packed cylinders with a common orientation.[189-191] The movement and reorientation of cylinder aggregates produce an increase in the size of the clusters with a preferential orientation towards the direction of the movement. As a consequence, *G'* and *G''* increase, which for high strain amplitudes when *G''* > *G'*, aggregates tend to break and reorient in the direction of movement. For PH_1, only the loss modulus increases, known as weak strain overshoot. This type of behaviour is characterised by an increase in the loss modulus *G''*, which is produced by a resistance to deformation of the self-assembled structure by the movement of the fluid. After a critical point, the stress is able to deform and realign the structure in the direction of the movement, however in this case cluster break-up is not considered, due to stronger interaction between their building blocks.[192] In the case of the lamellar phases of both polymers, FL_α and PL_α, weak strain overshoot is also observed, with an increase in the loss modulus, related to energy dissipation. For lamellar systems, weak strain overshoot is related to layer-to-layer sliding, caused by shear stress in the fluid.[190, 193] At high shear rates G'' becomes higher than G' during the nanostructure reorganization. From that point on, the viscoelastic moduli decrease, and the material flows more easily.

6.3.2. Anisotropy in Confined Flow[194]

The rheology experiments indicate the effect of shear in the lyotropic liquid crystals. Using microfluidic channels to reproduce the 3D printing nozzles allows for studying more complex flows with shear and extensional contributions. Scanning small-angle X-ray scattering (SAXS) was used to study the structure and anisotropy of the self-assembled systems in the confined space of the microfluidic channels. As described in more detail in Section 5.3 two microchannel designs were used to mimic the most common 3D printing nozzles, conic and blunt. The channels were prepared with the same contraction ratio from 1.25 mm to 100 μm, using a progressive and a sharp contraction. The hexagonal and lamellar phases of the polymer *F* were pumped through at a constant flow rate of 0.03, 0.30 and 3.00 μL/s. During the flow, the channels were scanned by the X-ray beam and the angle of orientation and the Hermans' orientation parameter of the main diffraction peak were obtained.

Figure 6.18a-d show the angle of orientation and the Hermans' orientation parameter of the hexagonal FH_1 liquid crystal in the microfluidic channel at a flow rate of 0.03 μL/s. The scattering intensity of the diffraction peaks was evaluated at the azimuthal angle for each scanning point (i.e., pixel). Some channel regions had two intensity maxima corresponding to the scattering signal of cylindric micelles parallel to the channel plane (Figure 6.18e). The central area of the channel showed a scattering pattern with six maxima in the azimuthal angle (Figure 6.18f). This type of diffraction signal in a hexagonal 2D lattice is expected when the crystalline long-axis is oriented parallel to the beam.[135, 195] Thus, the crystalline domains in these regions are oriented perpendicular to the flow direction. The scattering pattern found in these scan points is not compatible with the orientation quantification by the Hermans' algorithm; therefore, the corresponding pixels were masked out in white. The angle of orientation and orientation parameter is comparable in both channels. They reach an angle in the range of ± 3 degrees with a higher oriented layer in the proximities of the walls. The velocity profile in that area is expected to be lower; however, the shear rate is maximized.

Using a contraction increases the extensional flow in the centre of the channel, which plays an essential role in the alignment of particles in flow. However, the perpendicular orientation found in the central area contradicts the expected orientation. We presume that shear plays a significant role in the alignment and the shear rate is not high enough to orient the liquid crystal in that region.

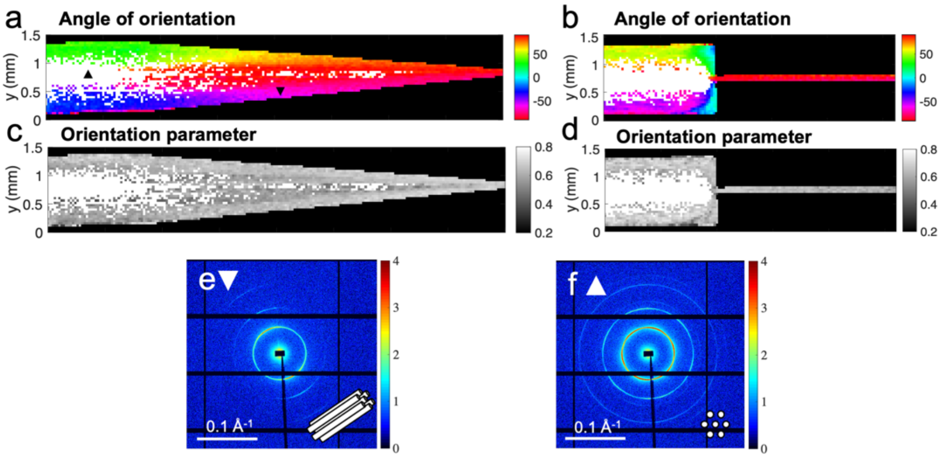

Figure 6.18. Scanning SAXS measurements of the lyotropic liquid crystal in the hexagonal phase (FH_I) in the microfluidic channel with a flow rate of 0.03 μL/s. Flow direction from left to right. Scattering pattern from a pixel where the orientation of the domain is **e**) perpendicular (▼) and **f**) parallel (▲) to the beam. The angle of orientation of the scattering is colour coded according to the colour scale from -90° to 90°.

The orientation in the lamellar phase FL_α occurs already more downstream with a more uniform distribution in the channel area and high alignment values at the channel's entrance, as shown in Figure 6.19a-b. This can be connected to the lower viscosity of the lamellar phase and lower resistance to movement and orientation in the flow direction, as discussed in Section 4.1.2. The orientation parameter in Figure 6.19c-d shows three areas with different values. Area A has a high orientation parameter in the proximities of the walls, which decays to a minimum in area B and then slightly increases in the centre of the channel in area C, as illustrated in Figure 6.19c and 6.19e. The shear rates in the walls are maximum, as explained in the previous case with the hexagonal phase.

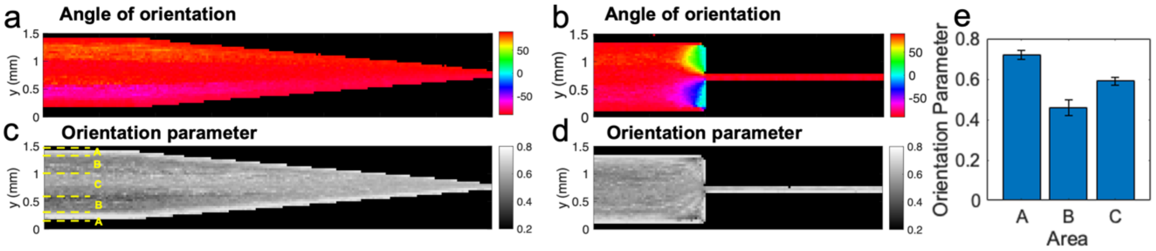

Figure 6.19. Scanning SAXS measurements of the lyotropic liquid crystal in the lamellar phase (FL_α) in the microfluidic channel with a flow rate of 0.03 μL/s. Flow direction from left to right. The angle of orientation of the scattering is colour coded according to the colour scale from -90° to 90°. The areas indicated with the letters A, B and C correspond with the three regions found in the orientation parameter.

In order to investigate the different regions of alignment a more in-depth study of the rheological behaviour of the liquid crystals was done by steady shear measurements. The viscosity dependence of the shear rate is shown in Figure 6.20. FH_I has a uniform viscosity curve with a shear thinning character. In contrast, FL_α has a viscosity curve with three different slopes in the experimental data. In order to relate the measured viscosity and the microfluidic experiments previously shown, the approximate shear rate in the microchannels was calculated using Son's model.[196] It uses the width (W), height (H) and flow rate (Q), and it is applicable to micellar systems[197] in geometries when the velocity is dependent on the lateral dimensions ($W \approx H$). This model calculates the apparent shear rate ($\dot{\gamma}_a$) in Equation 6.1 and the wall shear rate ($\dot{\gamma}_W$) in Equation 6.2, where f^* is a tabulated function dependant on the ratio height/width and n is the power law index (see ***Paper I***). The calculated wall shear rate ($\dot{\gamma}_W$) is found in regime III of the viscosity curve.

$$\dot{\gamma}_a = \left(\frac{6Q}{WH^2}\right)\left(1 + \frac{H}{W}\right) f^* \left(\frac{H}{W}\right) \qquad \text{Equation 6.1}$$

$$\dot{\gamma}_W = \dot{\gamma}_a \left(\frac{2}{3}\right)\left(\frac{b^*}{f^*} + \frac{a^*}{f^*}\frac{1}{n}\right) \qquad \text{Equation 6.2}$$

Figure 6.21 shows the scattering pattern of representative pixels in the three areas of the microchannel. Close to the channel walls, at high shear rates (area A and regime III of the viscosity curve), the diffraction peak associated with the lamella interspace shows a strong anisotropy, which indicates aligned extended lamellae perpendicular to the shear plane in accordance with previous literature.[186] In the intermediate area (area B and regime II), the diffraction peak appears at the same q-value but with an isotropic intensity in contrast to area A. This is an intrinsic feature of vesicular systems, which consist of spherical bilayers with homogeneous wall thickness and low anisotropy. The area C has a scattering pattern with a diffraction peak in the whole azimuthal range, however the intensity is not homogeneous. This scattering pattern is expected from elongated vesicles. The shear rate in the centre of the channel is significantly lower, but the contraction induces a high extensional flow. Thus, vesicles are stretched towards the contraction.

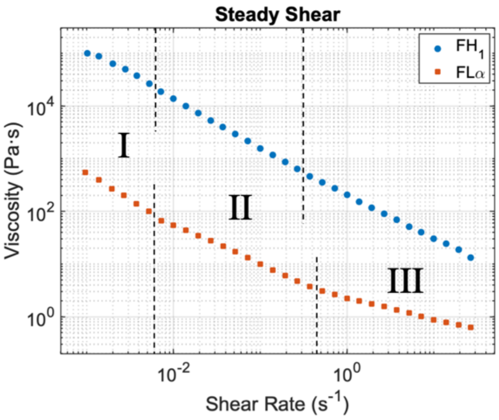

Figure 6.20. Steady shear measurements of the hexagonal and lamellar self-assembled phases. The viscosity dependence of the shear rate is split by the dashed lines in the three different slopes found.

These findings are supported by other studies on co-polymers self-assembled in lamellar structures, which have also shown a viscosity curve with three regimes.[198] At low shear rates (regime I), the structure has a high number of defects, such as dislocations in the lamellas. The viscosity regime I is likely dominated by local re-arrangements in the microstructure without significant conformational alterations. At intermediate shear rates (regime II), the formation of multilamellar vesicles has been discussed, which are broken into extended lamellae at high shear rates.[198] Multilamellar vesicles are likely to be formed due to the movement and wrapping of extended lamellae during the local reorientation, which are stretched due to the flow until they break and form well-ordered lamellae at high shear rates (regime III).

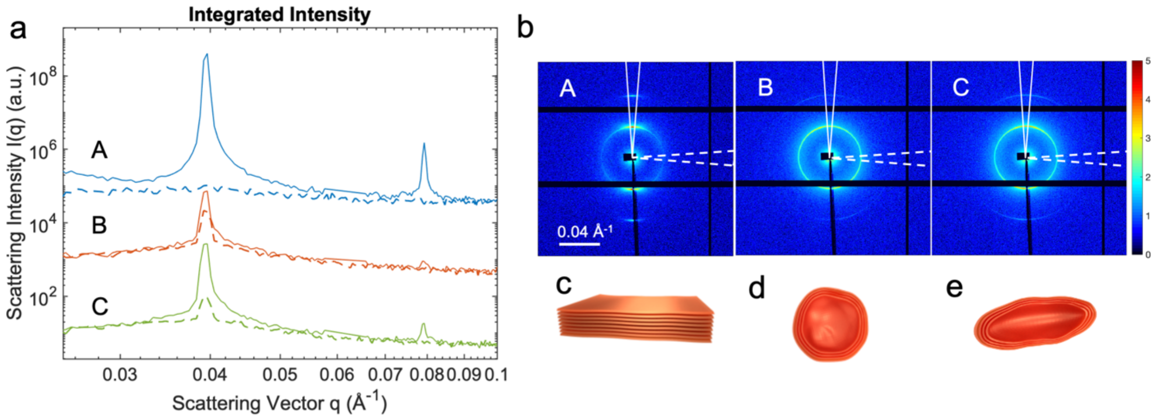

Figure 6.21. a) Integrated intensity in two segments with a difference of 90° plotted in solid and dashed lines. **b**) Scattering pattern of a representative point in the three identified areas in Figure 6.19c. The scattering seen in A corresponds to extended lamellae (**c**), whereas B shows the scattering of multilamellar vesicles (**d**) and C multilamellar vesicles stretched in the flow direction (**e**). The curves have been shifted vertically for better clarity.

6.3.3. *In Situ* 3D Printing and Study of the Induced Anisotropy[199]

After analysing the anisotropy and nanostructure of the materials in confined flow, a further step into open flow conditions is necessary to get a more complete overview of the induction of alignment in 3D printing as well as their evolution after exiting the nozzle. Lyotropic liquid crystals with a high enough viscoelastic modulus are appropriate for 3D printing. The samples FH_1, PH_1 and PL_α were loaded in the 3D printer cartridge and extruded while being scanned *in situ* by the X-ray beam. The results in Figure 6.22 show that the hexagonal structures have a higher orientation parameter when extruded through a larger nozzle diameter (Figure 6.22a-e). The average orientation parameter increased a 30 % for FH_1 and 38 % for PH_1 from the smallest to the largest nozzle, with a maximum mean value of $\langle f_a \rangle^{FH_1} = 0.64 \pm 0.06$ and $\langle f_a \rangle^{PH_1} = 0.61 \pm 0.02$ respectively. The lamellar structure PL_α is, in contrast, not significantly influenced by the nozzle diameter, with a maximum mean value of $\langle f_a \rangle^{PL_\alpha} = 0.50 \pm 0.11$ (Figure 6.22f-h).

The filaments show a core-shell structure with a higher orientation parameter in the outer layer and a low-oriented core. As explained in the previous section, the shear rate in the proximities of the walls is higher than in the middle, which influences the orientation parameter. High viscosity fluids with shear thinning behaviour can create a plug flow with a highly oriented layer that creates a shield effect in the rest of the filament, where the surrounding material pushes the internal core. In cylindrical deposition nozzles, a thin skin layer is followed by a yielded shell that experienced high shear forces. In the core of that filament, an unyielded gel moves at a constant velocity pushed by the flow.[200] This thin skin layer with high orientation is in particular distinct for PH_1 at 460 µm (Figure 6.22d).

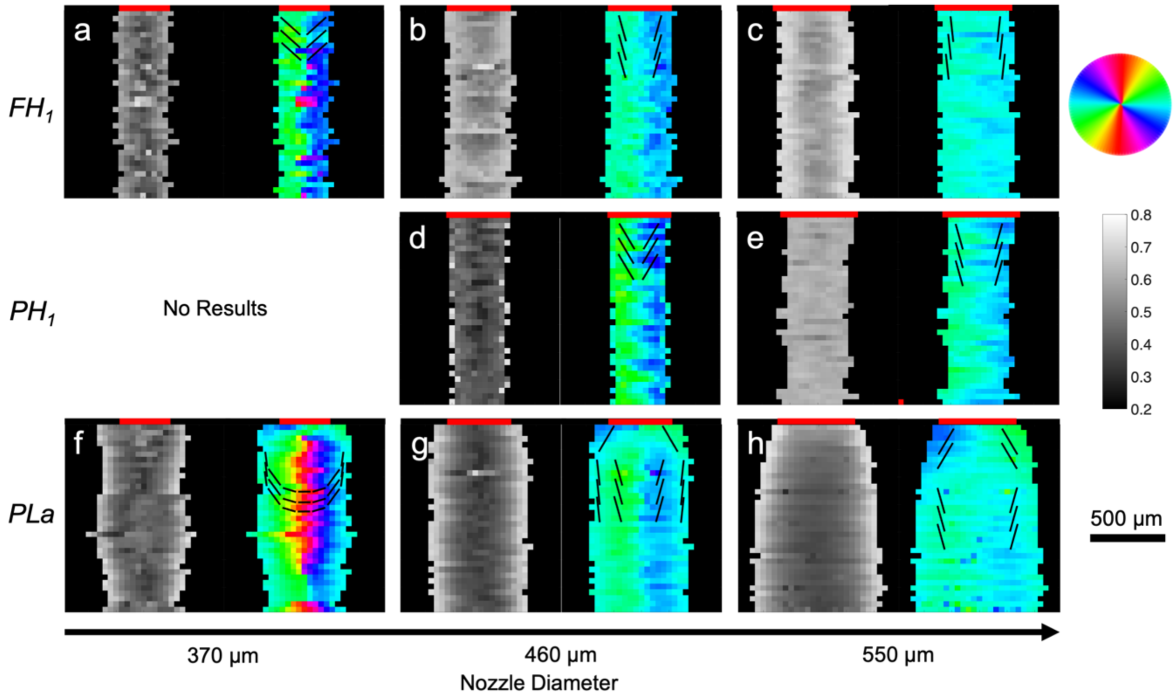

Figure 6.22. Scanning SAXS of *in situ* 3D printed lyotropic liquid crystals. The printed strand was scanned using increasing nozzle diameters (left to right) for the three examined liquid crystals. A row of red pixels represents the internal diameter of each nozzle on the top of the scanning maps. The Hermans' orientation parameter (left side) and angle of orientation (right side) were calculated and colour-coded for a more straightforward interpretation. Black lines indicating the principal direction of alignment in the liquid crystals are added to the angle of orientation plots.

The average angle of orientation of the scattering signal is in the range of ± 5°, which corresponds to the alignment of the hexagonal rods (Figure 6.16a-e) and lamellar sheets (Figure 6.16f-h), respectively, in the direction of extrusion. The variation of the angle of orientation is also strongly correlated with the nozzle diameter. Filaments produced by larger nozzle diameters have a more homogeneous alignment (turquoise) as well as a higher orientation parameter. Smaller nozzles created a distinct pattern of alignment directed diagonally downwards from each side of the wall (blue and green, respectively) in a V-shape for the 460 μm nozzle (Figure 6.22b, d and g) and U-shape for the 370 μm nozzle (Figure 6.22f).

The use of inks which are based on solvents, are susceptible to evaporation during the manufacturing process. The evaporation may change their properties due to the change in the composition, which defines the self-assembled structure of the lyotropic liquid crystals. Birefringence microscopy of the 3D printed filament was carried out to observe possible changes in the anisotropy and macrostructure. This is possible due to the optical anisotropy of the elongated polymeric structures in the liquid crystal.[201] FH_I in Figure 6.23a has an orientation parallel to the printing direction, which agrees with the scanning SAXS experiments shown in Figure 6.22a-c. A filament with low retardance is obtained, which later increases. The evolution of the macroscopic orientation shows the formation of microdomains, starting with a few microdomains and extending to the whole analysed area. The stress induced in the material during extrusion may cause the loss of orientation as a stress release process.[202] PH_I in Figure 6.23b, produced a filament oriented in the printing direction with high anisotropy. The retardance later decreases, presumably by the effect of solvent evaporation and relaxation forces. A few minutes after printing, a new region appears in the outer layer of the filament. From this point on the retardance values decay up to a minimum and the intensity of the birefringence signal is too low to consider the measured angle of the optical fast axis to be reliable. That new appearing structure has a similar birefringence signal to the one observed in the lamellar structure PL_α (Figure 6.23c) with a very low retardance and homogeneous orientation.

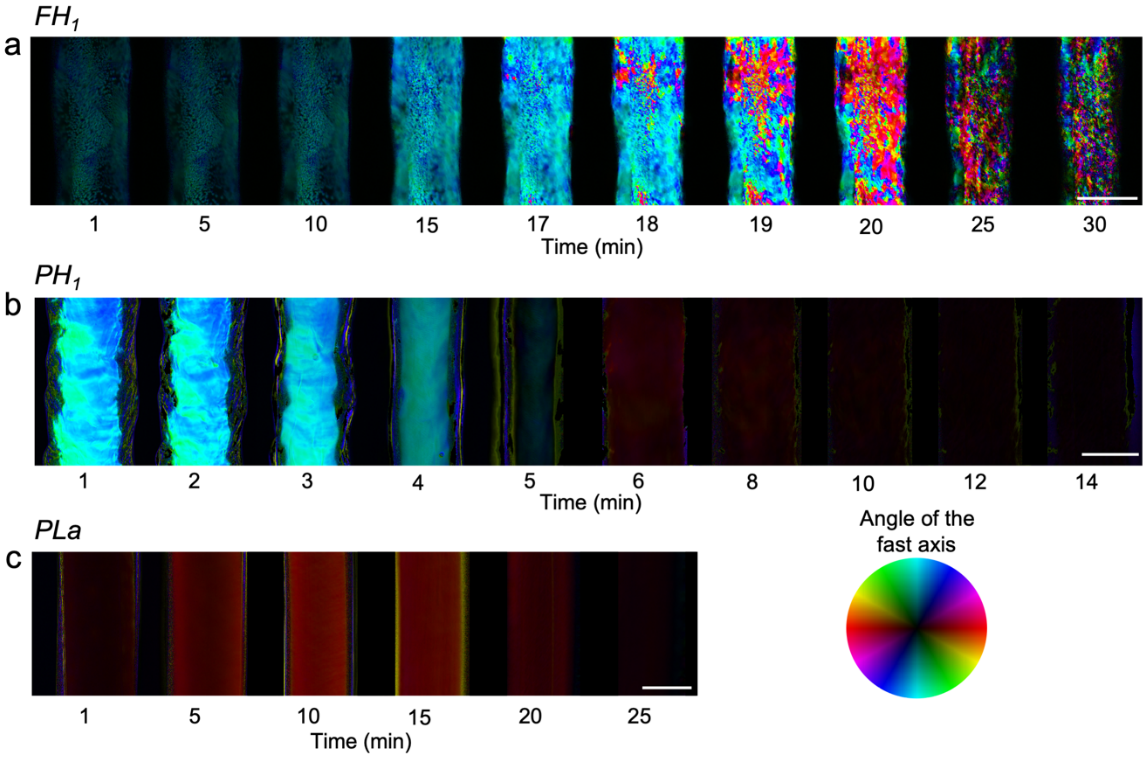

Figure 6.23. Birefringence microscopy of the 3D printed liquid crystal over time with a nozzle of 460 μm diameter. The combined plot with the angle of the optical fast axis is colour-coded according to the colour wheel and the value scaled with the retardance. The filament was 3D printed on the vertical axis and deposited on a glass slide in atmospheric conditions for the measurement. The time points indicated in min, with the most significant changes, were selected to visualize the evolution. The background (glass slide) was masked. The scale bar represents 400 μm.

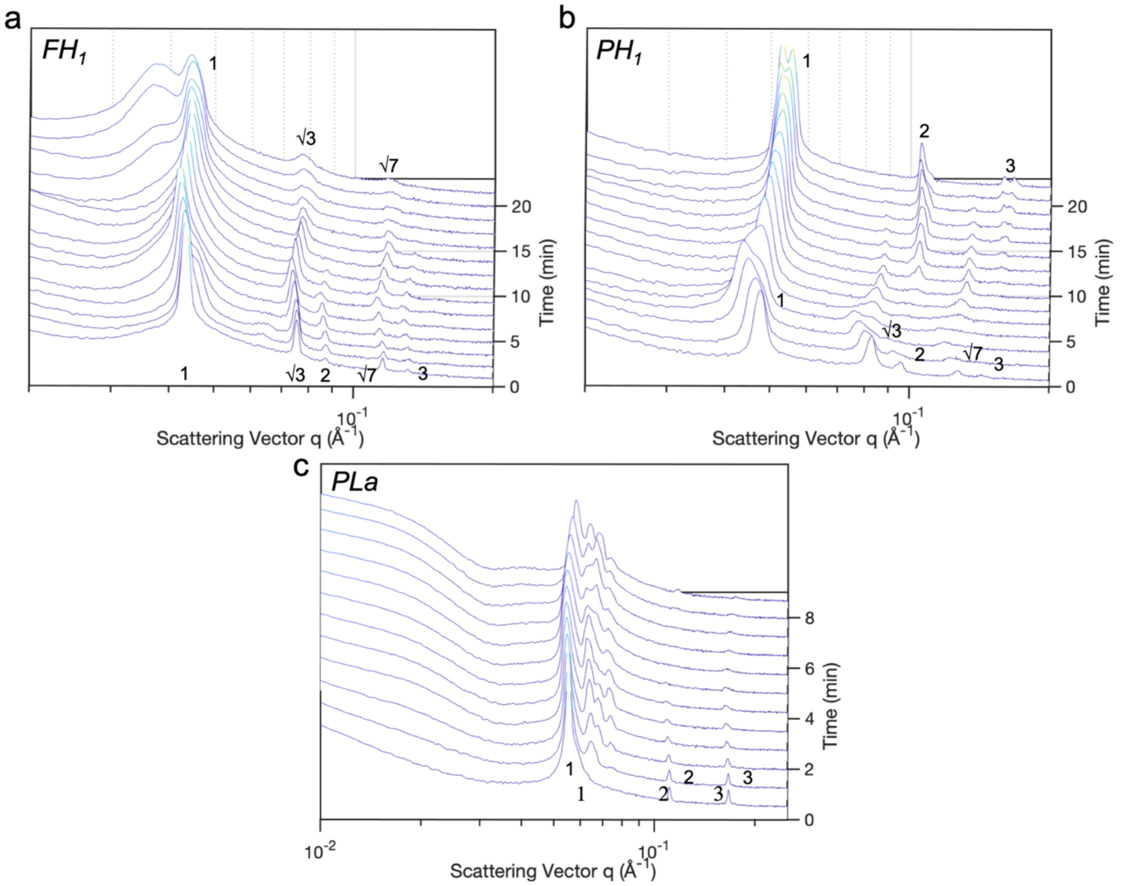

Figure 6.24. Evolution of the azimuthally integrated SAXS signal from 3D printed liquid crystals over time for FH_1 (**a**), PH_1 (**b**) and PL_α (**c**). The extruded filament was scanned in the vertical position and the scattering signal was recorded in each point across the width.

The evolution of the 3D printed filaments was also tracked with SAXS by scanning a single line of the filament over time. For FH_1 in Figure 6.24a the initial peak ratio is 1:√3:2:√7, which as commented before, represents a hexagonal self-assembled structure. The peaks get broader and less pronounced over time, adding a second population at lower q-values with a broader peak at a characteristic distance of 167.41 Å. This finding could be related with the disordered regions in the multidomain structure observed in Figure 6.23a. The time evolution of PH_1 (Figure 6.24b) starts with the characteristic hexagonal peak ratio 1:√3:2√7, which is transformed into the new ratio 1:2:3 from a lamellar phase. Since the experiment was performed in atmospheric conditions, we assume a change of composition due to the loss of solvent by evaporation, resulting in a shift in the phase diagram.[151] This finding supports the results in Figure 6.23c, where the hexagonal structure revealed an abrupt change in the birefringence signal matching the signal obtained in the lamellar phase in Figure 6.23e. The evolution of PL_α in Figure 6.24c shows the initial lamellar peak ratio 1:2:3. The effect of time and evaporation induced a partial phase change with three prominent peaks appearing at low q-values. The indexation of the diffraction peaks could presumably match the reflection of the crystalline planes (200), (210) and (211) as described in a similar system; however, the reflection (110) is not present.[203, 204] Together with the new peaks, a shoulder at low q appears. A fitting with the software SAS View agrees with a form factor from a sphere in cubic arrangement with a radius of 136 Å. This estimation is consistent with previous references and the theoretical sphere radius of a cubic structure of 148 Å. This result suggests the coexistence of two phases, L_α and I_1. The experiments involving extrusion and quick environmental changes are far from thermodynamic stability, which opens the possibility for these processes to occur.

Chapter 7

Conclusions and Outlook

The experiments and results presented in this thesis focused on studying anisotropic hierarchical materials using mainly imaging techniques. Scanning imaging, tensor tomography and full-field microscopy have been the principal techniques in this thesis to image the morphology and nanostructural anisotropy in 2D and 3D. X-rays and polarised light have been combined to produce images with different contrasts towards a better understanding of the materials.

3D SAXS tensor tomography is a time-consuming technique which requires high-end experimental setups and data analysis strategies, but the obtained information is highly valuable. This technique not only provides information about the 3D nanostructure orientation but also resolves the 3D reciprocal space map of each individual volumetric element. Furthermore, destructive sample preparations are also avoided, reducing the risk of slicing artefacts or destroying fragile or valuable samples. One drawback is that the current technology does not allow for measuring a large number of specimens. 2D techniques such as scanning SAXS are established in the field and are experimentally less challenging. They require considerably less measurement time per sample and allow for measuring relatively large numbers of samples with substantially larger fields of view at the same resolution as SAXS tensor tomography. For those reasons, by combining 2D and 3D techniques, it is possible to explore different length scales and fields of view, achieving the best possible balance between resolution, realistic measurement time and a larger number of specimens for better statistics.

Complementing the X-ray techniques, birefringence microscopy has been a very valuable tool for the studies presented in this thesis. Birefringence is one of the oldest techniques to study the ultrastructure orientation indirectly; however, the combination of a full-field imaging setup which allows retrieving quantitative values of the retardance and optical fast-axis with high spatial resolution allows for obtaining high-quality information about the two-dimensional nanostructure and microscale anisotropy of a wide range of materials. The technical requirements of birefringence microscopy make it possible to build instruments that fit in an optical table, accessible in any standard laboratory. The measurement time is extraordinary fast, and the field of view and resolution is only limited by the optical objectives used. So far, this type of birefringence microscopy has not been exploited to the full potential for studying hierarchical materials. The use of this technique should be promoted and expanded as a fast and accessible method to obtain quantitative nanostructural information, which will bring associated new developments in the current experimental capabilities and analysis methods in multiple research fields.

In imaging techniques where direct visualisation of the structure is possible, there is a close connection between the resolution and field of view. Thus, to directly visualise the nanostructure (e.g. with electron microscopy), only a small field of view can be imaged. In contrast, techniques used in this thesis image the nanostructure indirectly by probing their interaction with photons. In that case, the size of the probed nanostructure does not influence the resolution, or the field of view, allowing for investigating the arrangement of the nanostructure in extended macroscopic samples. These techniques are particularly relevant for anisotropic materials, in which the photon-matter interaction results in an anisotropic signal, thus revealing the alignment of the nanostructure. With X-ray scattering structures from a few hundred nanometres down to the Ångström scale can be probed and images with multiple contrasts can be created from the same measurement. However, indirect measurements do not allow for imaging the actual morphology of the structures. In the case of SAXS, the form and size of the nanostructure can be retrieved by fitting a model to the intensity, but it involves model assumptions that could lead to wrong interpretations. While the alignment of the nanostructures can be retrieved model-free, interpreting the underlying ultrastructure still needs some pre-knowledge about the material.

As a hierarchical material from a natural source, narwhal tusk is a fascinating example due to its complexity, unusual shape, and remote origin. As in many other mineralised tissues in mammals, the building blocks of narwhal tusk at the nanoscale are aligned collagen microfibrils, mineralised with hydroxyapatite nanoparticles. The specific distribution of these nanocomponents at the micro and macro scale is what gives the tusk its peculiar mechanical properties. The mineralised collagen fibrils have a strong anisotropy in the tusk longitudinal direction, as visualised in the scattering and birefringence signals in dentine. However, the minor deviations from the central axis create a macroscopic helical structure of mineralised collagen around the pulp chamber. Even though the 3D experiments highlighted these helical patterns, future experiments using high-energy X-rays in larger samples would reveal the spiral in the mineralised collagen structure as well as help to quantify and relate it to other features such as the dentine tubules and ridged patterns in the inner and outer surfaces of the tusk. Further work on this specific dataset will be very relevant for understanding the mineral morphology and its impact on the nanostructure. Important information about the size, shape and specific arrangement of the mineral particles could be obtained by combining the scattering information with high-resolution techniques such as electron microscopies. Alternating layers with high and low G exponents (i.e., rounded and flat/needle shapes, respectively) and gradients in the particle size have been shown in the 2D data, as well as a strong influence of the scattering anisotropy in the models. The architecture of those building blocks is such complex structure can also be used as a source of inspiration for new composites with improved mechanical properties such as the toughness and strength of narwhal tusk.

From an applied point of view, the study of bone regeneration with different scaffold and implant types could be assessed using the imaging techniques mentioned above. Through 2D scanning SAXS and SAXS tensor tomography, the superior behaviour of aligned scaffolds in the regeneration process of critical-size bone defects *in vivo* was verified. The aligned scaffolds showed significant differences in osseointegration and bone regeneration capacity. The newly formed tissue in those scaffolds had a nanostructure resembling the native bone in their surroundings. Using birefringence microscopy, the tissue surrounding the titanium implant surface was studied, confirming a better integration in the implant with small struts. New bone tissue was found in the pores of both implants; however, a higher degree of penetration and a more homogeneous structure were observed on the implant's surface with smaller struts. These techniques offered a unique chance to correlate spatial nanoscale features at relatively long distances in those experiments.

The same techniques previously used were equally valuable for studying bone-inspired synthetic materials. The hierarchical structure of self-assembled lyotropic liquid crystals has been investigated during manufacturing using 2D imaging techniques, microfluidics and *in situ* 3D printing. By doing so, we aimed to characterise the mechanisms that influence the morphology and anisotropy during processing. The induced anisotropy of lyotropic liquid crystals during 3D printing was dominated by the shear rate created by the walls of the printing channels. The strong effect of shear not only influenced the alignment of the self-assembled cylinders or bilayers but also induced heterogeneities such as core-shell structures on a larger scale. The combination of rheology and scanning SAXS revealed a transition from extended lamellae to multilamellar vesicles and the further break-up due to high mechanical stress back into extended structures. A particularly interesting aspect for further studies is a more in-depth analysis of the effect that pure shear and pure extensional flow have on the anisotropy of the liquid crystals. A combination of rheology and SAXS would clarify the actual transitions between self-assembled units as well as establish the thresholds or stability regimes of the desired morphologies. After 3D printing, the nanostructure of the filament was oriented in the printing direction; however, an increased and more homogeneous orientation was achieved using larger nozzles diameters. The time evolution of the self-assembled structure revealed a general trend towards relaxation, and disorder was observed at long exposure times to atmospheric conditions. The effect of solvent evaporation showed phase transitions to different self-assembled structures and the co-existence of multiple phases. The nozzle used for 3D printing has a critical impact on the final alignment of the material, inducing undesired anisotropy, heterogeneous morphologies and nanostructural transitions. Regarding the initial motivation of improving the quality of the bone-mimetic composites, a poor control in the orientation will therefore influence the mechanical properties of the composite, which is one of the targets in its design. Thus, the presented work is potentially helpful for a more accurate design of the processing parameters in the bone-mimetic composites.

Acknowledgements

I would like to thank the Area of Advance Material Science at the Chalmers University of Technology and the Swedish Research Council (VR 2018-041449) for providing the funding necessary to develop this work. I would also like to acknowledge the European Union's Horizon 2020 research and innovation programme (EUSMI) for providing funding for some of the synchrotron experiments, the Kristina Stenborgs Stiftelse and the Wallenberg Wood Science Centre (WWSC) for the financial support of the birefringence microscope. Finally, I want to acknowledge the Swiss Light Source at the Paul Scherrer Institute (Villigen, Switzerland) and the European Synchrotron Radiation Source (Grenoble, France) for the provision of synchrotron radiation beamtime at the beamlines cSAXS and ID13, respectively.

A big thanks to my supervisor Marianne Liebi, who put her trust in me. All the knowledge gained in these four and a half years is unmeasurable. You always offered me opportunities to explore, learn and develop to become an independent researcher. I have had a wonderful time and will always be grateful for that.

To my co-supervisor, Martin Andersson, for all the help I got in the lab and the exciting discussions, and to my examiner, Aleksandar Matic, for taking care of us and creating a very inclusive and welcoming working environment.

A huge thanks to everyone in the Division of Materials Physics, current and former members. Thank you for all the great time we spent together, afterworks, dinners and for taking me under your wing when I was a newcomer. A very special mention to my office mates, to Filippa, my writing mate, for all the mutual support, and to Matt, who indubitably taught me the Queen's English and gave me so many laughs and great moments.

To the Swiss branch of the team, I have had a quick but wonderful time working with all of you. We have had great experiments, discussions and evenings together, and I hope to continue having them in the future.

I would also like to thank all the help and support I received from the external collaborators in Switzerland, Denmark, Greenland, Germany, and Sweden. One cannot always walk alone, and you have been of great help all these years.

Finally, I would like to thank my family, who supported me when I decided to leave my country to pursue a new goal, to my friends back in Madrid, whom I always keep in mind and love to see every now and then, and to all the people in Göteborg, the ones that stayed and the ones that left, they made my life much easier and entertained, and my bank account a bit smaller.

¡GRACIAS!

Bibliography

1. Wegst, U. G. K., Bai, H., Saiz, E., Tomsia, A. P., and Ritchie, R. O., Bioinspired structural materials. *Nature Materials*, 2015. **14**(1): p. 23-36.

2. Yousefi, A.-M., Hoque, M. E., Prasad, R. G. S. V., and Uth, N., Current strategies in multiphasic scaffold design for osteochondral tissue engineering: A review. *Journal of Biomedical Materials Research Part A*, 2015. **103**(7): p. 2460-2481.

3. Stasiak, J., Brubert, J., Serrani, M., Nair, S., de Gaetano, F., Costantino, M. L., and Moggridge, G. D., A bio-inspired microstructure induced by slow injection moulding of cylindrical block copolymers. *Soft Matter*, 2014. **10**(32): p. 6077-6086.

4. He, W.-X., Rajasekharan, A. K., Tehrani-Bagha, A. R., and Andersson, M., Mesoscopically Ordered Bone-Mimetic Nanocomposites. *Advanced Materials*, 2015. **27**(13): p. 2260-2264.

5. Stock, S. R., Stock, M. K., and Almer, J. D., Combined computed tomography and position-resolved X-ray diffraction of an intact Roman-era Egyptian portrait mummy. *Journal of The Royal Society Interface*, 2020. **17**(172): p. 20200686.

6. Liebi, M., Georgiadis, M., Kohlbrecher, J., Holler, M., Raabe, J., Usov, I., Menzel, A., Schneider, P., Bunk, O., and Guizar-Sicairos, M., Small-angle X-ray scattering tensor tomography: model of the three-dimensional reciprocal-space map, reconstruction algorithm and angular sampling requirements. *Acta Crystallographica Section A Foundations and Advances*, 2018. **74**(1): p. 12-24.

7. Hémonnot, C. Y. J.and Köster, S., Imaging of Biological Materials and Cells by X-ray Scattering and Diffraction. *Acs Nano*, 2017. **11**(9): p. 8542-8559.

8. Prosekov, P. A., Nosik, V. L., and Blagov, A. E., Methods of Coherent X-Ray Diffraction Imaging. *Crystallography Reports*, 2021. **66**(6): p. 867-882.

9. Pfeiffer, F., X-ray ptychography. *Nature Photonics*, 2018. **12**(1): p. 9-17.

10. Guizar-Sicairos, M.and Thibault, P., Ptychography: A solution to the phase problem. *Physics Today*, 2021. **74**(9): p. 42-48.

11. Willmott, P., Synchrotron Physics, in An Introduction to Synchrotron Radiation: Techniques and Applications, 2nd Edition. 2019, Wiley.

12. Tavares, P. F., Al-Dmour, E., Andersson, A., Cullinan, F., Jensen, B. N., Olsson, D., Olsson, D. K., Sjostrom, M., Tarawneh, H., Thorin, S., and Vorozhtsov, A., Commissioning and first-year operational results of the MAX IV 3 GeV ring. *J Synchrotron Radiat*, 2018. **25**(Pt 5): p. 1291-1316.

13. Liu, L., Neuenschwander, R. T., and Rodrigues, A. R. D., Synchrotron radiation sources in Brazil. *Philosophical Transactions of the Royal Society A: Mathematical, Physical and Engineering Sciences*, 2019. **377**(2147): p. 20180235.

14. Raimondi, P., ESRF-EBS: The Extremely Brilliant Source Project. *Synchrotron Radiation News*, 2016. **29**(6): p. 8-15.

15. Li, P., Allain, M., Grünewald, T. A., Rommel, M., Campos, A., Carbone, D., and Chamard, V., 4th generation synchrotron source boosts crystalline imaging at the nanoscale. *Light: Science & Applications*, 2022. **11**(1): p. 73.

16. Willmott, P., Beamlines, in An Introduction to Synchrotron Radiation: Techniques and Applications, 2nd Edition. 2019, Wiley.

17. Schnablegger, H.and Singh, Y., The SAXS guide: getting acquainted with the principles. *Austria: Anton Paar GmbH*, 2011: p. 1-124.

18. Bunk, O., Bech, M., Jensen, T. H., Feidenhans'l, R., Binderup, T., Menzel, A., and Pfeiffer, F., Multimodal x-ray scatter imaging. *New Journal of Physics*, 2009. **11**(12).

19. van Gurp, M., The use of rotation matrices in the mathematical description of molecular orientations in polymers. *Colloid and Polymer Science*, 1995. **273**(7): p. 607-625.

20. Yu, J., Tian, F., Chen, S., Wang, X., Zhang, Y., and Wang, H., Structure and property development of aromatic copolysulfonamide fibers during wet spinning process. *Journal of Applied Polymer Science*, 2015. **132**(31).

21. Fratzl, P., Jakob, H. F., Rinnerthaler, S., Roschger, P., and Klaushofer, K., Position-Resolved Small-Angle X-ray Scattering of Complex Biological Materials. *Journal of Applied Crystallography*, 1997. **30**(5-2): p. 765-769.

22. Liebi, M., Georgiadis, M., Menzel, A., Schneider, P., Kohlbrecher, J., Bunk, O., and Guizar-Sicairos, M., Nanostructure surveys of macroscopic specimens by small-angle scattering tensor tomography. *Nature*, 2015. **527**(7578): p. 349-352.

23. Schaff, F., Bech, M., Zaslansky, P., Jud, C., Liebi, M., Guizar-Sicairos, M., and Pfeiffer, F., Six-dimensional real and reciprocal space small-angle X-ray scattering tomography. *Nature*, 2015. **527**(7578): p. 353-356.

24. Malecki, A., Potdevin, G., Biernath, T., Eggl, E., Willer, K., Lasser, T., Maisenbacher, J., Gibmeier, J., Wanner, A., and Pfeiffer, F., X-ray tensor tomography. *EPL (Europhysics Letters)*, 2014. **105**(3): p. 38002.

25. Georgiadis, M., Guizar-Sicairos, M., Zwahlen, A., Trüssel, A. J., Bunk, O., Müller, R., and Schneider, P., 3D scanning SAXS: a novel method for the assessment of bone ultrastructure orientation. *Bone*, 2015. **71**: p. 42-52.

26. Gao, Z., Guizar-Sicairos, M., Lutz-Bueno, V., Schroter, A., Liebi, M., Rudin, M., and Georgiadis, M., High-speed tensor tomography: iterative reconstruction tensor tomography (IRTT) algorithm. *Acta Crystallographica Section A*, 2019. **75**(2).

27. Nielsen, L. C., Erhart, P., Guizar-Sicairos, M., and Liebi, M., Improved small-angle x-ray scattering tensor tomography with unrestricted spherical harmonics. *In preparation*, 2022.

28. Nielsen, L. C., Theoretical and computational advances in small-angle x-ray scattering tensor tomography. *Licentiate thesis*, Chalmers University of Technology, Gothenburg, Sweden, 2022.

29. Willmott, P., The Interaction of X-rays with Matter, in An Introduction to Synchrotron Radiation: Techniques and Applications, 2nd Edition. 2019, Wiley.

30. Majumdar, S., Peralta-Videa, J. R., Castillo-Michel, H., Hong, J., Rico, C. M., and Gardea-Torresdey, J. L., Applications of synchrotron µ-XRF to study the distribution of biologically important elements in different environmental matrices: A review. *Analytica Chimica Acta*, 2012. **755**: p. 1-16.

31. Scholze, F., Longoni, A., Fiorini, C., Strüder, L., Meidinger, N., Hartmann, R., Kawahara, N., and Shoji, T., X-Ray Detectors and XRF Detection Channels, in Handbook of Practical X-Ray Fluorescence Analysis, Beckhoff, B., Kanngießer, h. B., Langhoff, N., Wedell, R., and Wolff, H., Editors. 2006, Springer Berlin Heidelberg: Berlin, Heidelberg. p. 199-308.

32. Collett, E., The Stokes Polarization Parameters, in Field Guide to Polarization. 2005, SPIE. p. 12-13.

33. Goldstein, D. H., Polarized Light. 3rd Edition ed. 2011: CRC Press.

34. Collett, E., The Mueller Matrices for Polarizing Components, in Field Guide to Polarization. 2005, SPIE. p. 17-17.

35. John, F., Andy, L., Jacob, W., Baoliang, W., and Solomon, S. A photoelastic modulator-based birefringence imaging microscope for measuring biological specimens. in Proc.SPIE. 2014.

36. Shane, N., John, F., Oriol, A., and Bart, K. Imaging with photoelastic modulators. in Proc.SPIE. 2014.

37. Han, C.-Y.and Chao, Y.-F., Photoelastic modulated imaging ellipsometry by stroboscopic illumination technique. *Review of Scientific Instruments*, 2006. **77**(2): p. 023107.

38. Haward, S. J., Toda-Peters, K., and Shen, A. Q., Steady viscoelastic flow around high-aspect-ratio, low-blockage-ratio microfluidic cylinders. *Journal of Non-Newtonian Fluid Mechanics*, 2018. **254**: p. 23-35.

39. Walther, J., Li, Q., Villiger, M., Farah, C. S., Koch, E., Karnowski, K., and Sampson, D. D., Depth-resolved birefringence imaging of collagen fiber organization in the human oral mucosa in vivo. *Biomedical Optics Express*, 2019. **10**(4): p. 1942-1956.

40. Wang, J., Dong, L., Chen, H., and Huang, S., Birefringence measurement of biological tissue based on polarization-sensitive digital holographic microscopy. *Applied Physics B*, 2018. **124**(12): p. 240.

41. Cardiel, J. J., Furusho, H., Skoglund, U., and Shen, A. Q., Formation of crystal-like structures and branched networks from nonionic spherical micelles. *Scientific Reports*, 2015. **5**(1): p. 17941.

42. Cardiel, J. J., Zhao, Y., De La Iglesia, P., Pozzo, L. D., and Shen, A. Q., Turning up the heat on wormlike micelles with a hydrotopic salt in microfluidics. *Soft Matter*, 2014. **10**(46): p. 9300-9312.

43. Schwieger, W., Machoke, A. G., Weissenberger, T., Inayat, A., Selvam, T., Klumpp, M., and Inayat, A., Hierarchy concepts: classification and preparation strategies for zeolite containing materials with hierarchical porosity. *Chemical Society Reviews*, 2016. **45**(12): p. 3353-3376.

44. Fratzl, P.and Weinkamer, R., Nature's hierarchical materials. *Progress in Materials Science*, 2007. **52**(8): p. 1263-1334.

45. Brodoceanu, D., Bauer, C. T., Kroner, E., Arzt, E., and Kraus, T., Hierarchical bioinspired adhesive surfaces—a review. *Bioinspiration & Biomimetics*, 2016. **11**(5): p. 051001.

46. Nudelman, F., Nacre biomineralisation: A review on the mechanisms of crystal nucleation. *Seminars in Cell & Developmental Biology*, 2015. **46**: p. 2-10.

47. Feng, Q. L., Cui, F. Z., Pu, G., Wang, R. Z., and Li, H. D., Crystal orientation, toughening mechanisms and a mimic of nacre. *Materials Science and Engineering: C*, 2000. **11**(1): p. 19-25.

48. Sun, J.and Bhushan, B., Hierarchical structure and mechanical properties of nacre: a review. *RSC Advances*, 2012. **2**(20): p. 7617-7632.

49. Gao, H., Wang, X., Yao, H., Gorb, S., and Arzt, E., Mechanics of hierarchical adhesion structures of geckos. *Mechanics of Materials*, 2005. **37**(2): p. 275-285.

50. Georgiadis, M., Müller, R., and Schneider, P., Techniques to assess bone ultrastructure organization: orientation and arrangement of mineralized collagen fibrils. *Journal of The Royal Society Interface*, 2016. **13**(119): p. 20160088.

51. Mao, L.-B., Gao, H.-L., Yao, H.-B., Liu, L., Cölfen, H., Liu, G., Chen, S.-M., Li, S.-K., Yan, Y.-X., Liu, Y.-Y., and Yu, S.-H., Synthetic nacre by predesigned matrix-directed mineralization. *Science*, 2016. **354**(6308): p. 107.

52. Renteria, C., Fernández-Arteaga, J. M., Grimm, J., Ossa, E. A., and Arola, D., Mammalian enamel: A universal tissue and diverse source of inspiration. *Acta Biomaterialia*, 2021. **136**: p. 402-411.

53. Petruska John, A.and Hodge Alan, J., A Subunit Model for the Tropocollagen Macromolecule. *Proceedings of the National Academy of Sciences*, 1964. **51**(5): p. 871-876.

54. Ottani, V., Martini, D., Franchi, M., Ruggeri, A., and Raspanti, M., Hierarchical structures in fibrillar collagens. *Micron*, 2002. **33**(7): p. 587-596.

55. Stock, S. R., The Mineral–Collagen Interface in Bone. *Calcified Tissue International*, 2015. **97**(3): p. 262-280.

56. Landis, W. J.and Jacquet, R., Association of Calcium and Phosphate Ions with Collagen in the Mineralization of Vertebrate Tissues. *Calcified Tissue International*, 2013. **93**(4): p. 329-337.

57. Reznikov, N., Bilton, M., Lari, L., Stevens Molly, M., and Kröger, R., Fractal-like hierarchical organization of bone begins at the nanoscale. *Science*, 2018. **360**(6388): p. eaao2189.

58. Reznikov, N., Chase, H., Brumfeld, V., Shahar, R., and Weiner, S., The 3D structure of the collagen fibril network in human trabecular bone: Relation to trabecular organization. *Bone*, 2015. **71**: p. 189-195.

59. Jaschouz, D., Paris, O., Roschger, P., Hwang, H.-S., and Fratzl, P., Pole figure analysis of mineral nanoparticle orientation in individual trabecula of human vertebral bone. *Journal of Applied Crystallography*, 2003. **36**(3): p. 494-498.

60. Lee, B. E. J., Langelier, B., and Grandfield, K., Visualization of Collagen–Mineral Arrangement using Atom Probe Tomography. *bioRxiv*, 2020: p. 2020.07.10.197673.

61. Nudelman, F., Pieterse, K., George, A., Bomans, P. H., Friedrich, H., Brylka, L. J., Hilbers, P. A., de With, G., and Sommerdijk, N. A., The role of collagen in bone apatite formation in the presence of hydroxyapatite nucleation inhibitors. *Nat Mater*, 2010. **9**(12): p. 1004-9.

62. Reznikov, N., Shahar, R., and Weiner, S., Bone hierarchical structure in three dimensions. *Acta Biomaterialia*, 2014. **10**(9): p. 3815-3826.

63. Pawelec, K. M., Introduction to the challenges of bone repair, in Bone Repair Biomaterials (Second Edition), Pawelec, K. M. and Planell, J. A., Editors. 2019, Woodhead Publishing. p. 1-13.

64. Ghorbani, F., Li, D., Zhong, Z., Sahranavard, M., Qian, Z., Ni, S., Zhang, Z., Zamanian, A., and Yu, B., Bioprinting a cell-laden matrix for bone regeneration: A focused review. *Journal of Applied Polymer Science*, 2021. **138**(8): p. 49888.

65. Jonas, P., Nina, K. W., Maja, Ø., Alexander, B. J., and Henrik, B. The osteocyte lacuno-canalicular network in bone investigated by synchrotron radiation-based techniques. in Proc.SPIE. 2019.

66. Fuchs, R. K., Thompson, W. R., and Warden, S. J., Bone biology, in Bone Repair Biomaterials (Second Edition), Pawelec, K. M. and Planell, J. A., Editors. 2019, Woodhead Publishing. p. 15-52.

67. Semprebon, G. M., Tao, D., Hasjanova, J., and Solounias, N., An examination of the dietary habits of Platybelodon grangeri from the Linxia Basin of China: Evidence from dental microwear of molar teeth and tusks. *Palaeogeography, Palaeoclimatology, Palaeoecology*, 2016. **457**: p. 109-116.

68. Su, X. W.and Cui, F. Z., Hierarchical structure of ivory: from nanometer to centimeter. *Materials Science and Engineering: C*, 1999. **7**(1): p. 19-29.

69. Albéric, M., Dean, M. N., Gourrier, A., Wagermaier, W., Dunlop, J. W. C., Staude, A., Fratzl, P., and Reiche, I., Relation between the Macroscopic Pattern of Elephant Ivory and Its Three-Dimensional Micro-Tubular Network. *Plos One*, 2017. **12**(1): p. e0166671.

70. Free, R., DeRocher, K., Xu, R., Joester, D., and Stock, S. R., A method for mapping submicron-scale crystallographic order/disorder applied to human tooth enamel. *Powder Diffraction*, 2020. **35**(2): p. 117-123.

71. Märten, A., Fratzl, P., Paris, O., and Zaslansky, P., On the mineral in collagen of human crown dentine. *Biomaterials*, 2010. **31**(20): p. 5479-5490.

72. Thompson, V. P., The tooth: An analogue for biomimetic materials design and processing. *Dental Materials*, 2020. **36**(1): p. 25-42.

73. Stifler, C. A., Wittig, N. K., Sassi, M., Sun, C.-Y., Marcus, M. A., Birkedal, H., Beniash, E., Rosso, K. M., and Gilbert, P. U. P. A., X-ray Linear Dichroism in Apatite. *Journal of the American Chemical Society*, 2018. **140**(37): p. 11698-11704.

74. Wang, C., Li, Y., Wang, X., Zhang, L., Tiantang, and Fu, B., The Enamel Microstructures of Bovine Mandibular Incisors. *The Anatomical Record*, 2012. **295**(10): p. 1698-1706.

75. Sui, T., Sandholzer, M. A., Baimpas, N., Dolbnya, I. P., Walmsley, A., Lumley, P. J., Landini, G., and Korsunsky, A. M., Multiscale modelling and diffraction-based characterization of elastic behaviour of human dentine. *Acta Biomaterialia*, 2013. **9**(8): p. 7937-7947.

76. Seyedkavoosi, S.and Sevostianov, I., Micromechanics of Dentin: Review. *Reviews on advanced materials and technologies*, 2019. **1**: p. 1-26.

77. Kinney, J. H., Pople, J. A., Marshall, G. W., and Marshall, S. J., Collagen Orientation and Crystallite Size in Human Dentin: A Small Angle X-ray Scattering Study. *Calcified Tissue International*, 2001. **69**(1): p. 31-37.

78. Bertassoni, L. E., Dentin on the nanoscale: Hierarchical organization, mechanical behavior and bioinspired engineering. *Dental Materials*, 2017. **33**(6): p. 637-649.

79. Shahmoradi, M., Bertassoni, L. E., Elfallah, H. M., and Swain, M., Fundamental Structure and Properties of Enamel, Dentin and Cementum, in Advances in Calcium Phosphate Biomaterials, Ben-Nissan, B., Editor. 2014, Springer Berlin Heidelberg: Berlin, Heidelberg. p. 511-547.

80. Ho, S. P., Balooch, M., Goodis, H. E., Marshall, G. W., and Marshall, S. J., Ultrastructure and nanomechanical properties of cementum dentin junction. *Journal of Biomedical Materials Research Part A*, 2004. **68A**(2): p. 343-351.

81. Heide-Jørgensen, M. P., Narwhal: Monodon monoceros, in Encyclopedia of Marine Mammals (Third Edition), Würsig, B., Thewissen, J. G. M., and Kovacs, K. M., Editors. 2018, Academic Press. p. 627-631.

82. Garde, E.and Heide-Jørgensen, M. P., Tusk anomalies in narwhals (Monodon monoceros) from Greenland. *Polar Research*, 2022. **41**.

83. Currey, J. D., Brear, K., and Zioupos, P., Dependence of mechanical properties on fibre angle in narwhal tusk, a highly oriented biological composite. *Journal of Biomechanics*, 1994. **27**(7): p. 885-897.

84. Nweeia, M. T., Eichmiller, F. C., Hauschka, P. V., Tyler, E., Mead, J. G., Potter, C. W., Angnatsiak, D. P., Richard, P. R., Orr, J. R., and Black, S. R., Vestigial Tooth Anatomy and Tusk Nomenclature for Monodon Monoceros. *The Anatomical Record*, 2012. **295**(6): p. 1006-1016.

85. Nweeia, M. T., Eichmiller, F. C., Hauschka, P. V., Donahue, G. A., Orr, J. R., Ferguson, S. H., Watt, C. A., Mead, J. G., Potter, C. W., Dietz, R., Giuseppetti, A. A., Black, S. R., Trachtenberg, A. J., and Kuo, W. P., Sensory ability in the narwhal tooth organ system. *The Anatomical Record*, 2014. **297**(4): p. 599-617.

86. Graham, Z. A., Garde, E., Heide-Jørgensen, M. P., and Palaoro, A. V., The longer the better: evidence that narwhal tusks are sexually selected. *Biology letters*, 2020. **16**(3): p. 20190950-20190950.

87. Break, K., Currey, J. D., Pond, C. M., and Ramsay, M. A., The mechanical properties of the dentine and cement of the tusk of the narwhal Monodon monoceros compared with those of other mineralized tissues. *Archives of Oral Biology*, 1990. **35**(8): p. 615-621.

88. Fratzl, P., Groschner, M., Vogl, G., Plenk Jr, H., Eschberger, J., Fratzl-Zelman, N., Koller, K., and Klaushofer, K., Mineral crystals in calcified tissues: A comparative study by SAXS. *Journal of Bone and Mineral Research*, 1992. **7**(3): p. 329-334.

89. Fratzl, P., Fratzl-Zelman, N., and Klaushofer, K., Collagen packing and mineralization. An x-ray scattering investigation of turkey leg tendon. *Biophysical Journal*, 1993. **64**(1): p. 260-266.

90. Seidel, R., Gourrier, A., Kerschnitzki, M., Burghammer, M., Fratzl, P., Gupta, H. S., and Wagermaier, W., Synchrotron 3D SAXS analysis of bone nanostructure. *Bioinspired, Biomimetic and Nanobiomaterials*, 2012. **1**(2): p. 123-131.

91. Weiner, S.and Traub, W., Bone structure: from ångstroms to microns. *The FASEB Journal*, 1992. **6**(3): p. 879-885.

92. Fratzl, P., Schreiber, S., and Klaushofer, K., Bone Mineralization as Studied by Small-Angle X-Ray Scattering. *Connective Tissue Research*, 1996. **34**(4): p. 247-254.

93. Fratzl, P., Fratzl-Zelman, N., Klaushofer, K., Vogl, G., and Koller, K., Nucleation and growth of mineral crystals in bone studied by small-angle X-ray scattering. *Calcified Tissue International*, 1991. **48**(6): p. 407-413.

94. Fratzl, P., Groschner, M., Vogl, G., Plenk, H., Jr., Eschberger, J., Fratzl-Zelman, N., Koller, K., and Klaushofer, K., Mineral crystals in calcified tissues: a comparative study by SAXS. *J Bone Miner Res*, 1992. **7**(3): p. 329-34.

95. Liebi, M., Lutz-Bueno, V., Guizar-Sicairos, M., Schonbauer, B. M., Eichler, J., Martinelli, E., Loffler, J. F., Weinberg, A., Lichtenegger, H., and Grunewald, T. A., 3D nanoscale

analysis of bone healing around degrading Mg implants evaluated by X-ray scattering tensor tomography. *Acta Biomater*, 2021.

96. Fratzl, P., Gupta, H. S., Paris, O., Valenta, A., Roschger, P., and Klaushofer, K., Diffracting "stacks of cards" - some thoughts about small-angle scattering from bone, in Scattering Methods and the Properties of Polymer Materials, Stribeck, N. and Smarsly, B., Editors. 2005, Springer Berlin Heidelberg: Berlin, Heidelberg. p. 33-39.

97. Gourrier, A., Li, C., Siegel, S., Paris, O., Roschger, P., Klaushofer, K., and Fratzl, P., Scanning small-angle X-ray scattering analysis of the size and organization of the mineral nanoparticles in fluorotic bone using a stack of cards model. *Journal of Applied Crystallography*, 2010. **43**(6): p. 1385-1392.

98. Zizak, I., Roschger, P., Paris, O., Misof, B. M., Berzlanovich, A., Bernstorff, S., Amenitsch, H., Klaushofer, K., and Fratzl, P., Characteristics of mineral particles in the human bone/cartilage interface. *Journal of Structural Biology*, 2003. **141**(3): p. 208-217.

99. Bünger, M. H., Oxlund, H., Hansen, T. K., Sørensen, S., Bibby, B. M., Thomsen, J. S., Langdahl, B. L., Besenbacher, F., Pedersen, J. S., and Birkedal, H., Strontium and Bone Nanostructure in Normal and Ovariectomized Rats Investigated by Scanning Small-Angle X-Ray Scattering. *Calcified Tissue International*, 2010. **86**(4): p. 294-306.

100. Rieppo, J., Hallikainen, J., Jurvelin, J. S., Kiviranta, I., Helminen, H. J., and Hyttinen, M. M., Practical considerations in the use of polarized light microscopy in the analysis of the collagen network in articular cartilage. *Microsc Res Tech*, 2008. **71**(4): p. 279-87.

101. Mark van, T., Sander, K., and Johan van, L., Modeling optical behavior of birefringent biological tissues for evaluation of quantitative polarized light microscopy. *Journal of Biomedical Optics*, 2009. **14**(5): p. 1-11.

102. Gosselin, R. A., Conway, D. J., Phillips, J. J., and Coughlin, R. R., Diseases of the Musculoskeletal System, in Hunter's Tropical Medicine and Emerging Infectious Diseases (Tenth Edition), Ryan, E. T., Hill, D. R., Solomon, T., Aronson, N. E., and Endy, T. P., Editors. 2020, Elsevier: London. p. 114-119.

103. Wu, A.-M., Bisignano, C., James, S. L., Abady, G. G., Abedi, A., Abu-Gharbieh, E., Alhassan, R. K., Alipour, V., Arabloo, J., Asaad, M., Asmare, W. N., Awedew, A. F., Banach, M., Banerjee, S. K., Bijani, A., Birhanu, T. T. M., Bolla, S. R., Cámera, L. A., Chang, J.-C., Cho, D. Y., et al., Global, regional, and national burden of bone fractures in 204 countries and territories, 1990–2019: a systematic analysis from the Global Burden of Disease Study 2019. *The Lancet Healthy Longevity*, 2021. **2**(9): p. e580-e592.

104. Zhang, W.and Yelick, P. C., Tooth Repair and Regeneration: Potential of Dental Stem Cells. *Trends in Molecular Medicine*, 2021. **27**(5): p. 501-511.

105. Wang, Z., Wang, Y., Yan, J., Zhang, K., Lin, F., Xiang, L., Deng, L., Guan, Z., Cui, W., and Zhang, H., Pharmaceutical electrospinning and 3D printing scaffold design for bone regeneration. *Advanced Drug Delivery Reviews*, 2021. **174**: p. 504-534.

106. Hsu, E. L.and Stock, S. R., Growth Factors, Carrier Materials, and Bone Repair, in Bone Regulators and Osteoporosis Therapy, Stern, P. H., Editor. 2020, Springer International Publishing: Cham. p. 121-156.

107. Pountos, I.and Giannoudis, P. V., Fracture Healing: Back to Basics and Latest Advances, in Fracture Reduction and Fixation Techniques: Upper Extremities, Giannoudis, P. V., Editor. 2018, Springer International Publishing: Cham. p. 3-17.

108. Huang, E. E., Zhang, N., Shen, H., Li, X., Maruyama, M., Utsunomiya, T., Gao, Q., Guzman, R. A., and Goodman, S. B., Novel Techniques and Future Perspective for Investigating Critical-Size Bone Defects. *Bioengineering*, 2022. **9**(4).

109. Quinnan, S. M.and Lawrie, C., Optimizing Bone Defect Reconstruction—Balanced Cable Transport With Circular External Fixation. *Journal of Orthopaedic Trauma*, 2017. **31**(10).

110. Kroto, H. W., Heath, J. R., O'Brien, S. C., Curl, R. F., and Smalley, R. E., C60: Buckminsterfullerene. *Nature*, 1985. **318**(6042): p. 162-163.

111. Iijima, S., Helical microtubules of graphitic carbon. *Nature*, 1991. **354**(6348): p. 56-58.

112. Eigler, D. M.and Schweizer, E. K., Positioning single atoms with a scanning tunnelling microscope. *Nature*, 1990. **344**(6266): p. 524-526.

113. Zeng, S., Yong, K.-T., Roy, I., Dinh, X.-Q., Yu, X., and Luan, F., A Review on Functionalized Gold Nanoparticles for Biosensing Applications. *Plasmonics*, 2011. **6**(3): p. 491.

114. Jariwala, D., Sangwan, V. K., Lauhon, L. J., Marks, T. J., and Hersam, M. C., Carbon nanomaterials for electronics, optoelectronics, photovoltaics, and sensing. *Chemical Society Reviews*, 2013. **42**(7): p. 2824-2860.

115. Teleanu, D. M., Chircov, C., Grumezescu, A. M., Volceanov, A., and Teleanu, R. I., Contrast Agents Delivery: An Up-to-Date Review of Nanodiagnostics in Neuroimaging. *Nanomaterials*, 2019. **9**(4).

116. Song, W., Musetti, S. N., and Huang, L., Nanomaterials for cancer immunotherapy. *Biomaterials*, 2017. **148**: p. 16-30.

117. Meyers, M. A., McKittrick, J., and Chen, P.-Y., Structural Biological Materials: Critical Mechanics-Materials Connections. *Science*, 2013. **339**(6121): p. 773.

118. Wang, Y., Naleway, S. E., and Wang, B., Biological and bioinspired materials: Structure leading to functional and mechanical performance. *Bioactive Materials*, 2020. **5**(4): p. 745-757.

119. Zhou, J., Zhang, Z., Joseph, J., Zhang, X., Ferdows, B. E., Patel, D. N., Chen, W., Banfi, G., Molinaro, R., Cosco, D., Kong, N., Joshi, N., Farokhzad, O. C., Corbo, C., and Tao, W., Biomaterials and nanomedicine for bone regeneration: Progress and future prospects. *Exploration*, 2021. **1**(2).

120. Groninger, O., Hess, S., Mohn, D., Schneider, E., Stark, W., Marsmann, S., Wolint, P., Calcagni, M., Cinelli, P., and Buschmann, J., Directing Stem Cell Commitment by

Amorphous Calcium Phosphate Nanoparticles Incorporated in PLGA: Relevance of the Free Calcium Ion Concentration. *Int J Mol Sci*, 2020. **21**(7).

121.Vasita, R.and Katti, D. S., Nanofibers and their applications in tissue engineering. *Int J Nanomedicine*, 2006. **1**(1): p. 15-30.

122.Li, W. J., Laurencin, C. T., Caterson, E. J., Tuan, R. S., and Ko, F. K., Electrospun nanofibrous structure: a novel scaffold for tissue engineering. *J Biomed Mater Res*, 2002. **60**(4): p. 613-21.

123.Jeong, J., Kim, J. H., Shim, J. H., Hwang, N. S., and Heo, C. Y., Bioactive calcium phosphate materials and applications in bone regeneration. *Biomater Res*, 2019. **23**: p. 4.

124.Samavedi, S., Whittington, A. R., and Goldstein, A. S., Calcium phosphate ceramics in bone tissue engineering: a review of properties and their influence on cell behavior. *Acta Biomater*, 2013. **9**(9): p. 8037-45.

125.Thibault, R. A., Mikos, A. G., and Kasper, F. K., Scaffold/Extracellular matrix hybrid constructs for bone-tissue engineering. *Adv Healthc Mater*, 2013. **2**(1): p. 13-24.

126.Liu, Y., Luo, D., and Wang, T., Hierarchical Structures of Bone and Bioinspired Bone Tissue Engineering. *Small*, 2016. **12**(34): p. 4611-4632.

127.Giacomelli, C.and Borsali, R., Disordered Phase and Self-Organization of Block Copolymer Systems, in Soft Matter Characterization, Borsali, R. and Pecora, R., Editors. 2008, Springer Netherlands: Dordrecht. p. 133-189.

128.Jones, R. A. L., Jones, R. A. L., and R Jones, P., Soft Condensed Matter. Oxford Master Series in Physics. 2002, Great Britain: OUP Oxford. 195.

129.Israelachvili, J. N., Thermodynamic Principles of Self-Assembly, in Intermolecular and Surface Forces (Third Edition), Israelachvili, J. N., Editor. 2011, Academic Press: San Diego. p. 503-534.

130.Tanford, C., Thermodynamics of Micelle Formation: Prediction of Micelle Size and Size Distribution. *Proceedings of the National Academy of Sciences*, 1974. **71**(5): p. 1811.

131.Bates, F. S.and Fredrickson, G. H., Block Copolymer Thermodynamics: Theory and Experiment. *Annual Review of Physical Chemistry*, 1990. **41**(1): p. 525-557.

132.Imran, M., Shah, M. R., and Shafiullah, Chapter 10 - Amphiphilic block copolymers–based micelles for drug delivery, in Design and Development of New Nanocarriers, Grumezescu, A. M., Editor. 2018, William Andrew Publishing. p. 365-400.

133.Feng, H., Lu, X., Wang, W., Kang, N.-G., and Mays, J. W., Block Copolymers: Synthesis, Self-Assembly, and Applications. *Polymers*, 2017. **9**(10).

134.Kim, J. H., Jin, H. M., Yang, G. G., Han, K. H., Yun, T., Shin, J. Y., Jeong, S.-J., and Kim, S. O., Smart Nanostructured Materials based on Self-Assembly of Block Copolymers. *Advanced Functional Materials*, 2020. **30**(2): p. 1902049.

135.Lim, S.-H., Lee, T., Oh, Y., Narayanan, T., Sung, B. J., and Choi, S.-M., Hierarchically self-assembled hexagonal honeycomb and kagome superlattices of binary 1D colloids. *Nature Communications*, 2017. **8**(1): p. 360.

136.Ha, J.-M., Lim, S.-H., Dey, J., Lee, S.-J., Lee, M.-J., Kang, S.-H., Jin, K. S., and Choi, S.-M., Micelle-Assisted Formation of Nanoparticle Superlattices and Thermally Reversible Symmetry Transitions. *Nano Letters*, 2019. **19**(4): p. 2313-2321.

137.Allen, S. M.and Thomas, E. L., Liquid-Crystalline State, in The Structure of Materials. 1999, Wiley. p. 213-248.

138.Li, L.-s., Walda, J., Manna, L., and Alivisatos, A. P., Semiconductor Nanorod Liquid Crystals. *Nano Letters*, 2002. **2**(6): p. 557-560.

139.Pomerantz, W. C., Yuwono, V. M., Pizzey, C. L., Hartgerink, J. D., Abbott, N. L., and Gellman, S. H., Nanofibers and Lyotropic Liquid Crystals from a Class of Self-Assembling β-Peptides. *Angewandte Chemie International Edition*, 2008. **47**(7): p. 1241-1244.

140.Baruchel, J., Hodeau, J. L., Lehmann, M. S., Regnard, J. R., and Schlenker, C., Structure of Liquid Crystals, in Neutron and Synchrotron Radiation for Condensed Matter Studies: Applications to Soft Condensed Matter and Biology. 1994, Springer-Verlag: Berlin. p. 332.

141.Truby, R. L.and Lewis, J. A., Printing soft matter in three dimensions. *Nature*, 2016. **540**(7633): p. 371-378.

142.Mosher, C. Z., Brudnicki, P. A. P., Gong, Z., Childs, H. R., Lee, S. W., Antrobus, R. M., Fang, E. C., Schiros, T. N., and Lu, H. H., Green electrospinning for biomaterials and biofabrication. *Biofabrication*, 2021. **13**(3): p. 035049.

143.Ding, J., Zhang, J., Li, J., Li, D., Xiao, C., Xiao, H., Yang, H., Zhuang, X., and Chen, X., Electrospun polymer biomaterials. *Progress in Polymer Science*, 2019. **90**: p. 1-34.

144.Robinson, A. J., Pérez-Nava, A., Ali, S. C., González-Campos, J. B., Holloway, J. L., and Cosgriff-Hernandez, E. M., Comparative analysis of fiber alignment methods in electrospinning. *Matter*, 2021. **4**(3): p. 821-844.

145.Wakuda, Y., Nishimoto, S., Suye, S.-i., and Fujita, S., Native collagen hydrogel nanofibres with anisotropic structure using core-shell electrospinning. *Scientific Reports*, 2018. **8**(1): p. 6248.

146.Patel, B. B., Walsh, D. J., Kim, D. H., Kwok, J., Lee, B., Guironnet, D., and Diao, Y., Tunable structural color of bottlebrush block copolymers through direct-write 3D printing from solution. *Science Advances*, 2020. **6**(24): p. eaaz7202.

147.Rajasekharan, A. K., Lotsari, A., Lutz-Bueno, V., Liebi, M., and Andersson, M., Bioinspired Structural Hierarchy within Macroscopic Volumes of Synthetic Composites. *Advanced Healthcare Materials*, 2018. **7**(18).

148.Palmquist, A., Snis, A., Emanuelsson, L., Browne, M., and Thomsen, P., Long-term biocompatibility and osseointegration of electron beam melted, free-form–fabricated solid and porous titanium alloy: Experimental studies in sheep. *Journal of Biomaterials Applications*, 2011. **27**(8): p. 1003-1016.

149.Shah, F. A., Omar, O., Suska, F., Snis, A., Matic, A., Emanuelsson, L., Norlindh, B., Lausmaa, J., Thomsen, P., and Palmquist, A., Long-term osseointegration of 3D printed CoCr constructs with an interconnected open-pore architecture prepared by electron beam melting. *Acta Biomaterialia*, 2016. **36**: p. 296-309.

150.Holler, M., Ihli, J., Tsai, E. H. R., Nudelman, F., Verezhak, M., van de Berg, W. D. J., and Shahmoradian, S. H., A lathe system for micrometre-sized cylindrical sample preparation at room and cryogenic temperatures. *J Synchrotron Radiat*, 2020. **27**(Pt 2): p. 472-476.

151.Holmqvist, P., Alexandridis, P., and Lindman, B., Modification of the Microstructure in Block Copolymer−Water−"Oil" Systems by Varying the Copolymer Composition and the "Oil" Type: Small-Angle X-ray Scattering and Deuterium-NMR Investigation. *The Journal of Physical Chemistry B*, 1998. **102**(7): p. 1149-1158.

152.Holmqvist, P., Alexandridis, P., and Lindman, B., Phase Behavior and Structure of Ternary Amphiphilic Block Copolymer−Alkanol−Water Systems: Comparison of Poly(ethylene oxide)/Poly(propylene oxide) to Poly(ethylene oxide)/Poly(tetrahydrofuran) Copolymers. *Langmuir*, 1997. **13**(9): p. 2471-2479.

153.Holmqvist, P., Alexandridis, P., and Lindman, B., Modification of the Microstructure in Poloxamer Block Copolymer−Water−"Oil" Systems by Varying the "Oil" Type. *Macromolecules*, 1997. **30**(22): p. 6788-6797.

154.Ivanova, R., Lindman, B., and Alexandridis, P., Evolution in Structural Polymorphism of Pluronic F127 Poly(ethylene oxide)−Poly(propylene oxide) Block Copolymer in Ternary Systems with Water and Pharmaceutically Acceptable Organic Solvents: From "Glycols" to "Oils". *Langmuir*, 2000. **16**(23): p. 9058-9069.

155.Alexandridis, P., Olsson, U., and Lindman, B., Self-Assembly of Amphiphilic Block Copolymers: The (EO)13(PO)30(EO)13-Water-p-Xylene System. *Macromolecules*, 1995. **28**(23): p. 7700-7710.

156.Lutz-Bueno, V., Zhao, J., Mezzenga, R., Pfohl, T., Fischer, P., and Liebi, M., Scanning-SAXS of microfluidic flows: nanostructural mapping of soft matter. *Lab on a Chip*, 2016. **16**(20): p. 4028-4035.

157.Barnes, H. A., Hutton, J. F., and Walters, K., An Introduction to Rheology, in An Introduction to Rheology, Walters, K., Editor. 1989, Elsevier.

158.Malvern-Instruments, A Basic Introduction to Rheology. 2016.

159.Schroer, C. G., Kuhlmann, M., Roth, S. V., Gehrke, R., Stribeck, N., Almendarez-Camarillo, A., and Lengeler, B., Mapping the local nanostructure inside a specimen by tomographic small-angle x-ray scattering. *Applied Physics Letters*, 2006. **88**(16): p. 164102.

160.Kraft, P., Bergamaschi, A., Broennimann, C., Dinapoli, R., Eikenberry, E. F., Henrich, B., Johnson, I., Mozzanica, A., Schleputz, C. M., Willmott, P. R., and Schmitt, B., Performance of single-photon-counting PILATUS detector modules. *J Synchrotron Radiat*, 2009. **16**(Pt 3): p. 368-75.

161. Henrich, B., Bergamaschi, A., Broennimann, C., Dinapoli, R., Eikenberry, E. F., Johnson, I., Kobas, M., Kraft, P., Mozzanica, A., and Schmitt, B., PILATUS: A single photon counting pixel detector for X-ray applications. *Nuclear Instruments and Methods in Physics Research Section A: Accelerators, Spectrometers, Detectors and Associated Equipment*, 2009. **607**(1): p. 247-249.

162. CXS group, P. S. I., Switzerland, Scanning SAXS Software Package. https://www.psi.ch/en/sls/csaxs/software.

163. Georgiadis, M., Schroeter, A., Gao, Z., Guizar-Sicairos, M., Liebi, M., Leuze, C., McNab, J. A., Balolia, A., Veraart, J., Ades-Aron, B., Kim, S., Shepherd, T., Lee, C. H., Walczak, P., Chodankar, S., DiGiacomo, P., David, G., Augath, M., Zerbi, V., Sommer, S., et al., Nanostructure-specific X-ray tomography reveals myelin levels, integrity and axon orientations in mouse and human nervous tissue. *Nature Communications*, 2021. **12**(1).

164. Odstrčil, M., Holler, M., Raabe, J., and Guizar-Sicairos, M., Alignment methods for nanotomography with deep subpixel accuracy. *Optics Express*, 2019. **27**(25): p. 36637-36652.

165. Solé, V. A., Papillon, E., Cotte, M., Walter, P., and Susini, J., A multiplatform code for the analysis of energy-dispersive X-ray fluorescence spectra. *Spectrochimica Acta Part B: Atomic Spectroscopy*, 2007. **62**(1): p. 63-68.

166. Goh, K. L., Hiller, J., Haston, J. L., Holmes, D. F., Kadler, K. E., Murdoch, A., Meakin, J. R., and Wess, T. J., Analysis of collagen fibril diameter distribution in connective tissues using small-angle X-ray scattering. *Biochimica et Biophysica Acta (BBA) - General Subjects*, 2005. **1722**(2): p. 183-188.

167. Buchanan, J. K., Zhang, Y., Holmes, G., Covington, A. D., and Prabakar, S., Role of X-ray Scattering Techniques in Understanding the Collagen Structure of Leather. *ChemistrySelect*, 2019. **4**(48): p. 14091-14102.

168. Locke, M., Structure of ivory. *Journal of Morphology*, 2008. **269**(4): p. 423-450.

169. Albéric, M., Gourrier, A., Müller, K., Zizak, I., Wagermaier, W., Fratzl, P., and Reiche, I., Early diagenesis of elephant tusk in marine environment. *Palaeogeography, Palaeoclimatology, Palaeoecology*, 2014. **416**: p. 120-132.

170. Giraud-Guille, M.-M.and Besseau, L., Banded Patterns in Liquid Crystalline Phases of Type I Collagen: Relationship with Crimp Morphology in Connective Tissue Architecture. *Connective Tissue Research*, 1998. **37**(3-4): p. 183-193.

171. Albéric, M., Gourrier, A., Wagermaier, W., Fratzl, P., and Reiche, I., The three-dimensional arrangement of the mineralized collagen fibers in elephant ivory and its relation to mechanical and optical properties. *Acta Biomaterialia*, 2018. **72**: p. 342-351.

172. Grandfield, K., Chattah, N. L.-T., Djomehri, S., Eidelmann, N., Eichmiller, F. C., Webb, S., Schuck, P. J., Nweeia, M., and Ho, S. P., The narwhal (Monodon monoceros) cementum–dentin junction: A functionally graded biointerphase. *Proceedings of the Institution of Mechanical Engineers, Part H: Journal of Engineering in Medicine*, 2014. **228**(8): p. 754-767.

173.Hoerth, R. M., Seidt, B. M., Shah, M., Schwarz, C., Willie, B. M., Duda, G. N., Fratzl, P., and Wagermaier, W., Mechanical and structural properties of bone in non-critical and critical healing in rat. *Acta Biomaterialia*, 2014. **10**(9): p. 4009-4019.

174.Vincent, J., 15 Microscopic Aspects of Mineral Metabolism In Bone Tissue With Special Reference to Calcium, Lead and Zinc. *Clinical Orthopaedics and Related Research®*, 1963. **26**.

175.Dietz, R., Desforges, J.-P., Rigét, F. F., Aubail, A., Garde, E., Ambus, P., Drimmie, R., Heide-Jørgensen, M. P., and Sonne, C., Analysis of narwhal tusks reveals lifelong feeding ecology and mercury exposure. *Current Biology*, 2021. **31**(9): p. 2012-2019.e2.

176.Stock, S. R., Finney, L. A., Telser, A., Maxey, E., Vogt, S., and Okasinski, J. S., Cementum structure in Beluga whale teeth. *Acta Biomaterialia*, 2017. **48**: p. 289-299.

177.Wittig, N. K., Palle, J., Østergaard, M., Frølich, S., Birkbak, M. E., Spiers, K. M., Garrevoet, J., and Birkedal, H., Bone Biomineral Properties Vary across Human Osteonal Bone. *Acs Nano*, 2019. **13**(11): p. 12949-12956.

178.Konig, M. A., Canepa, D. D., Cadosch, D., Casanova, E., Heinzelmann, M., Rittirsch, D., Plecko, M., Hemmi, S., Simmen, H. P., Cinelli, P., and Wanner, G. A., Direct transplantation of native pericytes from adipose tissue: A new perspective to stimulate healing in critical size bone defects. *Cytotherapy*, 2016. **18**(1): p. 41-52.

179.Liebi, M., Lutz-Bueno, V., Guizar-Sicairos, M., Schönbauer, B. M., Eichler, J., Martinelli, E., Löffler, J. F., Weinberg, A., Lichtenegger, H., and Grünewald, T. A., 3D nanoscale analysis of bone healing around degrading Mg implants evaluated by X-ray scattering tensor tomography. *Acta Biomaterialia*, 2021.

180.Xi, L., Zhang, Y., Gupta, H., Terrill, N., Wang, P., Zhao, T., and Fang, D., A multiscale study of structural and compositional changes in a natural nanocomposite: Osteoporotic bone with chronic endogenous steroid excess. *Bone*, 2021. **143**: p. 115666.

181.Hoerth, R. M., Kerschnitzki, M., Aido, M., Schmidt, I., Burghammer, M., Duda, G. N., Fratzl, P., Willie, B. M., and Wagermaier, W., Correlations between nanostructure and micromechanical properties of healing bone. *J Mech Behav Biomed Mater*, 2018. **77**: p. 258-266.

182.Deering, J.and Grandfield, K., Current interpretations on the in vivo response of bone to additively manufactured metallic porous scaffolds: A review. *Biomaterials and Biosystems*, 2021. **2**: p. 100013.

183.Rinnerthaler, S., Roschger, P., Jakob, H. F., Nader, A., Klaushofer, K., and Fratzl, P., Scanning Small Angle X-ray Scattering Analysis of Human Bone Sections. *Calcified Tissue International*, 1999. **64**(5): p. 422-429.

184.Chua, K., Khan, I., Malhotra, R., and Zhu, D., Additive manufacturing and 3D printing of metallic biomaterials. *Engineered Regeneration*, 2021. **2**: p. 288-299.

185.Shuai, C., Li, S., Peng, S., Feng, P., Lai, Y., and Gao, C., Biodegradable metallic bone implants. *Materials Chemistry Frontiers*, 2019. **3**(4): p. 544-562.

186.Winey, K. I., Patel, S. S., Larson, R. G., and Watanabe, H., Interdependence of shear deformations and block copolymer morphology. *Macromolecules*, 1993. **26**(10): p. 2542-2549.

187.Winter, H. H.and Chambon, F., Analysis of Linear Viscoelasticity of a Crosslinking Polymer at the Gel Point. *Journal of Rheology*, 1986. **30**(2): p. 367-382.

188.Kádár, R., Fazilati, M., and Nypelö, T., Unexpected microphase transitions in flow towards nematic order of cellulose nanocrystals. *Cellulose*, 2020. **27**(4): p. 2003-2014.

189.Hyun, K., Wilhelm, M., Klein, C. O., Cho, K. S., Nam, J. G., Ahn, K. H., Lee, S. J., Ewoldt, R. H., and McKinley, G. H., A review of nonlinear oscillatory shear tests: Analysis and application of large amplitude oscillatory shear (LAOS). *Progress in Polymer Science*, 2011. **36**(12): p. 1697-1753.

190.Hyun, K., Nam, J. G., Wilhellm, M., Ahn, K. H., and Lee, S. J., Large amplitude oscillatory shear behavior of PEO-PPO-PEO triblock copolymer solutions. *Rheologica Acta*, 2006. **45**(3): p. 239-249.

191.Richtering, W. Investigation of shear-induced structures in lyotropic mesophases by scattering experiments. in Optical Methods and Physics of Colloidal Dispersions. 1997. Darmstadt: Steinkopff.

192.Hyun, K., Kim, S. H., Ahn, K. H., and Lee, S. J., Large amplitude oscillatory shear as a way to classify the complex fluids. *Journal of Non-Newtonian Fluid Mechanics*, 2002. **107**(1): p. 51-65.

193.Li, X., Park, E.-k., Hyun, K., Oktavia, L., and Kwak, M., Rheological analysis of core-stabilized Pluronic F127 by semi-interpenetrating network (sIPN) in aqueous solution. *Journal of Rheology*, 2017. **62**(1): p. 107-120.

194.Rodriguez-Palomo, A., Lutz-Bueno, V., Cao, X., Kádár, R., Andersson, M., and Liebi, M., In Situ Visualization of the Structural Evolution and Alignment of Lyotropic Liquid Crystals in Confined Flow. *Small*, 2021. **17**: p. 2006229.

195.Trebbin, M., Steinhauser, D., Perlich, J., Buffet, A., Roth, S. V., Zimmermann, W., Thiele, J., and Förster, S., Anisotropic particles align perpendicular to the flow direction in narrow microchannels. *Proceedings of the National Academy of Sciences*, 2013. **110**(17): p. 6706.

196.Son, Y., Determination of shear viscosity and shear rate from pressure drop and flow rate relationship in a rectangular channel. *Polymer*, 2007. **48**(2): p. 632-637.

197.Martin, H. P., Brooks, N. J., Seddon, J. M., Luckham, P. F., Terrill, N. J., Kowalski, A. J., and Cabral, J. T., Microfluidic processing of concentrated surfactant mixtures: online SAXS, microscopy and rheology. *Soft Matter*, 2016. **12**(6): p. 1750-1758.

198.Diat, O., Roux, D., and Nallet, F., Effect of shear on a lyotropic lamellar phase. *J. Phys. II France*, 1993. **3**(9): p. 1427-1452.

199.Rodriguez-Palomo, A., Lutz-Bueno, V., Guizar-Sicairos, M., Kádár, R., Andersson, M., and Liebi, M., Nanostructure and anisotropy of 3D printed lyotropic liquid crystals studied by scattering and birefringence imaging. *Additive Manufacturing*, 2021: p. 102289.

200. Lewis, J. A., Direct Ink Writing of 3D Functional Materials. *Advanced Functional Materials*, 2006. **16**(17): p. 2193-2204.

201. Cardiel, J. J., Takagi, D., Tsai, H.-F., and Shen, A. Q., Formation and flow behavior of micellar membranes in a T-shaped microchannel. *Soft Matter*, 2016. **12**(39): p. 8226-8234.

202. Emmermacher, J., Spura, D., Cziommer, J., Kilian, D., Wollborn, T., Fritsching, U., Steingroewer, J., Walther, T., Gelinsky, M., and Lode, A., Engineering considerations on extrusion-based bioprinting: interactions of material behavior, mechanical forces and cells in the printing needle. *Biofabrication*, 2020. **12**(2): p. 025022.

203. Svensson, B., Alexandridis, P., and Olsson, U., Self-Assembly of a Poly(ethylene oxide)/Poly(propylene oxide) Block Copolymer (Pluronic P104, (EO)27(PO)61(EO)27) in the Presence of Water and Xylene. *The Journal of Physical Chemistry B*, 1998. **102**(39): p. 7541-7548.

204. Ivanova, R., Lindman, B., and Alexandridis, P., Effect of Glycols on the Self-Assembly of Amphiphilic Block Copolymers in Water. 1. Phase Diagrams and Structure Identification. *Langmuir*, 2000. **16**(8): p. 3660-3675.